Large Eddy Simulation of the Turbulence and Fiber Motion in a Headbox

By

Xiaosi Feng

B. Sc., Zhengzhou University, China, 1986

M. Sc., The Institute of Applied Physics and Computational Mathematics, China, 1989

A THESIS SUBMITTED IN PARTIAL FULFILLMENT OF
THE REQUIREMENTS OF THE DEGREE OF

DOCTOR OF PHILOSOPHY
in
THE FACULTY OF GRADUATE STUDIES

(Mechanical Engineering)

THE UNIVERSITY OF BRITISH COLUMBIA

August 2005

© Xiaosi Feng, 2005

Abstract

This thesis describes numerical simulations of the mean flow and the large-scale turbulence structures in a typical paper machine headbox. Parallel computational methods and a large eddy simulation (LES) model are used. Turbulent flow through the converging section is modelled and is then used, with a suitable fiber model, to make predictions of the statistical fiber orientation in the headbox.

The present large eddy simulations have been made with a new parallel computational code developed by the author for this purpose. Techniques for parallel computation of LES are discussed. In this code, the incompressible Navier-Stokes equations are solved using a staggered finite volume method for a generalized curvilinear coordinate system. The fractional step method is used to solve the momentum equations. A Poisson equation for pressure is obtained to satisfy the continuity equation. The Smagorinsky constant, the dynamic subgrid scale models and the approximate deconvolution model (ADM) are used in the large eddy simulations to account for the effects of the unresolved turbulent motions. Satisfactory validation of the new code is obtained through comparisons with experiments and computations of fully developed channel flow. The parallel efficiency is higher than 80% for the present parallel computation of LES.

For the converging section flow representing the headbox, the computed values of the mean velocity agree well with the measured values. For the rms fluctuations, there are some differences between the numerical and the measured results over the first third of the converging section. These differences appear to be related to the impossiblity to set accurately the flow in the experiment and to the inflow data used in the simulations. A modified method for the simulation of inflow conditions is proposed, and used, and better agreement with experimental data is obtained with the new inflow conditions.

The LES computer code is coupled with a suitable fiber model to predict the statistical orientation of nylon "fibers" in the converging section. The numerical methods give statistical results which are similar to existing experimental data for the fiber orientation.

Finally, high Reynolds number large eddy simulations are carried out for a commercial sized headbox of generic geometry. Two inflow conditions for the converging section are investigated and some conclusions are drawn.

Table of contents

Abstract ii

Table of contents iv

List of Tables vi

List of Figures vii

Nomenclature xi

Acknowledgements xiii

Chapter 1 Introduction 1

Chapter 2 Literature Review 4

2.1 Headbox 4
2.1.1 Headbox flow simulations 5
2.1.2 Fiber orientation 6

2.2 Numerical methods 7
2.2.1 Direct Numerical Simulation (DNS) 8
2.2.2 RANS models 9
2.2.3 Large Eddy Simulation 10

Chapter 3 Large Eddy Simulation for Fully Developed Channel Flow 12

3.1 Introduction 12

3.2 Governing equations 13
3.2.1 Filtered Navier-Stokes equations 13
3.2.2 Subgrid model 14
3.2.2.1 Dynamic subgrid model 16
3.2.2.2 Approximate deconvolution model (ADM) 18

3.3 Numerical methods 21
3.3.1 The flow solver 21
3.3.2 Numerical methods for solution of the Poisson equation 26
3.3.2.1 Direct method 26
3.3.2.2 Conjugate Gradient method and CGSTAB 26
3.3.3 Parallel computation for solution of the Poisson Equation 27
3.3.3.1 Parallel computation using the direct method 28
3.3.3.2 Parallel computation for CGSTAB method 28
3.3.4 Discrete test filters 30

3.4 Numerical results 31
3.4.1 Reynolds number $Re_\tau = 395$ 32
3.4.2 Results for Reynolds number $Re_\tau = 1655$ 42

3.5 Summary 47

Chapter 4 LES for Turbulent Flow through a Converging Section 49

4.1 Introduction 49

4.2 Flow simulation 50
4.2.1 Experimental setup 50
4.2.2 Numerical simulation of the converging section 52
4.2.3 Alternative methods for the generation of inflow data 62

4.3 Discussion 69
4.3.1 Dependence on grid resolution 70
4.3.2 Effects of the different subgrid models 74

4.4 Summary 77

Chapter 5 Fiber Concentration and Orientation 80

5.1 Introduction 80

5.2 Fiber concentration 81
5.2.1 Fiber model and wall model 81
5.2.2 Numerical results 83

5.3 Fiber orientation in the headbox 85
5.3.1 Initial conditions 85
5.3.2 Numerical results 86
5.3.3 Discussion 98

5.4 Summary 99

Chapter 6 Simulation of a Typical Industrial Headbox 101

6.1 Introduction 101

6.2 Flow simulation 101
6.2.1 Computational geometry 101
6.2.2 Inflow conditions 102
6.2.3 Numerical results 108

6.3 Summary 122

Chapter 7 Summary and Conclusions 124

7.1 Parallel computing 124

7.2 LES for turbulent flow through a converging section 125

7.3 Fiber orientation 127

7.4 Simulation of a typical industrial headbox 127

Chapter 8 Recommendations for Future Work 130

Bibliography 131

Appendix A 139

Appendix B 141

Appendix C 142

List of Tables

TABLE 3.1 EXECUTION TIME IN SECONDS, SPEED UP AND EFFICIENCY FOR DIFFERENT NUMBERS OF PROCESSORS ON $64\times64\times64$ GRID 30

TABLE 3.2 GRID PARAMETERS FOR $\mathrm{Re}_\tau = 395$ 33

TABLE 3.3 GRID PARAMETERS FOR $\mathrm{Re}_\tau = 1655$ 43

TABLE 4.1 THE GEOMETRY OF THE CONVERGING SECTION. 52

TABLE 4.2 GRID PARAMETERS. Nx, Ny, Nz DENOTE THE NUMBER OF MESHES IN THE STREAMWISE, SPANWISE AND WALL-NORMAL DIRECTIONS, RESPECTIVELY. δ IS HALF OF THE INLET HEIGHT OF THE CONVERGING SECTION. 71

TABLE 5.1 THE FIRST MOMENT ($\sum_i \alpha_i p(\alpha_i)\Delta\alpha_i$), SECOND MOMENT ($\sum_i \alpha_i^2 p(\alpha_i)\Delta\alpha_i$) AND THIRD MOMENT ($\sum_i \alpha_i^3 p(\alpha_i)\Delta\alpha_i$) OF THE PROBABILITY DISTRIBUTION IN X-Z PLANE 94

TABLE 5.2 THE FIRST MOMENT ($\sum_i \alpha_i p(\alpha_i)\Delta\alpha_i$), SECOND MOMENT ($\sum_i \alpha_i^2 p(\alpha_i)\Delta\alpha_i$) AND THIRD MOMENT ($\sum_i \alpha_i^3 p(\alpha_i)\Delta\alpha_i$) OF THE PROBABILITY DISTRIBUTION IN X-Y PLANE. 95

List of Figures

FIGURE 1.1 THE SCHEMA FOR THE PROCESS OF A PAPER MACHINE (FROM SHARIATI 2002). 1
FIGURE 3.1 SCHEMATIC OF ENERGY SPECTRUM ILLUSTRATING THE RELATIONSHIP AMONG RESOLVED, RESOLVED SUBFILTER-SCALE, AND SUBGRID-SCALE MOTIONS. ω IS THE WAVENUMBER. ω_c IS THE GRID CUTOFF WAVENUMBER (GULLBRAND AND CHOW 2003). 19
FIGURE 3.2 ILLUSTRATION OF THE PRIMARY CELL 22
FIGURE 3.3 CONTROL VOLUME FOR THE ξ_1 -MOMENTUM EQUATION. 24
FIGURE 3.4 TRAPEZOIDAL FILTER IN 3D. 31
FIGURE 3.5 SCHEMA OF THE CHANNEL FLOW 32
FIGURE 3.6 DIMENSIONLESS MEAN STREAMWISE VELOCITY PROFILES WITH THE ADM MODEL AND THE SMAGORINSKY MODEL 37
FIGURE 3.7 DIMENSIONLESS RMS FLUCTUATION OF U: $\sqrt{u'u'}/u_\tau$ WITH THE ADM MODEL AND THE SMAGORINSKY MODEL. 37
FIGURE 3.8 DIMENSIONLESS RMS FLUCTUATION OF V: $\sqrt{v'v'}/u_\tau$ WITH THE ADM MODEL AND THE SMAGORINSKY MODEL. 38
FIGURE 3.9 DIMENSIONLESS RMS FLUCTUATION OF W: $\sqrt{w'w'}/u_\tau$ WITH THE ADM MODEL AND THE SMAGORINSKY MODEL. 38
FIGURE 3.10 DIMENSIONLESS REYNOLDS STRESS: $u'v'/u_\tau^2$ WITH THE ADM MODEL AND THE SMAGORINSKY MODEL. 39
FIGURE 3.11 DIMENSIONLESS MEAN STREAMWISE VELOCITY PROFILES FROM THE CASE 2 39
FIGURE 3.12 DIMENSIONLESS RMS FLUCTUATION OF U: $\sqrt{u'u'}/u_\tau$ FROM THE CASE 2. 40
FIGURE 3.13 DIMENSIONLESS RMS FLUCTUATION OF V: $\sqrt{v'v'}/u_\tau$ FROM THE CASE 2. 40
FIGURE 3.14 DIMENSIONLESS RMS FLUCTUATION OF W: $\sqrt{w'w'}/u_\tau$ FROM THE CASE 2. 41
FIGURE 3.15 SGS MODEL COEFFICIENTS WITH THE MEDIUM MESH CASE (CASE 2). 41
FIGURE 3.16 RATIO OF SGS EDDY VISCOSITY TO MOLECULAR VISCOSITY: ν_T/ν WITH THE SMAGORINSKY MODEL AND THE ADM MODEL (IN CASE 2) 42
FIGURE 3.17 DIMENSIONLESS MEAN STREAMWISE VELOCITY PROFILES AT $\mathrm{Re}_\tau = 1655$. 44
FIGURE 3.18 DIMENSIONLESS RMS FLUCTUATION OF U: $\sqrt{u'u'}/u_\tau$ AT $\mathrm{Re}_\tau = 1655$. 45
FIGURE 3.19 DIMENSIONLESS RMS FLUCTUATION OF V: $\sqrt{v'v'}/u_\tau$ AT $\mathrm{Re}_\tau = 1655$. 45
FIGURE 3.20 DIMENSIONLESS REYNOLDS STRESS: $u'v'/u_\tau^2$ AT $\mathrm{Re}_\tau = 1655$. 46
FIGURE 3.21 DIMENSIONLESS RMS FLUCTUATION OF U: $\sqrt{u'u'}/u_\tau$ WITH $96\times128\times96$ MESH. 46
FIGURE 3.22 DIMENSIONLESS RMS FLUCTUATION OF V: $\sqrt{v'v'}/u_\tau$ WITH $96\times128\times96$ MESH. 47
FIGURE 4.1 FLOW LOOP IN THE EXPERIMENT (FROM SHARIATI 2002) 51
FIGURE 4.2 EXPERIMENTAL HEADBOX DRAWING (FROM SHARIATI 2002). 51
FIGURE 4.3 COMPUTATIONAL DOMAIN FOR THE CONVERGING SECTION. ONLY A SUBSET OF THE ACTUAL GRID IS PLOTTED. 55
FIGURE 4.4 MEASUREMENT LOCATIONS ALONG THE CENTERLINE OF THE CONVERGING SECTION (LINE ABC) AND THE VERTICAL LINE AT 0.03M AFTER INLET (LINE DE) 56
FIGURE 4.5 COMPARISON OF THE MEAN VELOCITY AT THE CENTERLINE OF THE CONVERGING SECTION. 56
FIGURE 4.6 COMPARISON OF RMS VALUE OF THE VELOCITY FLUCTUATION u' NORMALIZED BY u'_{in} 57

FIGURE 4.7 COMPARISON OF RMS VALUE OF THE VELOCITY FLUCTUATION v' NORMALIZED BY u'_{in} 57
FIGURE 4.8 COMPARISON OF RMS VALUE OF THE VELOCITY FLUCTUATION w' NORMALIZED BY u'_{in} 58
FIGURE 4.9 COMPARISON OF TURBULENCE KINETIC ENERGY k NONDIMENSIONALIZED BY k AT THE INLET OF THE POSITION 0.006M AFTER THE CONVERGENCE STARTS. 58
FIGURE 4.10 COMPARISON OF THE FLUCTUATING VELOCITY u' AT INLET FOR ONE CHANNEL INFLOW CONDITION WITH THE MEASURED VALUE AT THE VERTICAL LINE (DE LINE IN FIGURE 4.4) AT THE LOCATION 0.03M FROM THE INLET. 59
FIGURE 4.11 THE DIAGRAM OF " TWO-CHANNEL " INFLOW CONDITION. 59
FIGURE 4.12 COMPARISON OF THE MEAN VELOCITY AT THE CENTERLINE OF THE CONVERGING SECTION WITH DIFFERENT INFLOW CONDITIONS. 60
FIGURE 4.13 COMPARISON OF RMS VALUE OF THE VELOCITY FLUCTUATION u' NORMALIZED BY u'_{in} WITH DIFFERENT INFLOW CONDITIONS. 60
FIGURE 4.14 COMPARISON OF RMS VALUE OF THE VELOCITY FLUCTUATION v' NORMALIZED BY u'_{in} WITH DIFFERENT INFLOW CONDITIONS. 61
FIGURE 4.15 COMPARISON OF RMS VALUE OF THE VELOCITY FLUCTUATION w' NORMALIZED BY u'_{in} WITH DIFFERENT INFLOW CONDITIONS. 61
FIGURE 4.16 SCHEMATIC OF NEW INFLOW GENERATION TECHNIQUE. 64
FIGURE 4.17 COMPARISON OF RMS VALUE OF THE VELOCITY FLUCTUATION u' AT INLET WITH THE MEASURED VALUE AT THE VERTICAL LINE (LINE DE IN FIGURE 4.4) OF THE LOCATION 0.03M FROM THE INLET. 65
FIGURE 4.18 COMPARISON OF STREAMWISE COMPONENT OF THE MEAN VELOCITY AT THE INLET WITH THE MEASURED VALUE AT THE VERTICAL DE LINE (IN FIGURE 4.4) LOCATED 0.03M FROM THE INLET. 65
FIGURE 4.19 MEAN STREAMWISE VELOCITIES CALCULATED WITH THE NEW INFLOW CONDITION AT THE VERTICAL LINE (DE LINE IN FIGURE 4.4) COMPARED WITH MEASURED VALUES AT THE SAME LOCATION. ..66
FIGURE 4.20 COMPARISON OF RMS VALUE OF THE VELOCITY FLUCTUATION u' AT THE VERTICAL LINE (DE LINE IN FIGURE 4.4) WITH NEW INFLOW CONDITION. 66
FIGURE 4.21 MEAN VELOCITY AT THE CENTERLINE OF THE CONVERGING SECTION CALCULATED WITH NEW INFLOW CONDITION COMPARED TO MEASURED VALUES AT THE SAME LOCATION. 67
FIGURE 4.22 COMPARISON OF RMS VALUE OF THE VELOCITY FLUCTUATION u' NORMALIZED BY u'_{in} CALCULATED WITH THE NEW INFLOW CONDITION. 67
FIGURE 4.23 COMPARISON OF RMS VALUE OF THE VELOCITY FLUCTUATION v' NORMALIZED BY u'_{in} CALCULATED WITH THE NEW INFLOW CONDITION. 68
FIGURE 4.24 COMPARISON OF RMS VALUE OF THE VELOCITY FLUCTUATION w' NORMALIZED BY u'_{in} CALCULATED WITH THE NEW INFLOW CONDITION. 68
FIGURE 4.25 COMPARISON OF TURBULENCE KINETIC ENERGY K NONDIMENSIONALIZED BY k AT THE INLET OF THE POSITION 0.006M AFTER THE CONVERGENCE STARTS WITH THE NEW INFLOW CONDITION. 69
FIGURE 4.26 COMPARISON OF THE MEAN VELOCITY AT THE CENTERLINE OF THE CONVERGING SECTION WITH CASE 1 AND CASE 2. 71
FIGURE 4.27 COMPARISON OF RMS VALUE OF THE VELOCITY FLUCTUATION u' NORMALIZED BY u'_{in} WITH CASE 1 AND CASE 2. 72
FIGURE 4.28 COMPARISON OF RMS VALUE OF THE VELOCITY FLUCTUATION w' NORMALIZED BY u'_{in} WITH CASE 1 AND CASE 2 72
FIGURE 4.29 COMPARISON OF THE MEAN VELOCITY AT THE CENTERLINE OF THE CONVERGING SECTION WITH CASE1 AND CASE 3. 73
FIGURE 4.30 COMPARISON OF RMS VALUE OF THE VELOCITY FLUCTUATION u' NORMALIZED BY u'_{in} WITH CASE1 AND CASE 3. 73
FIGURE 4.31 COMPARISON OF RMS VALUE OF THE VELOCITY FLUCTUATION w' NORMALIZED BY u'_{in} WITH CASE1, AND CASE 3. 74

FIGURE 4.32 COMPARISON OF THE MEAN VELOCITY AT THE CENTERLINE OF THE CONVERGING SECTION WITH DIFFERENT SUBGRID MODELS 75
FIGURE 4.33 COMPARISON OF RMS VALUE OF THE VELOCITY FLUCTUATION u' NORMALIZED BY u'_{in} WITH DIFFERENT SUBGRID MODELS 75
FIGURE 4.34 COMPARISON OF RMS VALUE OF THE VELOCITY FLUCTUATION v' NORMALIZED BY u'_{in} WITH DIFFERENT SUBGRID MODELS 76
FIGURE 4.35 COMPARISON OF RMS VALUE OF THE VELOCITY FLUCTUATION w' NORMALIZED BY u'_{in} WITH DIFFERENT SUBGRID MODELS 76
FIGURE 4.36 RATIO OF SGS EDDY VISCOSITY TO MOLECULAR VISCOSITY: ν_T / ν WITH THE SMAGORINSKY MODEL. 77
FIGURE 5.1 A FIBER CONSISTING OF SPHEROIDS CONNECTED THROUGH BALL AND SOCKET JOINTS (FROM ROSS AND KLINGENBERG (1997)) 83
FIGURE 5.2 SCHEMA OF THE CHANNEL FLOW 83
FIGUER 5.3 CONCENTRATION FOR 0.001M, 0.002M, 0.003M FIBER VS. CHANNEL HEIGHT SCALED BY FIBER LENGTH WITH LES 84
FIGURE 5.4 A FIBER'S INITIAL POSITION. 85
FIGURE 5.5 MEASUREMENT POINTS ALONG THE HEADBOX, UNIT M. 90
FIGURE 5.6 INITIAL FIBER ORIENTATION DISTRIBUTION, (A) IN X-Z PLANE, (B) IN X-Y PLANE 90
FIGURE 5.7 FIBER ORIENTATION DISTRIBUTION AT X = 0.045M, (A) IN X-Z PLANE, (B) IN X-Y PLANE 91
FIGURE 5.8 FIBER ORIENTATION DISTRIBUTION AT X = 0.122M, (A) IN X-Z PLANE, (B) IN X-Y PLANE 91
FIGURE 5.9 FIBER ORIENTATION DISTRIBUTION AT X = 0.157M, (A) IN X-Z PLANE, (B) IN X-Y PLANE 92
FIGURE 5.10 FIBER ORIENTATION DISTRIBUTION AT X = 0.192M, (A) IN X-Z PLANE, (B) IN X-Y PLANE 92
FIGURE 5.11 FIBER ORIENTATION DISTRIBUTION AT X = 0.227M, (A) IN X-Z PLANE, (B) IN X-Y PLANE 93
FIGURE 5.12 FIBER ORIENTATION DISTRIBUTION AT X = 0.262M, (A) IN X-Z PLANE, (B) IN X-Y PLANE 93
FIGURE 5.13 FIBER ORIENTATION DISTRIBUTION AT THE CONVERGING SECTION EXIT, ... 94
FIGURE 5.14 THE FIRST MOMENT ($\sum_i \alpha_i p(\alpha_i)\Delta\alpha_i$) AT DIFFERENT STATIONS IN X-Z PLANE. 95
FIGURE 5.15 THE FIRST MOMENT ($\sum_i \alpha_i p(\alpha_i)\Delta\alpha_i$) AT DIFFERENT STATIONS IN X-Y PLANE. 96
FIGURE 5.16 THE SECOND MOMENT ($\sum_i \alpha_i^2 p(\alpha_i)\Delta\alpha_i$) AT DIFFERENT STATIONS IN X-Z PLANE 96
FIGURE 5.17 THE SECOND MOMENT ($\sum_i \alpha_i^2 p(\alpha_i)\Delta\alpha_i$) AT DIFFERENT STATIONS IN X-Y PLANE. 97
FIGURE 5.18 THE THIRD MOMENT ($\sum_i \alpha_i^3 p(\alpha_i)\Delta\alpha_i$) AT DIFFERENT STATIONS IN X-Z PLANE 97
FIGURE 5.19 THE THIRD MOMENT ($\sum_i \alpha_i^3 p(\alpha_i)\Delta\alpha_i$) AT DIFFERENT STATIONS IN X-Y PLANE. 98
FIGURE 5.20 FIBER ORIENTATION DISTRIBUTION AT X = 0.157M IN X-Y PLANE WITH 8000, 16,000 AND 24,000 FIBERS 99
FIGURE 6.1 THE GEOMETRY OF THE CONVERGING SECTION. 102
FIGURE 6.2 ONE-CHANNEL INFLOW CONDITION FOR THE CONVERGING SECTION 104
FIGURE 6.3 SCHEMATIC DIAGRAM OF THE "FIVE-CHANNEL" INFLOW CONDITION SHOWING THE DETAILS OF ONE OF THE FIVE IDENTICAL CHANNELS 105
FIGURE 6.4 COMPARISON OF THE MEAN VELOCITY AT THE INLET. 106
FIGURE 6.5 COMPARISON OF RMS VALUE OF THE VELOCITY FLUCTUATION u' AT THE INLET. 106
FIGURE 6.6 COMPARISON OF RMS VALUE OF THE VELOCITY FLUCTUATION v' AT THE INLET. 107
FIGURE 6.7 COMPARISON OF RMS VALUE OF THE VELOCITY FLUCTUATION w' AT THE INLET. 107
FIGURE 6.8 COMPARISON POSITIONS ALONG THE HEADBOX. 110
FIGURE 6.9 COMPARISON OF THE MEAN VELOCITY AT THE FIRST STATION AB 111

FIGURE 6.10 COMPARISON OF RMS VALUE OF THE VELOCITY FLUCTUATION u' AT THE FIRST STATION AB...111
FIGURE 6.11 COMPARISON OF RMS VALUE OF THE VELOCITY FLUCTUATION v' AT THE FIRST STATION AB. ...111
FIGURE 6.12 COMPARISON OF RMS VALUE OF THE VELOCITY FLUCTUATION w' AT THE FIRST STATION AB. ..112
FIGURE 6.13 COMPARISON OF THE MEAN VELOCITY PROFILES AT THE SECOND STATION CD. 112
FIGURE 6.14 COMPARISON OF RMS VALUE OF THE VELOCITY FLUCTUATION u' AT THE SECOND STATION CD. 113
FIGURE 6.15 COMPARISON OF RMS VALUE OF THE VELOCITY FLUCTUATION v' AT THE SECOND STATION CD. 113
FIGURE 6.16 COMPARISON OF RMS VALUE OF THE VELOCITY FLUCTUATION w' AT THE SECOND STATION CD. 114
FIGURE 6.17 COMPARISON OF THE MEAN VELOCITY AT THE THIRD STATION EF. 114
FIGURE 6.18 COMPARISON OF RMS VALUE OF THE VELOCITY FLUCTUATION u' AT THE THIRD STATION EF....115
FIGURE 6.19 COMPARISON OF RMS VALUE OF THE VELOCITY FLUCTUATION v' AT THE THIRD STATION EF....115
FIGURE 6.20 COMPARISON OF RMS VALUE OF THE VELOCITY FLUCTUATION w' AT THE THIRD STATION EF. ..116
FIGURE 6.21 COMPARISON OF THE MEAN VELOCITY AT THE OUTLET..... 116
FIGURE 6.22 COMPARISON OF RMS VALUE OF THE VELOCITY FLUCTUATION u' AT THE OUTLET..... 117
FIGURE 6.23 COMPARISON OF RMS VALUE OF THE VELOCITY FLUCTUATION v' AT THE OUTLET. 117
FIGURE 6.24 COMPARISON OF RMS VALUE OF THE VELOCITY FLUCTUATION w' AT THE OUTLET. 118
FIGURE 6.25 COMPARISON THE MEAN VELOCITY PROFILES AT THE OUTLET WITH THE SMAGORINSKY MODEL.118
FIGURE 6.26 COMPARISON OF RMS VALUE OF THE VELOCITY FLUCTUATION u' AT THE OUTLET WITH THE SMAGORINSKY MODEL. 119
FIGURE 6.27 COMPARISON OF RMS VALUE OF THE VELOCITY FLUCTUATION v' AT THE OUTLET WITH THE SMAGORINSKY MODEL. 119
FIGURE 6.28 COMPARISON OF RMS VALUE OF THE VELOCITY FLUCTUATION w' AT THE OUTLET WITH THE SMAGORINSKY MODEL. 120
FIGURE 6.29 COMPARISON OF THE RATIO v'/u' AT DIFFERENT POSITIONS. 120
FIGURE 6.30 COMPARISON OF THE RATIO w'/u' AT DIFFERENT POSITIONS. 121
FIGURE 6.31 COMPARISON OF THE RATIO v'/u' AT THE OUTLET WITH THE TWO DIFFERENT INFLOW CONDITIONS. 121
FIGURE 6.32 COMPARISON OF THE RATIO w'/u' AT THE OUTLET WITH THE TWO DIFFERENT INFLOW CONDITIONS. 122

Nomenclature

C_S	Smagorinsky constant
G	grid filter function
$\tilde{G}$	test filter
k	kinetic energy of turbulence
n	unit normal
$\overline{p}$	filtered pressure
R_b	Reynolds number based on bulk velocity
R_τ	Reynolds number based on friction velocity
S_t	Stokes number
$\overline{S}_{ij} = \frac{1}{2}(\frac{\partial \overline{u}_i}{\partial x_j} + \frac{\partial \overline{u}_j}{\partial x_i})$	filtered rate of strain tensor
$\lvert \overline{S} \rvert = \sqrt{2\overline{S}_{ij}\overline{S}_{ij}}$	magnitude of the strain tensor
t	time
$\overline{u}_i$	filtered velocity
U,V,W	mean velocity in x, y, z direction, respectively
U_b	bulk velocity
V	velocity vector
x, y, z	distance parameter
y^+	non-dimensional distance

Greek Letters

δ_{ij}	Kronecker delta
ε	dissipation rate of turbulence
μ	dynamic viscosity
ρ	density
τ_{ij}	Reynolds-stress tensor
ν_T	eddy viscosity
Δ	grid filter width
$\tilde{\Delta}$	test filter width
η	Kolmogorov microscale

Superscripts

*	nondimensionalized value

Acknowledgements

I would like to express my deepest appreciation to my research supervisors, Dr. Martha Salcudean and Dr. Ian Gartshore for their invaluable guidance and kind support that made this work possible.

I would also like to thank my research committee member, Dr. W. Kendal Bushe for his technical guidance and helpful suggestions. I gratefully acknowledge Dr. Mark Martinez for participating in my research committee and for his help.

Special thanks are due to Dr. Ned Djilali and Dr. Brian Wetton for their inspiration and useful discussions. I would like to thank to my colleagues at the University of British Columbia (UBC) specially Mohammad R. Shariati and Xun Zhang for providing experimental data for comparison.

I would like to thank Dr. Matthew W. Choptuik and Dr. Doug Phillips for their generosity and technical supports in the use of the PIII/Linux and P4-Xeon clusters at UBC and the MACI Alpha cluster at the University of Calgary. I also wish to acknowledge the financial assistance from FRBC and the Natural Science and Engineering Research Council of Canada.

Finally, I am deeply indebted to my wife Suqin, my daughter Manning, my parents and my brothers and sisters for their love, infinite patience, unconditional support and help throughout all the years of work.

Chapter 1 Introduction

The headbox is the first component of a paper machine in the papermaking system (Figure 1.1). The fiber orientation and basis weight profiles of the paper depend on the fluid flow in the headbox, which makes a headbox critical to a successful papermaking system.

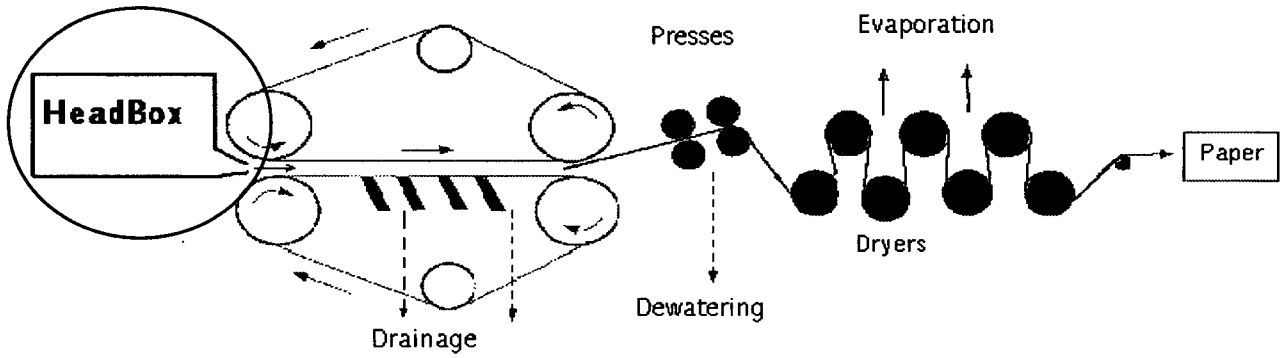

Figure 1.1 The schema for the process of a paper machine (from Shariati 2002).

The headbox can be several meters wide in the cross machine direction and has a contraction ratio (inlet area to outlet area) of 10 or more in a streamwise length of less than a meter. A dilute concentration of pulp fibers in water flows steadily through the headbox. The detailed introduction of the headbox will be given in chapter 2. One of its functions is to provide a discharge of stock (fibers and other substances in fluid suspension) at its outlet that is uniform in both the machine direction and across the width of the paper web (the cross direction). The stock is fed onto the forming section wire mesh through a slice (exit of the headbox) opening.

The forming section will drain water from the stock, leaving behind the fibers that naturally bond together into a sheet. A common way to speed up the papermaking process is to use a twin-wire

former that squeezes the water off simultaneously from above and below. Following the forming section, the paper web then passes through the presses, in which the rolls squeeze out excess water. After that, the web proceeds to the drying section, which consists of a set of steam-heated drums. Then the paper web goes through a calender. The calender is composed of a set of high-pressure rolls to give the web smoothness and increase its density. Finally the web is carried to the paper machine reel to be made into jumbo rolls.

To achieve good paper formation, there must be no fiber flocculation in the jet exiting the headbox. The fibers must also have an even distribution in the cross direction of the machine. Thus the flow in the headbox should have a minimal component of mean velocity in the cross-machine direction. At the same time, the maintenance of high intensity turbulence within the stock is required in headbox designs to prevent fiber flocculation. The turbulence characteristics are critically important, since the turbulence directly influences fiber flocculation and orientation.

Turbulence is a complex but common form of fluid motion. In many practical numerical simulations, the RANS (Reynolds averaged Navier-stokes) model is used to simulate the turbulent flow, together with a specific turbulence model such as the k-ε equation model. This provides results that agree well with the experimental data in simple flows. But for complex flows, such as the flow through the converging section of a headbox with its large and rapid contraction, the turbulence may become very anisotropic. In these cases, conventional turbulence models such as k-ε can not simulate the turbulence well. There are two ways to solve this problem. One way is to modify the k-ε equation model (using for example, a non-linear k-ε model such as that of Speziale (1987)) or using other models for the RANS equation. These modifications are not universal and require a test for each modified model. The other way is to use large eddy simulation methods. These are much more universal because they simulate more of the physical features of turbulence and use fewer model constants than RANS models.

The main objectives of the thesis are to investigate the turbulent flow and fiber orientation in the converging section of the headbox and to develop a computational tool necessary to carry out the investigation.

These objectives are listed below in the order they have been approached:

1. To develop a practical numerical tool based on LES which is capable of simulating the large scales of turbulence in a headbox.
2. To study parallel computing algorithms and develop an appropriate LES parallel code, that will allow simulations of the turbulent flow in the converging section of the headbox to be made.
3. To simulate the turbulent flow in the converging section.
4. To study the fiber orientation in a headbox coupling LES with the fiber model.
5. To simulate the turbulent flow in an industrial headbox.

Following this introductory chapter, a literature review is given in chapter 2. The headbox and the numerical methods to simulate the turbulence are also described in chapter 2. Chapter 3 describes the numerical results of LES for fully developed channel flow. In chapter 4, the results of LES for the turbulent flow through the converging section are presented. Chapter 5 describes the fiber motion through the converging section and the fiber concentration calculation for fully developed channel flow. The LES simulation for a typical industrial-scale headbox is described in chapter 6. The summary and conclusions are presented in chapter 7. Finally, recommendations for future work are given in chapter 8.

Chapter 2 Literature Review

2.1 Headbox

The function of the headbox is to supply a continuous flow of fibers and other substances in a fluid suspension at constant velocity both across the width of the paper machine and with respect to time. The formation and uniformity of the final paper product are dependent on the uniformity of flow through the headbox, so a good understanding of the headbox is necessary for a successful papermaking system (Smook 1992, Britt 1970 and Gavelin 1998).

The operational objectives of the headbox system are listed by Smook (1992) as follows:

- Spread stock evenly across the width of the machine.
- Level out cross-currents and consistency variations.
- Level out machine direction velocity gradients.
- Create controlled turbulence to eliminate fiber flocculation.
- Discharge fluid and fibers evenly from the slice opening so that they impinge on the forming fabric at the correct location and angle.

Headboxes can be classified as open, air-cushioned and hydraulic (Smook 1992).

In the open headbox, the stock surface is open to the atmosphere and the flow at the slice is varied through adjustments to the level of stock in the headbox. Open headboxes were used in early paper machines. As paper machine speeds increased, it became impractical to increase the height of stock, so the air-cushioned headbox was developed.

Air-cushioned headboxes use rotating hollow cylinders with large perforations in their walls to provide a high turbulence and to smooth velocity gradients. These boxes are pressurized by the hydraulic feed. A pressurized air chamber is incorporated at the top of the box (Peel 1999).

Hydraulic headboxes usually have no air chamber while the air-cushioned types do. They comprise most of the modern headboxes. Practically all headbox research today deals with hydraulic headboxes without air-cushions (Gavelin 1998). This thesis will therefore focus on hydraulic headboxes.

Headboxes can be divided into three sections according to the principal flow processes involved (Britt 1970): flow distribution, flow rectification and jet development. In the first section, the flow of stock is distributed across the width of the machine through a manifold distributor. In the second section, the flow from the distributor is rectified. In a hydraulic headbox, a tube bank is often used in the second section. The wall friction in the tubes dampens flow disturbances originating in the stock approach system, provides a resistance to flow which creates a more even flow distribution across the section and creates turbulence to prevent fiber flocculation in the paper-machine forming zone. The processes in the tube bank may include mixing and blending of separate flows from a distributor, eliminating undesirable cross-flows and eddies, improving the velocity profile and developing turbulence of desired scale and intensity (Dahl and Weiss 1975). The third section is responsible for developing the jet and delivering the stock to the sheet forming section. An ideal headbox should produce a uniform and stable jet over the width of the machine.

2.1.1 Headbox flow simulations

Shimizu and Wada (1992) have calculated the flow of water in a generic headbox using the k-ε model. They calculated the relationship between the varying height in the contracting part and the flow velocity distribution at the exit. The flow distribution was investigated in two dimensions and the jets from the diffuser tubes were modelled three-dimensionally. Hämäläinen (1993) used a

finite element method to model the manifold, the turbulence generating section, and the slice in two dimensions. Aidun and Kovacs (1995) have focussed on the study of secondary flows in the headbox and their effects on non-uniform fiber orientation and mass. A non-linear k-ε model developed by Speziale (1987) was employed. They reported surprisingly large secondary flows at the headbox exit. Bandahakavi and Aidun (1999) investigated the turbulent flow in the converging section of a headbox using the RNG k-ε model and the Reynolds Stress Model (RSM). The RNG k-ε model is an improved version of the standard k-ε model (Chowdhury 1993). They found that the results obtained from the RSM model are superior to those from the RNG k-ε model. Parsheh and Dahlkild (1999) compared the results of modeling the turbulence with different models. It was observed that the turbulence energy computed by the k-ε (linear) model is exaggerated. He *et al.* (1998), Hua *et al.* (1999, 2000) and Pougatch *et al.* (2005) have done a complete modeling of the manifold along with all the individual tubes with the k-ε model in three dimensions. Shariati *et al.* (2000, 2001) and Shariati (2002) studied the headbox flow both experimentally and numerically exploring various models for the turbulence (not including LES).

2.1.2 Fiber orientation

Fiber orientation refers to the angular distribution of fibers relative to the paper-machine direction (MD). Fiber orientation, both in the plane of the paper and in the paper thickness direction, significantly affects the paper quality (Loewen 1997).

Ullmar and Norman (1997) and Ullmar (1998) investigated experimentally the effect of the headbox contraction ratio on fiber orientation. They found that the effect of the contraction ratio is more significant on fiber orientation than that of the flow rate. The fibers have been found to be more strongly orientated in the machine direction for higher contraction ratios. Zhang (2001) measured the orientation of dyed nylon fibers moving in a pilot plexiglass headbox and conducted the numerical simulation of fiber orientation with a fiber motion model. The fiber orientation distribution was

calculated using the mean flow only. The fibers were seen to be more strongly oriented in the machine direction by the numerical predictions than was observed in the experiments. He concluded that the anisotropy of the fiber orientation in the headbox flow was caused not only by the mean flow field characteristics, but also by the turbulence characteristics, and the explicit effects of the turbulence should be included into the fiber model. Olson (2002) provided an analytic expression for the fiber orientation distribution in a headbox flow, neglecting the effect of turbulent dispersion. His analysis showed:

- Fiber orientation distribution is independent of the flow rate through the headbox.
- Fibers are more strongly oriented in the plane of the contraction than in the plane of the paper.
- The shape of the headbox does not affect the final fiber orientation distribution leaving the headbox.
- The contraction ratio is the only geometrical factor affecting fiber orientation distribution at the slice.

Olson *et al.* (2004) proposed an Eulerian model of a turbulent fiber suspension through a one-dimensional headbox to predict the fiber orientation distribution.

The contributions discussed earlier have helped considerably to understand better the flow and fiber motion in headboxes. However, a better representation of the turbulence in the headbox and its effect on fiber motion and distribution is necessary to advance the knowledge of paper making process and equipment design. The thesis objective is to address this issue.

2.2 Numerical methods

Generally, there are three numerical methods to simulate turbulence: direct numerical simulation, RANS models and large eddy simulation.

2.2.1 Direct Numerical Simulation (DNS)

A direct numerical simulation means a complete time dependent solution of the Navier-Stokes and continuity equations. The main idea of this method is to assume that the size of the smallest eddies in any turbulent flow is of the order of the Kolmogorov microscale ($\eta \sim (\nu^3 / \varepsilon)^{\frac{1}{4}}$, where ν is kinematic viscosity, and ε is the energy dissipation rate of the turbulent flow). A huge number of grids are required in space in order to resolve these eddies.

Unfortunately, DNS can only be applied to very small Reynolds number problems, because the necessary number of cells is roughly given by (Reynolds 1989)

$$N=O(Re^{\frac{9}{4}}),$$

where Re is defined by the bulk velocity and the characteristic length of the flow. For a typical headbox, this requirement suggests the need for a very large number of cells, more than 10^9, which is impossible using today's computational systems. In spite of this restriction, DNS has been applied to many relatively simple problems, such as homogenous isotropic turbulent flow and turbulent boundary layer and channel flow (Clark *et al.* 1978, Kim *et al.* 1987, Spalart 1989, Moser *et al.* 1999).

For channel flow, the grids required by DNS are

Re_H	N (grid number)
12,300	6.7×10^6
30,800	4.0×10^7
61,600	1.5×10^8
230,000	2.1×10^9

Here $\mathrm{Re}_H = \frac{U_m H}{\nu}$, U_m is the average velocity across the channel and 2H is the height of the channel. DNS techniques are very accurate (assuming the numerical error to be very small by using a spectral method or other high accuracy methods). The results can be used like experimental data to calibrate other models. But DNS is restricted to low Reynolds numbers.

2.2.2 RANS models

From a practical viewpoint, the RANS model provides a simple and powerful tool to obtain solutions to many flows.

For incompressible turbulent flow, the velocity u_i and kinematic pressure p can be decomposed into ensemble means and fluctuation parts as:

$$u_i = \overline{u}_i + u_i' \qquad p = \overline{p} + p',$$

where an overbar is an ensemble mean (a time average can be used in statistically steady turbulent flows, and spatial averages can be used in homogeneous turbulent flows).

The mean velocity and pressure are solutions of the Reynolds averaged Navier-Stokes and continuity equations which are given for constant density and viscosity by

$$\frac{\partial \overline{u}_i}{\partial t} + \overline{u}_j \frac{\partial \overline{u}_i}{\partial x_j} = -\frac{1}{\rho}\frac{\partial \overline{p}}{\partial x_i} + \nu \nabla^2 \overline{u}_i - \frac{1}{\rho}\frac{\partial \tau_{ij}}{\partial x_j} \tag{2.1}$$

$$\frac{\partial \overline{u}_i}{\partial x_i} = 0, \tag{2.2}$$

where $\tau_{ij} \equiv \rho \overline{u_i' u_j'}$ is the Reynolds stress tensor.

The Reynolds stress tensor needs a model or another equation (for higher order closure). The additional model is based on a combination of physical reasoning, dimensional analysis and empiricism. RANS models can be divided into two groups, eddy-viscosity models and shear-stress models, respectively. In eddy-viscosity models, the Reynolds stresses are modelled by:

$$-\overline{u_i'u_j'} = \nu_T\left(\frac{\partial \overline{u}_i}{\partial x_j} + \frac{\partial \overline{u}_j}{\partial x_i}\right) - \frac{2}{3}\delta_{ij}k \tag{2.3}$$

where ν_T is referred to as the effective turbulent viscosity, δ_{ij} is the Kronecker delta and $k \equiv \overline{u_i' u_i'}/2$. The shear-stress model, however, computes the Reynolds stress directly, without assuming the existence of an eddy viscosity. There are many models: zero-equation model (such as the mixing length model), one equation model (k, l, etc.), two-equation models ($k-\varepsilon$, $k-\omega$, etc.) and second-order closure models. A comprehensive overview of these models can be found in Wilcox (1998).

The RANS model is fairly efficient for many simple flows, so that results can often be obtained relatively quickly. But there are empirical choices of model constants for different flows. For complex flows, these constants are difficult to determine. The simpler $k-\varepsilon$ model essentially assumes isotropy of the turbulence by assuming a scalar effective viscosity that is independent of direction and k is calculated based on this assumption. The normal stresses like $\overline{u_1'^2}$ can be computed from the assumption of $\overline{u_1'^2} = \frac{2}{3}k - \nu_T\frac{\partial \overline{u}_1}{\partial x_1}$ in (2.3). With this assumption used in a converging section of a headbox (where $\frac{\partial \overline{u}_1}{\partial x_1}$ is very large near the exit), $\overline{u_1'^2}$ can become negative which of course is unphysical. This leads to the production term not being calculated accurately. The production term in the simpler $k-\varepsilon$ model is highly over estimated in comparison with the similar term in other turbulence models (Shariati 2002).

2.2.3 Large Eddy Simulation

From the above discussion, the major disadvantage of DNS is that it can only deal with low Reynolds number problems using currently available computers. The major defect of RANS models is that they are not truly universal for different turbulent flows and are even inapplicable to

some flows. LES, however, has advantages over both DNS and RANS. It employs a mesh resolution coarser than that used by DNS but fine enough to resolve the large-scale eddies and uses a turbulence model only for those eddies whose size is smaller than the mesh spacing. This model is called the SGS (Subgrid Scale) model. LES reduces computing time compared to DNS so that it can be applied to relatively high Reynolds number problems. The results of LES research can certainly be used to help improve engineering models of turbulence. Although LES is more economical than DNS (typically requires 5-10% of the CPU time need for DNS), the method still requires large computer resources.

Chapter 3 Large Eddy Simulation for Fully Developed Channel Flow

3.1 Introduction

Large eddy simulation is used to model the flow in a headbox because the contraction in the headbox produces unusual anisotropic turbulence that has an important effect on the fiber distribution leaving the headbox. The overall idea in the LES method is to filter out the smaller scales of turbulence, and to solve explicitly for the detailed unsteady motion in the remaining larger scale motions, using a simplified isotropic assumption for the effects of the smaller scales. Domain-decomposition is used to handle geometrically complicated domains such as those occurring in the headbox contraction. The finite volume method and a staggered grid are applied for discretization in space. A combination of a two-stage Adams-Bashforth scheme and the cyclic reduction method for the Poisson-like pressure equation is used to advance the solution in time.

Fully developed turbulent channel flow was tested as a code validation case. It is an ideal model flow for simulations of wall-bounded turbulence. Since the flow is fully developed, it is statistically homogeneous in the streamwise direction. Thus, periodic boundary conditions can be used in that direction, avoiding the problems associated with inflow and outflow boundary conditions. Fully developed channel flow has been studied numerically by other people using LES, for example, Deardorff (1970), Schumann (1975), Moin and Kim (1982), Horiuti (1987) and Piomelli, *et al.* (1988).

The filtered Navier-Stokes equations and subgrid models that are used are described in section 3.2. The numerical methods are presented in section 3.3. In section 3.4, the numerical results are provided. A summary is given in section 3.5.

3.2 Governing equations

3.2.1 Filtered Navier-Stokes equations

The incompressible Navier-Stokes equations for constant viscosity ν can be written in the following form

$$\frac{\partial u_i}{\partial x_i} = 0 \tag{3.1}$$

$$\frac{\partial u_i}{\partial t} + \frac{\partial u_i u_j}{\partial x_j} = -\frac{1}{\rho}\frac{\partial p}{\partial x_i} + \nu \frac{\partial^2 u_i}{\partial x_j \partial x_j} \tag{3.2}$$

where the indices $i, j = 1,2,3$ refer to x, y and z. Einstein's summation convention is applied, and u_i is the velocity in i-direction.

A filtering operation is performed on the Navier-Stokes equations to remove the small spatial scales. The resulting equations that describe the space-time evolution of the "large eddies" contain the subgrid scale stress tensor that describes the effect of the unresolved small scales on the resolved larger scales.

Any flow variable ϕ, in the fluid domain D, can be decomposed into a large-scale part (resolvable-scale filtered variables) $\bar{\phi}$ and a small-scale part (subgrid scale variables) ϕ' respectively, as

$$\phi = \bar{\phi} + \phi'$$

where

$$\overline{\phi} = \int_D G(x-x^*,\Delta)\phi(x^*)d^3x^*,$$

Δ is filter width, G is a filter function with property:

$$\int_D G(x-x^*,\Delta)d^3x^* = 1$$

A finite volume discretization involves a box-filter with

$$G(|x-\xi|,\Delta) = \begin{cases} \dfrac{1}{\Delta x_1 \Delta x_2 \Delta x_3} & |x_i-\xi_i| < \Delta x_i/2 \\ 0 & otherwise \end{cases} \qquad i = 1,2,3.$$

After applying the above box-filter to equations (3.1) and (3.2), we can get the filtered Navier-Stokes equations:

$$\frac{\partial \overline{u}_i}{\partial x_i} = 0 \tag{3.3}$$

$$\frac{\partial \overline{u}_i}{\partial t} + \frac{\partial \overline{u}_i \overline{u}_j}{\partial x_j} = -\frac{1}{\rho}\frac{\partial \overline{p}}{\partial x_i} + \nu \frac{\partial^2 \overline{u}_i}{\partial x_j \partial x_j} - \frac{\partial \tau_{ij}}{\partial x_j} \tag{3.4}$$

where the subgrid-scale (SGS) Reynolds stress tensor is written as

$$\tau_{ij} = \overline{u_i u_j} - \overline{u}_i \overline{u}_j \tag{3.5}$$

In order to solve the equations (3.3) and (3.4), the SGS Reynolds stress must be modelled with subgrid scale models.

3.2.2 Subgrid model

The most commonly used SGS model is the Smagorinsky model (1963). The model assumes the SGS stress follows a gradient-diffusion process, similar to molecular motion. Consequently, τ_{ij} is given by

$$\tau_{ij} - \frac{1}{3}\tau_{kk}\delta_{ij} = -2C_s\Delta^2 \mid \bar{S} \mid \bar{S}_{ij} = -2\nu_T \bar{S}_{ij} \tag{3.6}$$

where ν_T is the eddy viscosity related only to the smaller scale motions, $\bar{S}_{ij} = \frac{1}{2}(\frac{\partial \bar{u}_i}{\partial x_j} + \frac{\partial \bar{u}_j}{\partial x_i})$ is the filtered rate of strain tensor, $|\bar{S}| = \sqrt{2\bar{S}_{ij}\bar{S}_{ij}}$ is the magnitude of the strain tensor and C_S is the Smagorinsky constant ($0.1 \le C_s \le 0.24$, Rogallo and Moin (1984)). Here $\Delta = (\Delta x_1 * \Delta x_2 * \Delta x_3)^{\frac{1}{3}}$ is the filter width, $\Delta x_i (i = 1,2,3)$ is $i-$direction grid spacing. In the region close to the wall, the eddy viscosity has to be reduced, which is usually achieved by using a Driest damping function:

$$\nu_T = C_s[(1 - e^{-y^+/25})\Delta]^2 \mid \bar{S} \mid \tag{3.7}$$

Lilly (1966) postulated that

$$\nu_T = C_L \Delta q \tag{3.8}$$

where q^2 is the SGS kinetic energy and C_L is a closure coefficient. An equation for q^2 can be derived from a moment of the Navier-Stokes equation, which involves several terms that must be modelled. It is difficult to conclude that any significant improvement over the Smagorinsky model can be obtained with such a model.

The most complicated SGS model was created by Deardorff (1973) for application to the atmospheric boundary layer. The model consists of 10 partial differential equations and bears a strong resemblance to a second-order closure model. The computational effort was increased using this model, but almost no improvement in the results was obtained.

Several alternative models for the subgrid scale turbulence have been proposed: Yakhot *et al.* (1989) proposed a subgrid-scale model based on renormalization group (RNG) theory for the study of channel flow. Lesieur and Metais (1996) showed that Kraichnan's spectral eddy viscosity can be implemented in physical space, yielding the so-called structure-function model.

3.2.2.1 Dynamic subgrid model

A more flexible model for the subgrid turbulence has been devised by Germano *et al.* (1991), the dynamic SGS model. Their formulation begins with the Smagorinsky eddy-viscosity approximation. However, rather than assuming a fixed value of C_s a priori, they permit it to be computed as the LES proceeds. This is accomplished by using two filters (test filter $\tilde{G}$, and grid filter G). The characteristic length scale of $\tilde{G}$, which is $\tilde{\Delta}$, is larger than that of the grid filter G, Δ. The value of $\alpha = \tilde{\Delta}/\Delta$ depends on the filter type. From Najjar and Taffi (1996), Lund (1997), it is known that $\alpha = \sqrt{6}$ for a box-filter with a trapezoidal rule for a numerical test filter, $\alpha = 2$ for a box-filter with Simpson's rule for a numerical test filter. The grid filter and test filter are applied to the momentum equations (3.2) to produce the following equations:

$$\frac{\partial \tilde{\bar{u}}_i}{\partial t} + \frac{\partial \tilde{\bar{u}}_i \tilde{\bar{u}}_j}{\partial x_j} = -\frac{1}{\rho}\frac{\partial \tilde{\bar{p}}}{\partial x_i} + \nu \frac{\partial^2 \tilde{\bar{u}}_i}{\partial x_j \partial x_j} - \frac{\partial T_{ij}}{\partial x_j} \tag{3.9}$$

where the subtest stress is

$$T_{ij} = \widetilde{u_i u_j} - \tilde{\bar{u}}_i \tilde{\bar{u}}_j . \tag{3.10}$$

Now the test filter $\tilde{G}$ is applied to the filtered momentum equations (3.4)

$$\frac{\partial \tilde{\bar{u}}_i}{\partial t} + \frac{\partial \tilde{\bar{u}}_i \tilde{\bar{u}}_j}{\partial x_j} = -\frac{1}{\rho}\frac{\partial \tilde{\bar{p}}}{\partial x_i} + \nu \frac{\partial^2 \tilde{\bar{u}}_i}{\partial x_j \partial x_j} - \frac{\partial \tilde{\tau}_{ij}}{\partial x_j} - \frac{\partial \ell_{ij}}{\partial x_j} \tag{3.11}$$

$$\ell_{ij} = \widetilde{\bar{u}_i \bar{u}_j} - \tilde{\bar{u}}_i \tilde{\bar{u}}_j \tag{3.12}$$

Using equation (3.9) and (3.11), the resolved turbulent stress ℓ_{ij} can be expressed with

$$\ell_{ij} = T_{ij} - \tilde{\tau}_{ij} \tag{3.13}$$

The subgrid-scale and subtest-scale stress are then modelled by the Smagorinsky model:

$$\tau_{ij} - \frac{1}{3}\tau_{kk}\delta_{ij} = -2C\Delta^2 |\bar{S}| \bar{S}_{ij} = -2C\beta_{ij} \tag{3.14}$$

$$T_{ij} - \frac{1}{3} T_{kk} \delta_{ij} = -2C\tilde{\Delta}^2 \,|\, \tilde{\bar{S}} \,|\, \tilde{\bar{S}}_{ij} = -2C\alpha_{ij} \tag{3.15}$$

where $\beta_{ij} = \Delta^2 \,|\, \bar{S} \,|\, \bar{S}_{ij}$, $\alpha_{ij} = \tilde{\Delta}^2 \,|\, \tilde{\bar{S}} \,|\, \tilde{\bar{S}}_{ij}$.

Substitution of (3.14) and (3.15) into (3.13) gives

$$\ell_{ij} - \frac{1}{3} \ell_{kk} \delta_{ij} = -2C(\alpha_{ij} - \tilde{\beta}_{ij}) . \tag{3.16}$$

Equation (3.16) represents a set of five independent equations that unfortunately cannot be solved explicitly for C. Lilly (1992) suggested computing the optimum in the least squares sense. The error is

$$Q = (\ell_{ij} - \frac{1}{3} \ell_{kk} \delta_{ij} + 2CM_{ij})^2 \tag{3.17}$$

where

$$M_{ij} = \tilde{\Delta}^2 \,|\, \tilde{\bar{S}} \,|\, \tilde{\bar{S}}_{ij} - \Delta^2 \widetilde{|\, \bar{S} \,|\, \bar{S}_{ij}} \tag{3.18}$$

is minimized by $\partial Q / \partial C = 0$, which yields:

$$C(x, y, z, t) = -\frac{\ell_{ij} M_{ij}}{2 M_{ij} M_{ij}} \tag{3.19}$$

The numerator $\ell_{ij} M_{ij}$ can have both negative and positive values. This leads to eddy viscosities of both signs. A negative eddy viscosity is considered a way of representing backscatter, which takes place as energy is transferred from the small scales to large scales in turbulent flows. But negative viscosity may cause a numerical instability. One way to avoid this is to employ averaging. It is a common procedure to average the denominator and the numerator in homogeneous directions (Germano *et al.* 1991, Najjar and Taffi 1996) in turbulent channel flows. This results in:

$$C(y, t) = -\frac{\langle \ell_{ij} M_{ij} \rangle_{xz}}{\langle 2 M_{ij} M_{ij} \rangle_{xz}} \tag{3.20}$$

where the brackets ($\langle\rangle$) represent an average over the spatial region, $\langle\rangle_{xz}$ is a plane averaging operation in the x and z directions, which are usually homogeneous in a turbulent channel flow. For fully inhomogeneous flows, Ghosal *et al.* (1995) proposed a dynamic localization model based on a constrained variational formulation.

Both the dynamic subgrid model and the simpler Smagorinsky model for subgrid turbulence will be used to produce the numerical results described in the following sections.

3.2.2.2 Approximate deconvolution model (ADM)

For the finite volume method, a box-filter is considered 'implicit' filtering of the Navier-Stokes equations. This approach has the advantage that it does not need to define a filter function. There are no explicit filter operations. For the dynamic Smagorinsky model, the only test filter is constructed to model the subgrid scales.

In contrast, a filter is defined when explicit filtering is used. The flow is divided into resolved and subfilter-scale (SFS) motions. The SFS motions can be further divided into resolved SFS (RSFS) and unresolved SFS (USFS) (Zhou *et al.* 2001, Carati *et al.* 2001). The USFS is commonly called SGS. The RSFS motions can be reconstructed from the resolved motions. The SGS (USFS) can not be represented directly and must be modelled. The schematic of energy spectrum is shown in Figure 3.1.

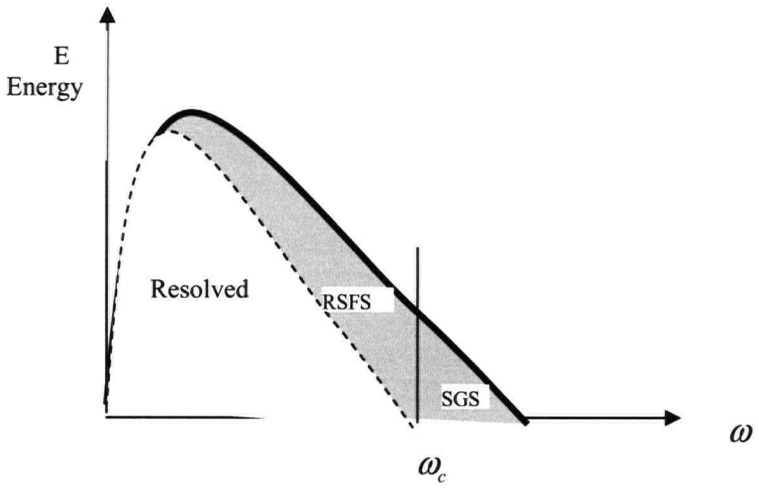

Figure 3.1 Schematic of energy spectrum illustrating the relationship among resolved, resolved subfilter-scale, and subgrid-scale motions. ω is the wavenumber. ω_c is the grid cutoff wavenumber (Gullbrand and Chow 2003).

Stolz *et al.* (2001) used u^* to approximate the unfiltered solution u. The approximate deconvolution u^* is computed by applying the deconvolution operator Q_N to the filter quantity $\overline{u}$

$$u^* = Q_N * \overline{u} \tag{3.21}$$

The operator Q_N is obtained by expanding the inverse of the filter G as an infinite series and truncating it at finite N. This leads to Q_N as an approximation of G^{-1},

$$Q_N = \sum_{i=0}^{N} (I - G)^i \approx G^{-1} \tag{3.22}$$

where I is the identity operator (Stolz *et al.* 1999). It is found that the deconvolution order $N = 5$ is sufficient for numerical test cases (Stolz *et al.* 2001). Using (3.22), u^* can be computed by repeated filtering of $\overline{u}$ from

$$u^* = Q_N \overline{u} = \overline{u} + (\overline{u} - \overline{\overline{u}}) + (\overline{u} - 2\overline{\overline{u}} + \overline{\overline{\overline{u}}}) + \ldots \tag{3.23}$$

The subgrid-scale Reynolds stress tensor τ_{ij} in (3.5) can be divided into two terms: SGS and RSFS

$$\tau_{ij} = (\overline{u_i u_j} - \overline{u_i^* u_j^*}) + (\overline{u_i^* u_j^*} - \overline{u}_i \overline{u}_j) \tag{3.24}$$

SGS(USFS) RSFS

To model the transfer of energy to small scales, represented by $\overline{u_i u_j} - \overline{u_i^* u_j^*}$, a relaxation term $\chi_u (I - Q_N * G) * \overline{u}$ is added for the ADM model. The RSFS term in (3.24) is moved to the left of the filtered Navier-Stokes equation (3.4). The equation (3.4) with the ADM model can be written into

$$\frac{\partial \overline{u}_i}{\partial t} + \frac{\overline{\partial u_i^* u_j^*}}{\partial x_j} = -\frac{1}{\rho}\frac{\partial \overline{p}}{\partial x_i} + \nu \frac{\partial^2 \overline{u}_i}{\partial x_j \partial x_j} - \chi_u (I - Q_N * G) * \overline{u}_i \quad . \tag{3.25}$$

where $\chi_u > 0$ is a relaxation coefficient.

The relaxation coefficient χ_u can be determined dynamically (Stolz *et al.* 2001). The second-order structure function (Lesieur and Metais 1996) is applied to $(I - Q_N * G) * \overline{u}$. The structure function F_2 is defined as

$$F_2(\xi, t) = \left\| \phi_u(\xi + r, t) - \phi_u(\xi, t) \right\|^2_{\|r\| = h} \tag{3.26}$$

where h is the grid size in computational space $\xi = (\xi_1, \xi_2, \xi_3)$, $\phi_u = \{\phi_1, \phi_2, \phi_3\}$ with $\phi_i = (I - Q_N * G) * \overline{u}_i$.

To estimate the relaxation coefficient χ_u, the equation (3.25) is solved two times in one time step, once using $\chi_u = \chi_{u_0}$ and once using $\chi_u = 0$. χ_{u_0} is the χ_u value from the previous time step or a positive constant at time t=0. The difference of the structure function $F_2(\xi, t^n + \Delta t)|_{\chi_u = 0} - F_2(\xi, t^n)$ represents an estimate of the energy generation of non-resolved scales within Δt. The difference $F_2(\xi, t^n + \Delta t)|_{\chi_u = 0} - F_2(\xi, t^n + \Delta t)|_{\chi_u = \chi_{u_0}}$ estimates how much energy would be dissipated by the relaxation term using $\chi_u = \chi_{u_0}$. Then χ_u can be computed from

$$\chi_u = \chi_{u_0} \frac{F_2(\xi, t^n + \Delta t)|_{\chi_u=0} - F_2(\xi, t^n)}{F_2(\xi, t^n + \Delta t)|_{\chi_u=0} - \xi, t^n + \Delta t)|_{\chi_u=\chi_{u_0}}}. \tag{3.27}$$

This ADM model will be used in the following chapters to compare with the Smagorinsky model. Another alternative is using the dynamic Smagorinsky model to compute the subgrid scales instead of using the relaxation term in the ADM model. This leads to the dynamic reconstruction model (DRM) which combines the ADM model with the dynamic Smagorinsky model (Gullbrand and Chow 2003).

3.3 Numerical methods

3.3.1 The flow solver

The equations governing incompressible and isothermal flow with constant density are written into a conservative form:

$$\int \mathbf{V} \cdot \mathbf{n} \, dS = 0 \tag{3.28}$$

$$\frac{\partial}{\partial t}\int_V u dV + \int_S [u\,\mathbf{V} \cdot \mathbf{n} + \frac{p}{\rho} n_x - \nu(n_x \frac{\partial u}{\partial x} + n_y \frac{\partial u}{\partial y} + n_z \frac{\partial u}{\partial z})] dS = 0 \tag{3.29}$$

$$\frac{\partial}{\partial t}\int_V v dV + \int_S [v\,\mathbf{V} \cdot \mathbf{n} + \frac{p}{\rho} n_y - \nu(n_x \frac{\partial v}{\partial x} + n_y \frac{\partial v}{\partial y} + n_z \frac{\partial v}{\partial z})] dS = 0 \tag{3.30}$$

$$\frac{\partial}{\partial t}\int_V w dV + \int_S [w\,\mathbf{V} \cdot \mathbf{n} + \frac{p}{\rho} n_z - \nu(n_x \frac{\partial w}{\partial x} + n_y \frac{\partial w}{\partial y} + n_z \frac{\partial w}{\partial z})] dS = 0 \tag{3.31}$$

where $\mathbf{V}$ is the velocity vector, dV is a volume element, dS is an area element and $\mathbf{n} = n_x\mathbf{i} + n_y\mathbf{j} + n_z\mathbf{k}$ is a unit normal of the control volume face.

The scheme used in this thesis is based on a fraction-step method (Chorin 1968, Kim and Moin 1987). The pressure gradient and the incompressibility constraint are integrated implicitly in time. The convective and diffusive terms are treated explicitly with the second-order Adams-

Bashforth scheme in time. For finite volume discretization, the flux is computed by a second-order accurate averaging which is therefore equivalent to second-order central difference scheme.

A general nonorthogonal coordinate system (ξ_1, ξ_2, ξ_3) is defined by

$$\mathbf{r} = \mathbf{r}(\xi_1, \xi_2, \xi_3),$$

where $\mathbf{r} = (x, y, z)^T$ is the Cartesian coordinate system (He and Salcudean 1994, Rosenfeld et al. 1991). The computational domain (ξ_1, ξ_2, ξ_3) is divided into uniform general cells (or scalar control cells) with mesh size $\Delta\xi_i = 1$, and the center of each general cell corresponds to the indices i, j, k.

The general cell is illustrated in Figure 3.2. The surface area vectors, $\mathbf{S}^i$ (i = 1,2,3), are defined at the centers of the control volume surfaces, and are locally parallel to the coordinate line ξ_i.

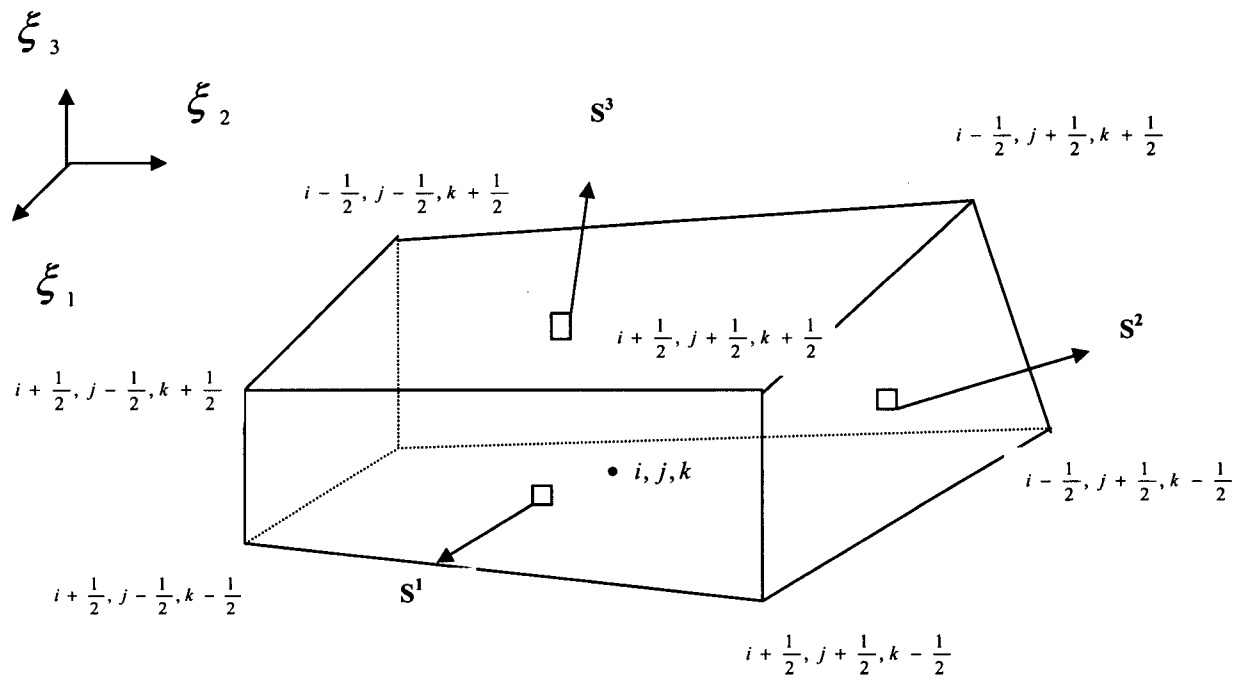

Figure 3.2 Illustration of the primary cell

Integrating the equation (3.28) over a primary cell, as shown in Figure 3.2, we get

$$(\mathbf{S}^1.\mathbf{V})_{i+1/2} - (\mathbf{S}^1.\mathbf{V})_{i-1/2} + (\mathbf{S}^2.\mathbf{V})_{j+1/2} - (\mathbf{S}^2.\mathbf{V})_{j-1/2}$$

$$+ (\mathbf{S}^3.\mathbf{V})_{k+1/2} - (\mathbf{S}^3.\mathbf{V})_{k-1/2} = \sum_{faces} \mathbf{S}^i \bullet \mathbf{V} = 0 \qquad (3.32)$$

where $\sum$ implies summation (with the proper signs) over all the faces of a primary cell. Each term of (3.32) represents the volume flux over the corresponding face. The volume fluxes are selected as the velocity unknowns. Let

$$U^1 = \mathbf{S}^1 \cdot \mathbf{V}$$

$$U^2 = \mathbf{S}^2 \cdot \mathbf{V}$$

$$U^3 = \mathbf{S}^3 \cdot \mathbf{V}$$

where U^1, U^2 and U^3 are the volume fluxes defined at the center of ξ_1, ξ_2 and ξ_3 faces in a primary cell. Then the equation of (3.32) can be written as

$$U^1_{i+1/2} - U^1_{i-1/2} + U^2_{j+1/2} - U^2_{j-1/2} + U^3_{k+1/2} - U^3_{k-1/2} = 0$$

or $$D_{iv}(U^l) = 0, \qquad (3.33)$$

where $U^l = (U^1, U^2, U^3)$. The summation operator D_{iv} is a discrete divergence-like operator (the divergence operator itself is $\frac{1}{V} D_{iv}$, where V is the cell volume).

Different computational cells are used for the discretization of the momentum equations. Each cell has the element size of $\Delta\xi_1 \times \Delta\xi_2 \times \Delta\xi_3$ in the computational space, but centers are located differently at $(i+\frac{1}{2}, j, k)$, $(i, j+\frac{1}{2}, k)$, and $(i, j, k+\frac{1}{2})$ for the U^1, U^2 and U^3 momentum equations. This grid uses the staggered-grid convention.

The control volume used for the discretization of U^1 equation is shown in Figure 3.3.

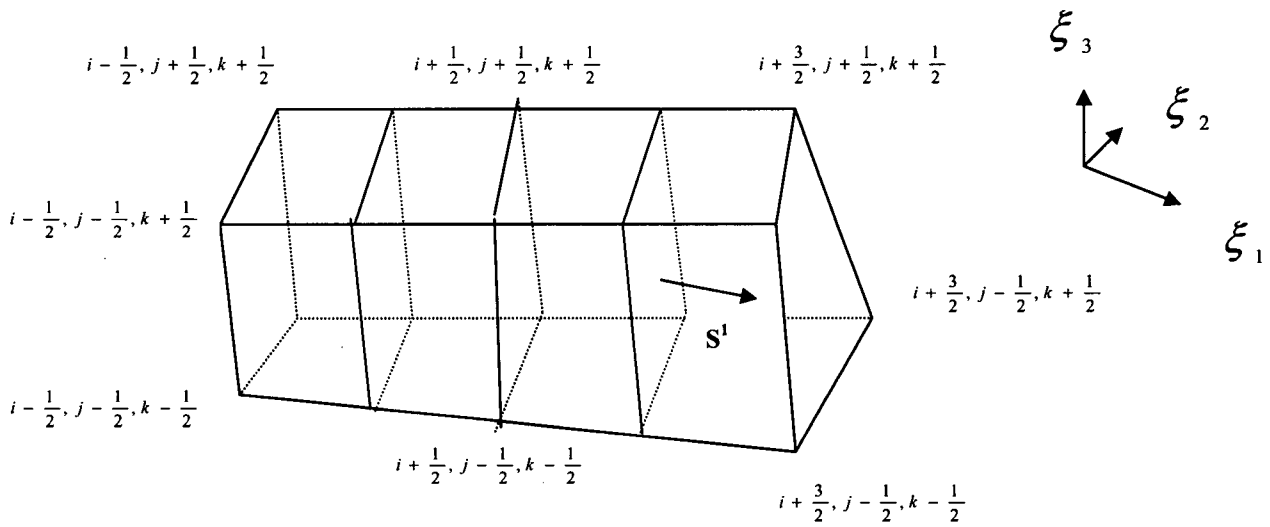

Figure 3.3 Control volume for the ξ_1 -momentum equation.

Dotting $\mathbf{S}^1_{i+1/2}$ with (3.29), (3.30) and (3.31) produces

$$V_{i+1/2}\frac{dU^1_{i+1/2}}{dt} = \mathbf{S}^1_{i+1/2}\ \mathbf{F}_{i+1/2} \tag{3.34}$$

where $\mathbf{F}_{i+1/2}$ is the total flux through the computational cell of the ξ_1 -momentum equation, and $V_{i+1/2}$ is the volume of the control cell. The equation (3.34) also can be written as

$$V_{i+1/2}\frac{dU^1_{i+1/2}}{dt} = L_1 \tag{3.35}$$

where L_1 is the right side of equation (3.34). L_1 can be split into two parts,

$$L_1 = H_1(U^l) + R_1(P), \tag{3.36}$$

where $H_1(U^l)$ is an operator representing the discretized convective, diffusive terms , and $R_1(P)$ is the operator of discretized pressure terms.

In the first step, the pressure terms are dropped from the equation (3.35). An Adams-Bashforth scheme is used to advance the time step.

$$U_{i+1/2}^{1\,*}=U_{i+1/2}^{1\,n}+\frac{\Delta t}{2V_{i+1/2}}(3H_1(U^{l\,n})-H_1(U^{l\,n-1})) \tag{3.37}$$

where $U_{i+1/2}^{1\,*}$ is an intermediate velocity which does not generally satisfy the continuity equation. Substitution of (3.37) into (3.35) yields

$$U_{i+1/2}^{1\;n+1}=U_{i+1/2}^{1\,*}+\frac{\Delta t}{V_{i+1/2}}R_1(p^{n+1}) \tag{3.38}$$

In a similar way, the ξ_2 - and ξ_3 -momentum equation, for which the control cell centers are located at $(i, j+\frac{1}{2}, k)$, and $(i, j, k+\frac{1}{2})$ respectively, can be discretized as

$$U_{j+1/2}^{2\,*}=U_{j+1/2}^{2\,n}+\frac{\Delta t}{2V_{j+1/2}}(3H_2(U^{l\,n})-H_2(U^{l\,n-1})) \tag{3.39}$$

$$U_{j+1/2}^{2\;n+1}=U_{j+1/2}^{2\,*}+\frac{\Delta t}{V_{j+1/2}}R_2(p^{n+1}) \tag{3.40}$$

$$U_{k+1/2}^{3\,*}=U_{k+1/2}^{3\,n}+\frac{\Delta t}{2V_{k+1/2}}(3H_3(U^{l\,n})-H_3(U^{l\,n-1})) \tag{3.41}$$

$$U_{k+1/2}^{3\;n+1}=U_{k+1/2}^{3\,*}+\frac{\Delta t}{V_{k+1/2}}R_3(p^{n+1}) \tag{3.42}$$

where $H_2(U^l)$ and $H_3(U^l)$ are the operators representing the discretized convective, diffusive terms , and $R_2(P)$ and $R_3(P)$ are the operators of the discretized pressure terms.

Substituting (3.38), (3.40) and (3.42) into (3.33) gives the following discrete Poisson equation

$$-D_{iv}(U^{l\,*})=\Delta t D_{iv}(\frac{R_l(p^{n+1})}{V_{m+1/2}}) \tag{3.43}$$

or

$$D_{iv}(\frac{R_l(p^{n+1})}{V_{m+1/2}}) = -\frac{1}{\Delta t} D_{iv}(U^{l*}) \tag{3.44}$$

where $m = i, j,$ or k for $l = 1,2$ or 3, respectively.

In the next step, the pressure field is obtained by solving the Poisson equation (3.44). Finally, the new velocities at the $(n+1)$ time step are computed from (3.38), (3.40) and (3.42).

3.3.2 Numerical methods for solution of the Poisson equation

3.3.2.1 Direct method

If there is one periodic direction, we can use fast a Fourier transform (FFT) in that direction, resulting in a two-dimensional Helmholtz equations. The cyclic reduction method (Golub and Van Loan (1993)) is used to solve the Helmholtz equations. Finally an inverse FFT is then applied to obtain the three-dimensional solution.

In our code, VFFTPACK and FISHPACK libraries from netlib were used to implement the fast Fourier transform and cyclic reduction methods.

This approach is very fast. The exact solution is found in a finite number of operations. The pressure Poisson equation in the channel flow computation is solved with this approach. Note however that this solution method is restricted to special cases: those having one direction of periodicity and orthogonal computational meshes.

3.3.2.2 Conjugate Gradient method and CGSTAB

The Poisson equation (3.44) can be written into a linear system, $AU = Q$, where the matrix A is sparse. The method of Conjugate gradients (CG) is often used for solving sparse positive definite systems. This method is iterative in that it generates a sequence of vectors $\{u_0, u_1, u_2, \ldots\}$ that end when $\| r_k \|_2 = \| Q - Au_k \|_2$ is small enough. The effectiveness of this method for sparse matrices lies in the fact that only the computation of Ap for some vector p is required. This can be

done quickly since A contains only a few non-zero entries in each row. Most often, CG is used in combination with some kind of preconditioning to reduce the total number of iterations (Golub and Van Loan (1993)). The CG algorithm is presented in Appendix A.

The CG method is applicable only to symmetric positive definite systems. To apply the CG method to systems of equations that are not symmetric, such as the pressure Poisson equation in non-orthogonal meshes, we need to use a different method. One of the most stable and robust conjugate gradient methods for solving non-symmetric systems, Bi-Conjugate Gradient Stabilized (BI-CGSTAB) is used. It is also known as CGSTAB (Van den Vorst 1992). The CGSTAB algorithm can also be found in Appendix A. The CGSTAB algorithm performs approximately twice as many operations as the preconditioned CG algorithm.

Although the fast multi-grid method (Hackbusch 1985) can also be used to solve the Poisson equation, it is difficult to use with non-orthogonal meshes.

3.3.3 Parallel computation for solution of the Poisson Equation

The rapid growth in the capability of single processor computers has slowed in recent years. It now appears that further increases in speed will require multiple processors, i.e. parallel computers. One of the characteristics of modern distributed memory parallel computers is very high computational potential. This is very attractive for the simulation of complicated turbulent flow problems since these problems, when posed in complex geometries can be very large and time consuming. Furthermore, these problems cannot be solved easily with high grid resolution due to limitations of memory on a single workstation. Parallel computation can reduce the computing time and memory requirements per processor.

Message-Passing Interface (MPI), the de facto message-passing standard, is a library specification for message passing. It is designed for high performance on both massively parallel machines and on workstation clusters. It is an efficient match to the hardware available at UBC.

3.3.3.1 Parallel computation using the direct method

For parallel calculation, the processors are decomposed into one direction. First, FFT is used in the periodic direction. Then ALL-TO-ALL (MPI command) is used to exchange the data. The rest is the same as the sequential calculation.

3.3.3.2 Parallel computation for CGSTAB method

For the CGSTAB method, the Incomplete LU (ILU) is used as a preconditioner (Gustafsson 1978, Ferziger and Peric 2001). These preconditioners, which have proven their effectiveness on serial machines, have an inherent sequentiality which makes them difficult to parallelize.

The ILU preconditioner has a known factorization of $M = LU$ where M, which is known as the preconditioning matrix, L is a lower triangular matrix with the same non-zero structure as the lower triangular part of A, and U is an upper triangular matrix U of similar form (see Appendix B). The solution of a linear system involving M requires a forward and backward substitution in solving lower and upper triangular systems respectively.

Parallelization of the construction of L, U and solution of the triangular systems is comparable. The parallel implementation of $Lx = b$ is only considered here. The dependencies can be seen immediately. In the first step, the equation is solved with no dependencies because the first row of L contains only one element. In the second step, the results can be computed once the first solution is known and used as a substitution. Each of those solutions can be substituted into two (in 2D) or three (in 3D) other dependent equations, and so on.

A staircase parallelization algorithm is used for the parallel implementation (Bastian and Horton 1991, Vuik et al., 1998). One advantage of this method is that the serial and parallel versions of this method have the same behavior with respect to convergence. The rectangular computational domain is decomposed into p strips parallel to the y-axis. For a 5-point stencil, unknowns (i, j) depend only on $(i-1, j)$ and $(i, j-1)$. The algorithm is shown as follows: in the first step,

processor 1 calculates unknown $(i,1)$ and sends the boundary value to processor 2. The processors 2 and 3 are idle. Then processor 2 calculates $(i,1)$ and sends the boundary value to processor 3. At the same time, processor 1 calculates $(i,2)$ in parallel and exchanges the boundary data to processor 2. Then processor 3 calculates $(i,1)$. After some start-up time, all processors are running.

For the 3D case, Joubert *et al.*, (2000) extend the staircase parallel strategy. The basic concept of this algorithm is based on imposing 2D processor decomposition on the 3D grid and changing the computation order so that the processors can be used with computations as quickly as possible while the processor idle time is minimized. This algorithm is used to parallel CGSTAB method in our code.

For parallel computation with LES, the domain decomposition approach is used to partition the data. Each sub-domain data is assigned to one processor to calculate the quantities and exchange the boundary data with neighbors. Two extra rows of cells are added for each block as ghost cells (sub-domain boundaries). In one time step, each processor solves the same equations with each sub-domain data and passes the boundary information to its neighbors. It then proceeds to the next time step.

Table 3.1 shows the execution time of the LES for the converging section in 100 time steps. The computational time reduces significantly with 8 processors. For measuring the performance of the two different systems, the following true speedup and efficiency definitions are used (Vuik *et al.*, 1998):

$$S(p) = \frac{\text{wall clock time for a run on one processor}}{\text{wall clock time for a run on } p \text{ processors}},$$

$$E(p) = S(p)/p.$$

From the Table 3.1, the efficiency is higher than 80%. Furthermore, the parallel approach for LES reduces the memory usage with processors. It is therefore possible to compute large sized problems.

Processors / Cases	1	4	8
LES for converging section (100 time steps)	791.79	232.11	122.56
Speed up $S(p)$	1	3.41	6.46
Efficiency $E(p)$	1	0.85	0.80

Table 3.1 Execution time in seconds, speed up and efficiency for different numbers of processors on 64×64×64 grid

3.3.4 Discrete test filters

The filtering operation in one dimension is defined as

$$\overline{f(x)} = \int_{x-\Delta x}^{x+\Delta x} G(x-x')f(x')dx'. \tag{3.45}$$

The box-filter then becomes

$$G(x-x') = \frac{1}{2\Delta x} \qquad if \ |x-x'| \le \Delta x \tag{3.46}$$

$$G(x-x') = 0 \qquad if \ |x-x'| > \Delta x. \tag{3.47}$$

The trapezoidal rule is applied to the numerical integration (Burden and Faires (1993)). The result is the following second-order accurate trapezoidal filter

$$\overline{f(x)} = \frac{1}{4}(f(x-\Delta x)+2f(x)+f(x+\Delta x)). \tag{3.48}$$

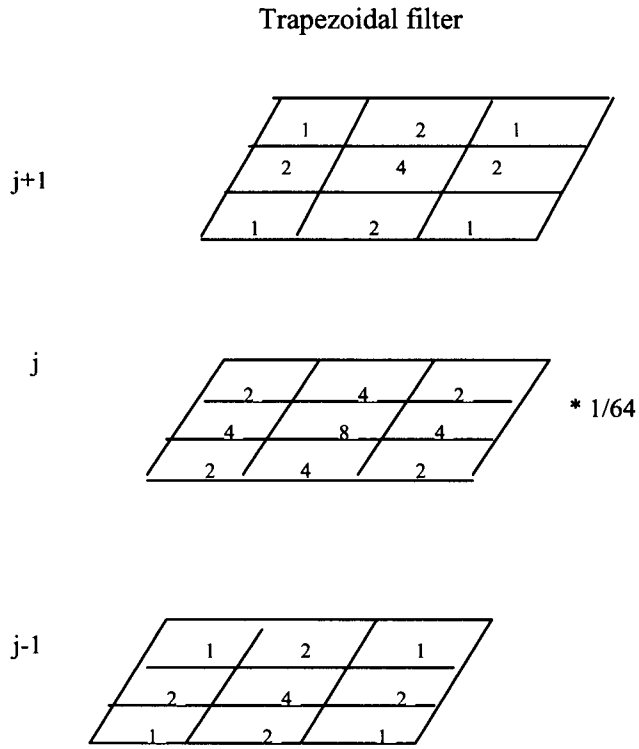

Figure 3.4 Trapezoidal filter in 3D.

The filters are used serially in each direction for three dimensions. The three dimensional trapezoidal filter is shown in Figure 3.4.

3.4 Numerical results

The lengths of the computational domain in the streamwise (x) and spanwise (z) direction are 3.0H and 1.5H respectively where H is the channel height. Periodic boundary conditions are imposed in the x and z directions. The schema of the channel flow is shown in Figure 3.5.

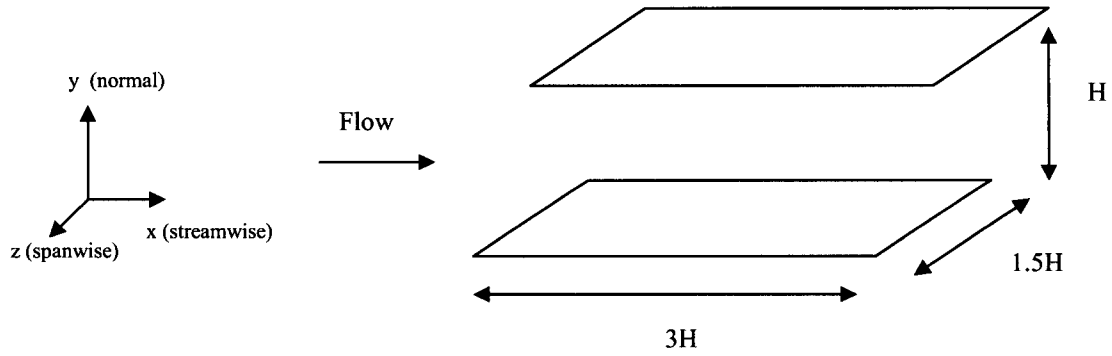

Figure 3.5 Schema of the channel flow

There is no wall model used in the simulations to be presented here. For the Smagorinsky model, a Driest damping function is used in (3.7). A no-slip wall condition is imposed in y direction. To resolve the near wall region, a nonuniform grid is used in the wall direction as in Moin and Kim (1982). The y coordinate is then:

$$y_j = \frac{1}{2} H(\tanh(a_0 \eta_j)/a + 1) \text{ (j} = 0,1,..., Ny-1). \tag{3.49}$$

where Ny is the total number of grid points in y direction. The quantity a is a stretching parameter $(0 < a < 1)$,

$$a_0 = \frac{1}{2}\log((1+a)/(1-a)),$$

$\eta_j = -1 + 2j\Delta\eta$ and $\Delta\eta = 1/(Ny-1)$. Here a = 0.98846 is used to get finer meshes near the wall.

3.4.1 Reynolds number $\mathrm{Re}_\tau = 395$

The parameters of the first test case have the following values:

$$\text{H} = 0.075 \text{ m},\ U_b = 0.204 m/s \text{ and } \nu = 1\times10^{-6} \text{ m}^2/\text{s},$$

Where U_b is the bulk velocity. The Reynolds number based on friction velocity is

$$\text{Re}_\tau = \frac{u_\tau \delta}{\nu} \approx 395$$

where $u_\tau = \sqrt{\tau_w / \rho}$ is the friction velocity , τ_w is the wall shear stress and δ is half of the channel height H. The Reynolds number based on bulk velocity is

$$\text{Re}_\delta = \frac{U_b \delta}{\nu} \approx 7650 .$$

The flow is turbulent since Re_δ is greater than $\text{Re}_{\delta,crit} \approx 575$ (White 1998).

The simulations are performed with three meshes. Table 3.2 gives the grid parameters.

Case	*Nx*	*Nz*	*Ny*	Δx^+	Δz^+	$\Delta y^+_{\min}$	$\Delta y^+_{\max}$
1	32	32	32	65.0	32.6	1.5	56.0
2	64	64	64	37.8	18.9	0.8	32.8
3	96	96	96	25.6	12.8	0.5	22.2

Table 3.2 Grid parameters for $\text{Re}_\tau = 395$

The initial mean velocity profile was generated by interpolating data obtained from a computation with the common $k-\varepsilon$ model. Random perturbations were added to the mean velocity distribution. The simulations 1, 2 and 3 correspond to the coarse, medium and fine mesh cases. The CFL number (CFL $= \dfrac{\Delta t}{\dfrac{1}{dtconv}+\dfrac{1}{dtdif}}$, where $dtconv = \min(|\dfrac{\Delta x}{U}|,|\dfrac{\Delta y}{V}|,|\dfrac{\Delta z}{W}|)$,

$dtdif = \min(\dfrac{\Delta x^2}{2(\nu+\nu_T)},\dfrac{\Delta y^2}{2(\nu+\nu_T)},\dfrac{\Delta z^2}{2(\nu+\nu_T)})$) is 0.15 for all three cases. The time steps are

0.002T, 0.0018T and 0.0012T, respectively, where T=H/U_b. The fluctuating velocities, u_i', are computed from:

$$u_i' = u_i - < u_i >,$$

where u_i is the instantaneous velocity and $< u_i >$ is the tempo-spatial average of the velocity field. Since x and z are two homogeneous directions, the data are collected at each xz -plane normal to the walls and averaged in each time step.

The computations are conducted with three SGS models: a constant Smagorinsky, a dynamic model and the ADM model. The Smagorinsky model uses the damping function of (3.7), where C_s is set to 0.1. The dynamic model computes the constant from (3.20). The relaxation coefficient χ_u is computed from (3.27) in the ADM model. The value of deconvolution order N is 5 if not specified.

As discussed in 3.2.2.1, the dynamic model involves two filters: the test filter and the grid filter. The trapezoidal rule is applied for test filter, which is illustrated in Figure 3.4. The total viscosity is restricted to positive values:

$$\nu_{tot} = \max(0, \nu + \nu_T).$$

Ghosal, *et al.* (1995) and Zang, *et al.* (1993) found that this restriction improved the numerical stability.

The dimensionless mean streamwise velocity profiles are shown in Figure 3.6 with the ADM model and the Smagorinsky model. The coarse mesh (Case 1) does not predict the logarithmic layer well. It shows some differences when compared with the direct numerical simulation (or DNS) data conducted by Moser, Kim and Mansour (1999), hereafter denoted by MKM. The medium mesh (Case 2) and fine mesh (Case 3) agree well with the profile of MKM. The results of the ADM model are better than those of the Smagorinsky model. Figures 3.7-3.9 present the resolved rms fluctuations: $\sqrt{u_i u_i}/u_\tau$ with two different models. Figure 3.10 shows the Reynolds stress $u'v'/u_\tau^2$.

Figures 3.7-3.9 show that the fluctuations from Case 1 are significantly different from those of MKM. This can be arributed to an inadequate gird resolution. The near wall region cannot be resolved with such a coarse mesh. The effective shear stress on the wall is reduced and so the streamwise non-dimensional fluctuations are overpredicted. The resolved fluctuations normal to the wall are underpredicted. The fluctuations found in Case 3 from two different subgrid models are close to those of MKM. The results from Case 2 are closer to those of Case 3.

Figure 3.11 shows the dimensionless mean streamwise velocity profiles from case 2 using three different SGS models. The improvement from the ADM model is clear in the comparison of the mean velocity profiles in Figure 3.11. The incremental improvement of mean velocity between ADM ($N=5$) and ADM ($N=10$) is small, indicating that good reconstruction of the unfiltered velocity is likely obtained with $N=5$.

The resolved rms fluctuations from the medium mesh case are presented in Figures 3.12 – 3.14. In the near wall region, the maximum value of the fluctuation *urms* for the ADM model is close to DNS value in Figure 3.12. The differences between the ADM model and the Smagorinsky model are small apart from wall regions.

In Figure 3.15, the dynamic coefficient $\sqrt{C(y)}$ and the van Driest damping on the Smagorinsky coefficient $C_s(1-e^{-y^+/25})$ are compared from the medium mesh case. The peak value of the dynamic coefficient is 10% higher than the constant Smagorinsky coefficient. In most of the computational region, the difference between the dynamic model coefficient and the Smagorinsky coefficient is less than 2%. So the results of the dynamic model and the Smagorinsky model are almost the same from Figures 3.11-3.14.

The ratio of the SGS eddy viscosity to the molecular viscosity in the direction perpendicular to the wall is shown in Figure 3.16 from case 2. The Smagorinsky model and the ADM model are used in this case. As the value of the ratio is less than 0.5 one can conclude that the effect of

different subgrid models is not very important for fully developed channel flow. It can be observed that the ratio of ADM model eddy viscosity to the molecular viscosity is not symmetric at $y/H = 0.5$. Numerical errors are most likely reponsible for the lack of simmetry observed.

The filter size near the wall region is small. The smallest value of y^+ is less than 1. The wall can be resolved well with the small mesh size near the wall as shown in Figures 3.6-3.14 except for the coarse mesh case. On the other hand, the filter size in the channel middle region is large. The value of y^+ can be 40 times larger than the smallest one. It is not surprising to find that the fluctuations are not well resolved in the core flow. The reason is that a streching mesh is used in the direction perpendicular to the wall, which increases the mesh size in the middle of the channel.

More grid points and coarse meshes near the wall can be used with the ADM model if the flow is expected to be well resolved in the middle region of the channel. It is known that the ADM model can alleviate the mesh restriction near the wall region from Stolz *et al.* (2001). Another alternative is using the wall model to remove the mesh restriction near the wall region (Sagaut 2001). But the wall model contains an additional source of error because a model is used for part of the flow dynamics.

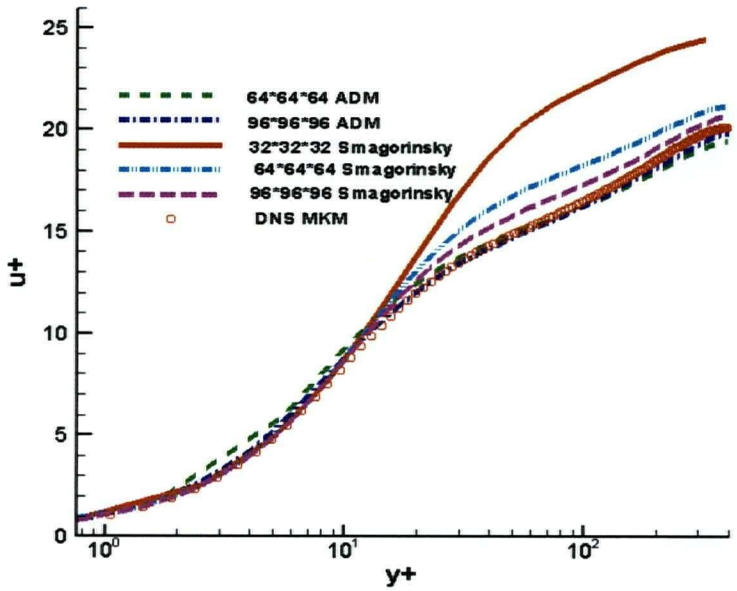

Figure 3.6 Dimensionless mean streamwise velocity profiles with the ADM model and the Smagorinsky model

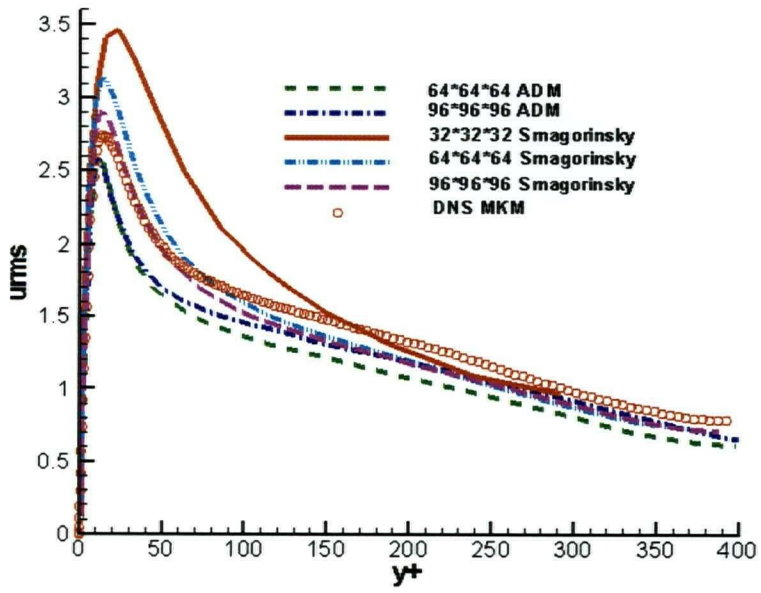

Figure 3.7 Dimensionless rms fluctuation of u: $\sqrt{u'u'}/u_\tau$ with the ADM model and the Smagorinsky model.

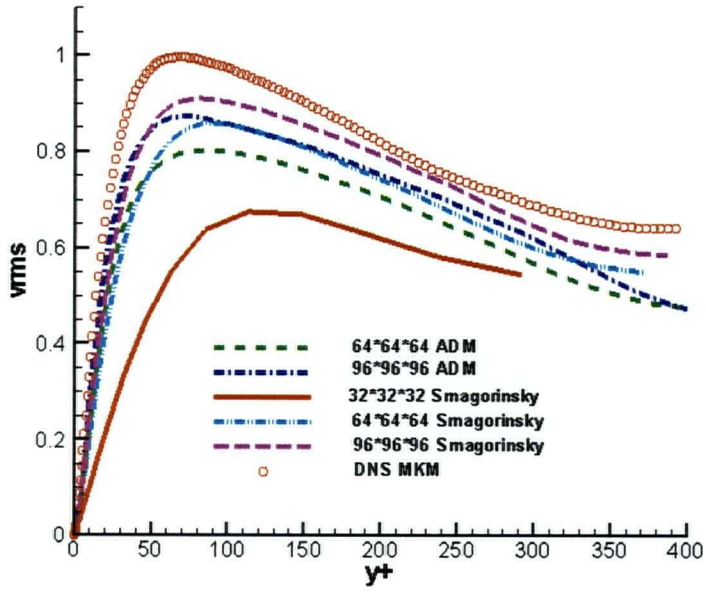

Figure 3.8 Dimensionless rms fluctuation of v: $\sqrt{v'v'}/u_\tau$ with the ADM model and the Smagorinsky model.

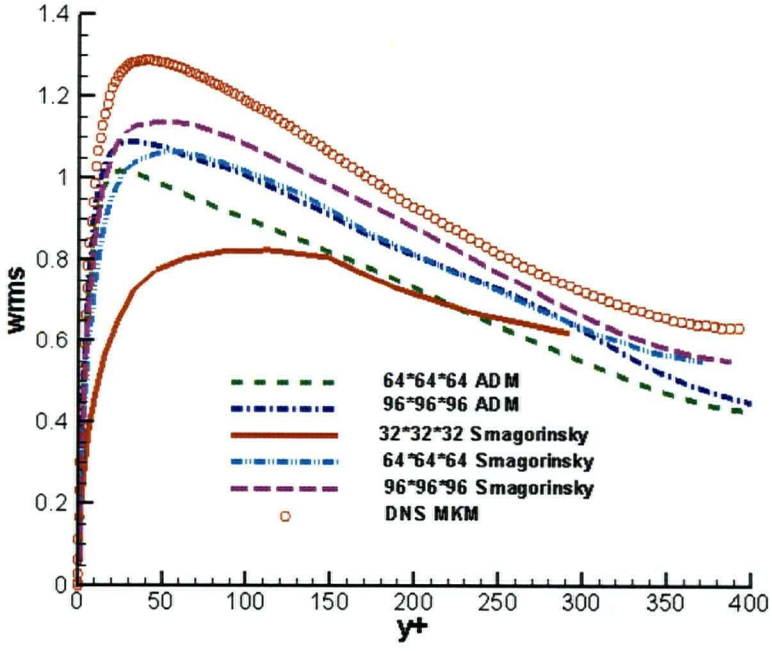

Figure 3.9 Dimensionless rms fluctuation of w: $\sqrt{w'w'}/u_\tau$ with the ADM model and the Smagorinsky model.

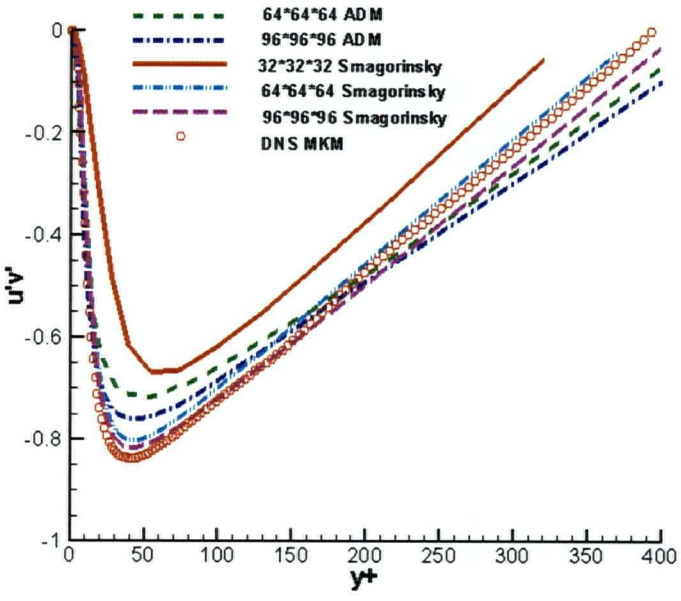

Figure 3.10 Dimensionless Reynolds stress: $u'v'/u_\tau^2$ with the ADM model and the Smagorinsky model.

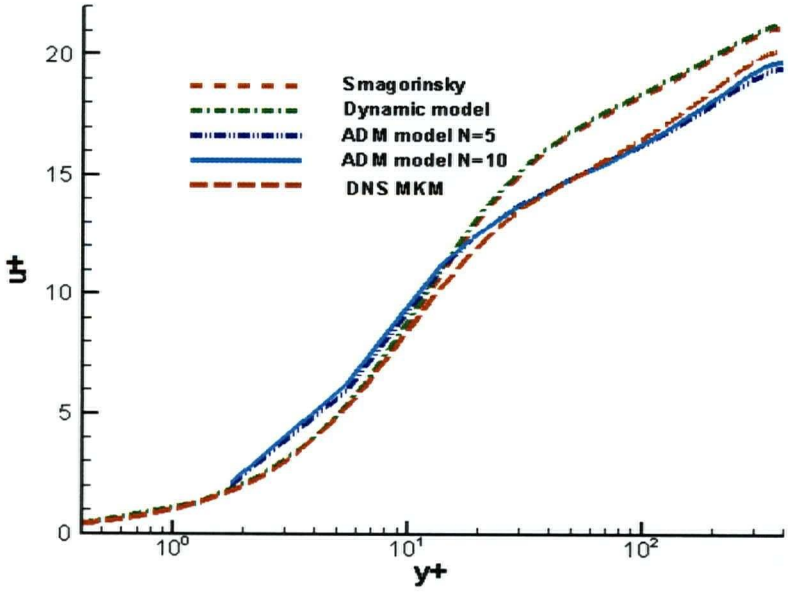

Figure 3.11 Dimensionless mean streamwise velocity profiles from the case 2.

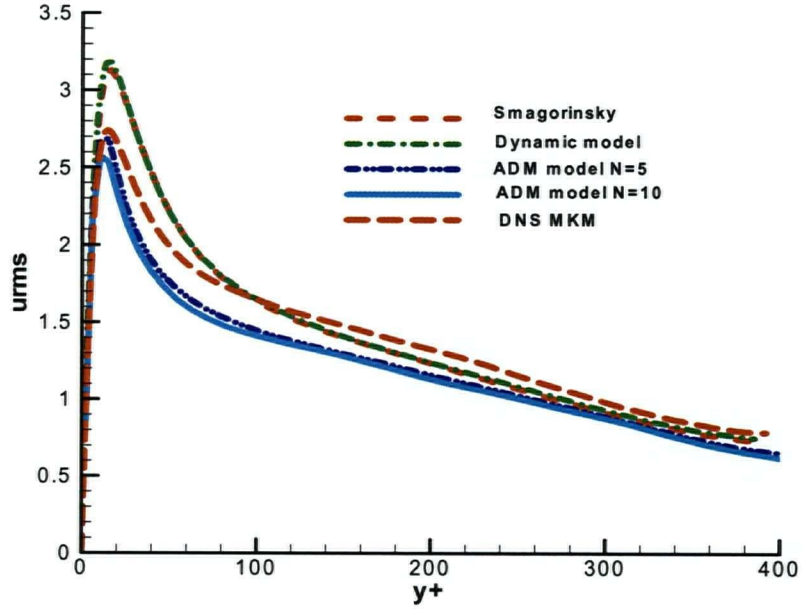

Figure 3.12 Dimensionless rms fluctuation of u: $\sqrt{u'u'}/u_\tau$ from the case 2.

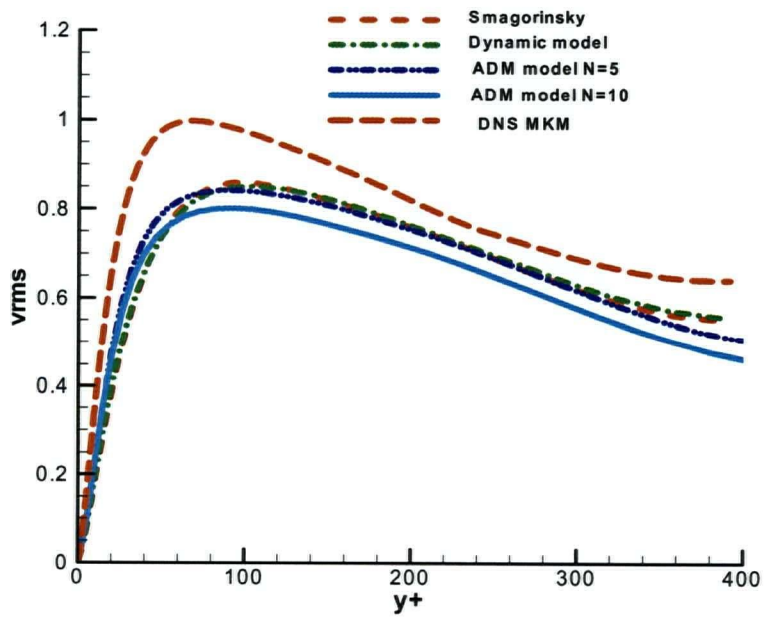

Figure 3.13 Dimensionless rms fluctuation of v: $\sqrt{v'v'}/u_\tau$ from the case 2.

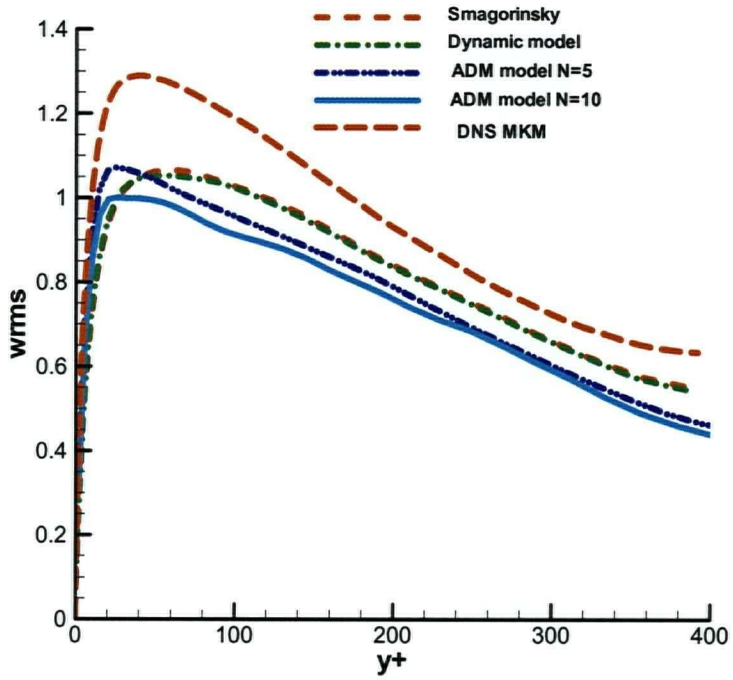

Figure 3.14 Dimensionless rms fluctuation of w: $\sqrt{w'w'}/u_\tau$ from the case 2.

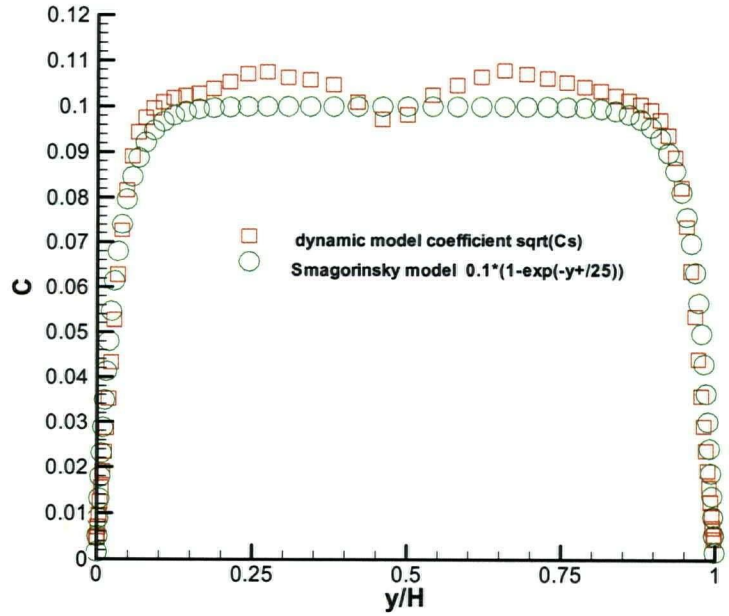

Figure 3.15 SGS model coefficients with the medium mesh case (case 2).

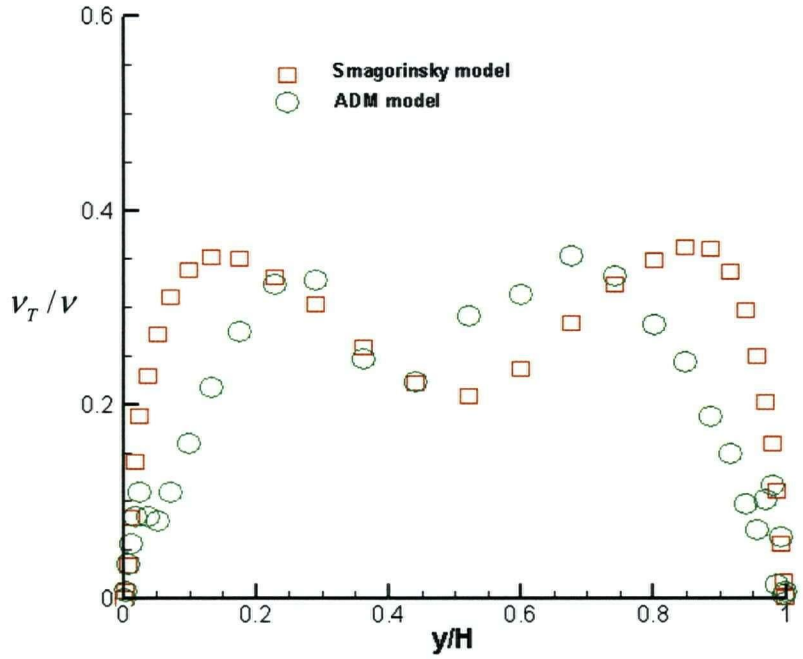

Figure 3.16 Ratio of SGS eddy viscosity to molecular viscosity: ν_T / ν with the Smagorinsky model and the ADM model (in case 2).

3.4.2 Results for Reynolds number $\mathrm{Re}_\tau = 1655$

The parameters of the second test case have the following values:

$$\mathrm{H} = 0.075 \text{ m}, \; U_b = 0.204 m/s \text{ and } \nu = 0.2441 \times 10^{-6} \text{ m}^2/\text{s},$$

Where U_b is the bulk velocity. The Reynolds number based on friction velocity is

$$\mathrm{Re}_\tau = \frac{u_\tau \delta}{\nu} \approx 1655$$

where $u_\tau = \sqrt{\tau_w / \rho}$ is the friction velocity , τ_w is the wall shear stress and δ is half of the channel height H. The geometry is the same as that with $\mathrm{Re}_\tau = 395$. The initial distribution comes from the previous $\mathrm{Re}_\tau = 395$ case. The grid parameters are shown in Table 3.3.

Case	*Nx*	*Nz*	*Ny*	Δx^+	Δz^+	Δy^+_{min}	Δy^+_{max}
1	96	96	96	101.1	51.6	2.1	89.4
2	96	96	128	101.1	51.6	1.2	51.6

Table 3.3 Grid parameters for $\mathrm{Re}_\tau = 1655$

The calculations are conducted with two mesh sizes: 96×96×96 and 96×128×96. The dimensionless mean velocity profiles are shown in Figure 3.17. There is no DNS data available at this high Reynolds problem. Spalding's (1961) formula quoted below, which covers the entire wall-region, is used as the reference profile, with $\kappa = 0.40$, $B = 5.5$:

$$y^+ = u^+ + e^{-\kappa B}\left[e^{\kappa u^+} - 1 - \kappa u^+ - \frac{(\kappa u^+)^2}{2} - \frac{(\kappa u^+)^3}{6}\right].$$

It is shown that the ADM model provides an obvious improvement for the mean velocity profiles. The reason is that the ADM model uses an explicit filter and recovers a part of small scales from the large scales directly.

The dimensionless resolvable turbulence intensities and Reynolds stress are presented in Figures 3.18-3.20. WW (1989) is the reference experimental data measured by Wei and Willmarth (1989) at $\mathrm{Re}_\tau = 1655$. The results from the Smagorinsky model are a little better than those from the ADM model.

From above results, only the resolved scales quantities are shown. If the small scale is added, the computational results are closer to the experimental data, but the difference is less than 10%. The dimensionless resolvable turbulence intensities plus the small scale part (from the model) with ADM model are shown in Figure 3.21-3.22.

The difference between numerical results and the experimental data can be seen clearly above $y^+ > 200$ region. One reason is that the nonuniform mesh from (3.49) is used, where the mesh

ratio is large away from the wall region. It is expected to get better solutions with more finer mesh or a higher accuracy scheme. It is noted that the shear velocity is used as a non dimensional parameter. Since u_τ varies between the different cases and its vaue is very small, using the shear velocity as a non dimensional parameter somewhat exaggerates the differences between different cases.

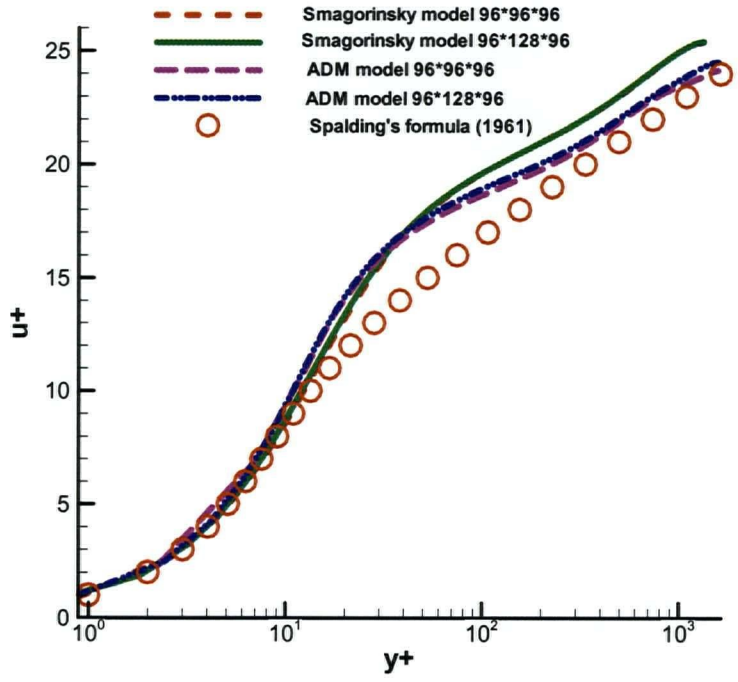

Figure 3.17 Dimensionless mean streamwise velocity profiles at $\mathrm{Re}_\tau = 1655$.

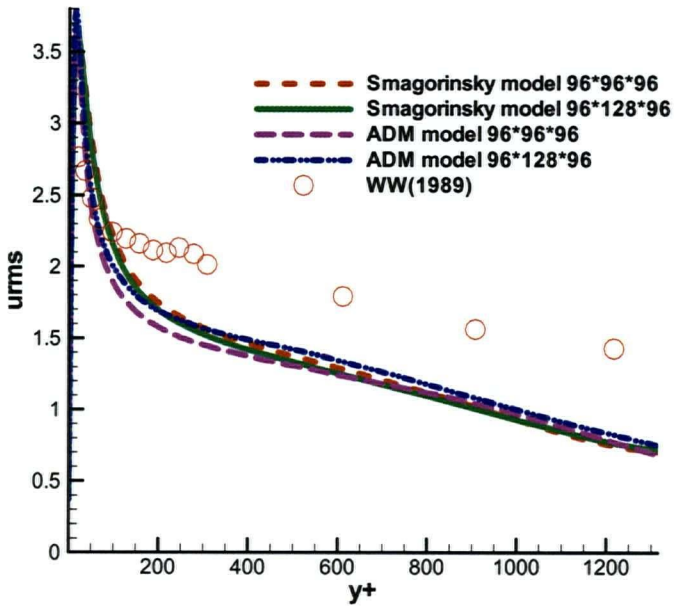

Figure 3.18 Dimensionless rms fluctuation of u: $\sqrt{u'u'}/u_\tau$ at $\mathrm{Re}_\tau = 1655$.

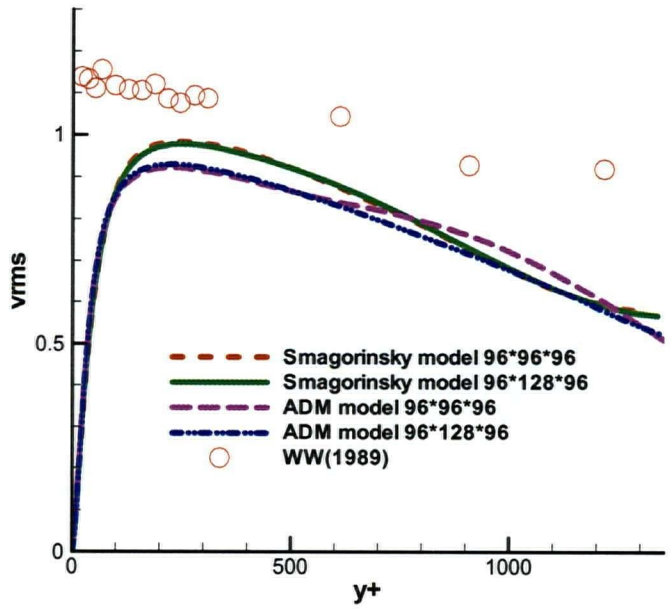

Figure 3.19 Dimensionless rms fluctuation of v: $\sqrt{v'v'}/u_\tau$ at $\mathrm{Re}_\tau = 1655$.

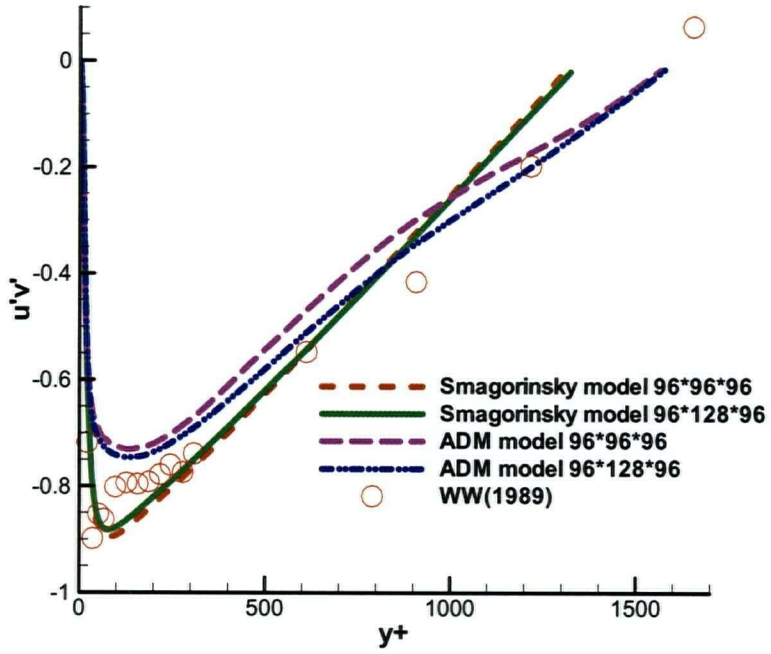

Figure 3.20 Dimensionless Reynolds stress: $u'v'/u_\tau^2$ at $\mathrm{Re}_\tau = 1655$.

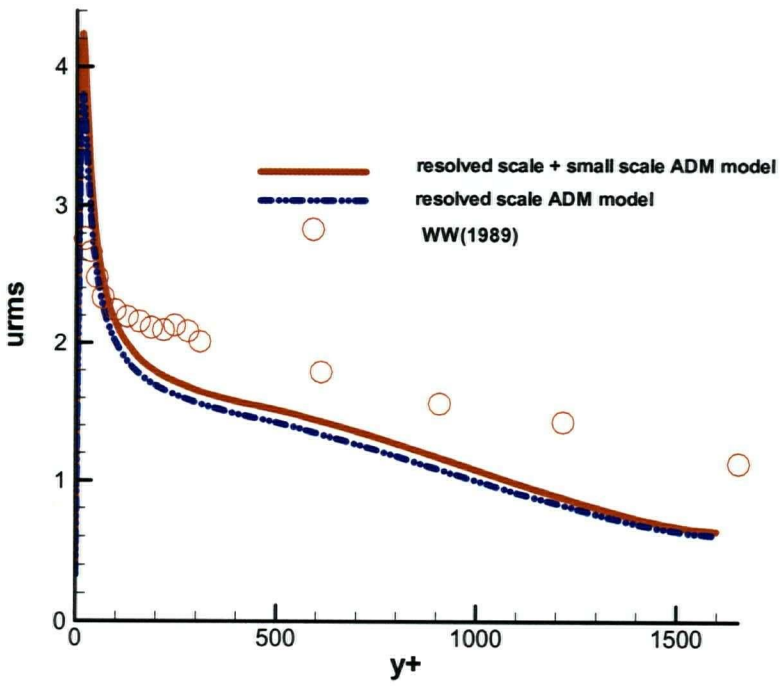

Figure 3.21 Dimensionless rms fluctuation of u: $\sqrt{u'u'}/u_\tau$ with 96×128×96 mesh.

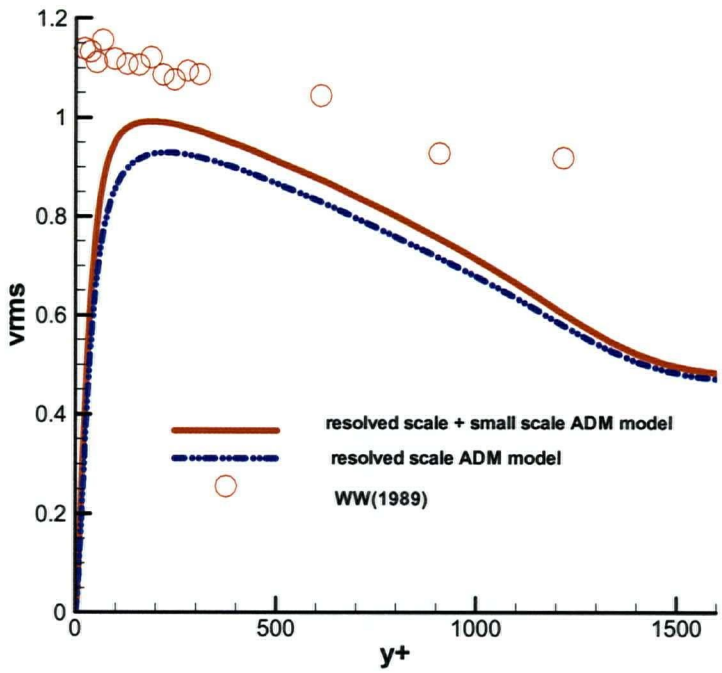

Figure 3.22 Dimensionless rms fluctuation of v: $\sqrt{v'v'}/u_\tau$ with $96\times128\times96$ mesh.

3.5 Summary

The Navier-Stokes equations were solved using a staggered finite volume method for a generalized curvilinear coordinate system. The fractional step method was used to solve the momentum equations. A Poisson equation for pressure was obtained to satisfy the continuity equation. For the channel flow, the fast Fourier transform and the cyclic reduction method were presented to solve the Poisson equation.

For parallel computation of a large eddy simulation, the domain decomposition approach is used to partition the data. Each sub-domain data is assigned to one processor to calculate the quantities and exchange the boundary data with neighbors. The parallel efficiency is still higher than 80% for the parallel computation of a large eddy simulation.

The channel flow at Re_τ = 395 was modelled first with three different SGS models utilizing three alternative mesh sizes. The coarse mesh case did not predict the logarithmic layer well, which can be arributed to an inadequate grid resolution. The fine mesh case was close to the reference DNS result. The medium case was close to the fine mesh case. The Smagorinsky SGS model shows little difference from results obtained with the dynamic SGS model. The peak value of the dynamic coefficient was 10% higher than the Smagorinsky coefficient. In most of the computational region, the difference between the dynamic model coefficient and the Smagorinsky coefficient is less than 2%. The ADM model improves the mean velocity profile compared to the Smagorinsky model. The reason is that the ADM model uses an explicit filter and recovers a part of small scales from the large scales directly. The resolved turbulence intensities with the ADM model are close to the Smagorinsky model results.

At the higher Reynolds number Re_τ = 1655, the channel flow was computed by using two mesh sizes. The trend in the calculations was similar to that of the low Reynolds number case.

The Smagorinsky model with $64\times64\times64$ mesh can provide a good representation of channel flow and is used to provide inflow conditions for the modelling of the converging section as described in chapter 4. The ADM model can improve the mean velocity profile using the explicit filter. But the ADM model needs much more computational time than the Smagorinsky model, and so it will be used only for model comparisons in chapter 4 and chapter 6. The objectives 1 and 2, described in chapter 1, are achieved.

Chapter 4 LES for Turbulent Flow through a Converging Section

4.1 Introduction

As described in chapter 1, the rapidly converging section of a paper-machine headbox carries a dilute concentration of pulp fibers in water to the wire mesh where the fibers are dried to become paper. Ideally, the mean velocity distribution in the stock (fibers and other substances in fluid suspension) leaving the converging section (or slice) should be uniform over the paper thickness direction and across the entire span of the converging section exit. Otherwise, the non-uniform stock can result in defects in the paper being produced by the machine.

To achieve good paper formation, there must be no fiber flocculation in the jet exiting the headbox. The turbulence produced in the converging section does not affect the mean flow distribution significantly, but it is critically important in preventing unwanted fiber flocculation and in providing a degree of dispersion and preferential orientation of the fibers. A detailed understanding of this turbulence is therefore essential in order to study the fiber motion and to predict the quality of the paper produced.

Shariati (2002) has studied the flow in the converging section of a headbox both experimentally and numerically. The experimental headbox that he used is a laboratory scale model of a typical headbox with the size reduced by a factor of 5. Shariati made LDV (Laser Doppler Velocimeter) measurements of mean and fluctuating components of the velocity in the headbox. He also compared results using the $k-\varepsilon$ model and a Reynolds stress model (RSM) to his experimental measurements. He found that the turbulence kinetic energy predicted with the $k-\varepsilon$ model was much too high near the slice exit. The RSM model provided better agreement with the

experimental measurements. However, the RSM model cannot provide the instantaneous velocity distribution which is required to predict the fiber motion in the converging section.

In this chapter, a large eddy simulation computation of the converging section is presented. The geometry of the converging section is the same as that of the experimental headbox used by Shariati (2002). The calculated time-averaged turbulence components predicted by the LES are compared to Shariati's measured values. Different inflow conditions are explored. Qualitatively, the calculated and observed turbulence distributions follow similar trends. More exact inflow conditions for the turbulence must be introduced into the calculated LES results if better agreement is to be obtained. This aspect of the present work needs further investigation.

The results of flow simulation are presented in section 4.2. Some discussions are presented in section 4.3. A summary is given in section 4.4.

4.2 Flow simulation

4.2.1 Experimental setup

The experiments were performed by Shariati (2002) at the University of British Columbia. The experimental set-up used a closed flow system, diagrammatically shown in Figure 4.1.

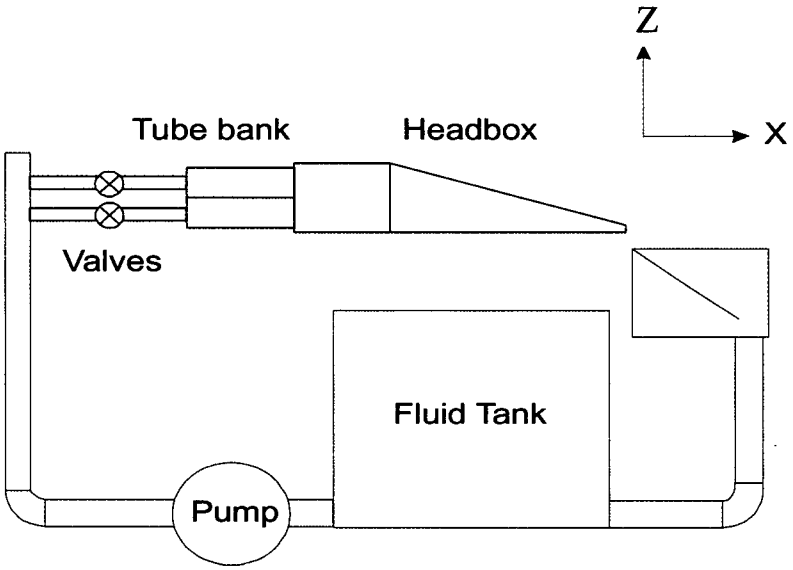

Figure 4.1 Flow loop in the experiment (from Shariati 2002).

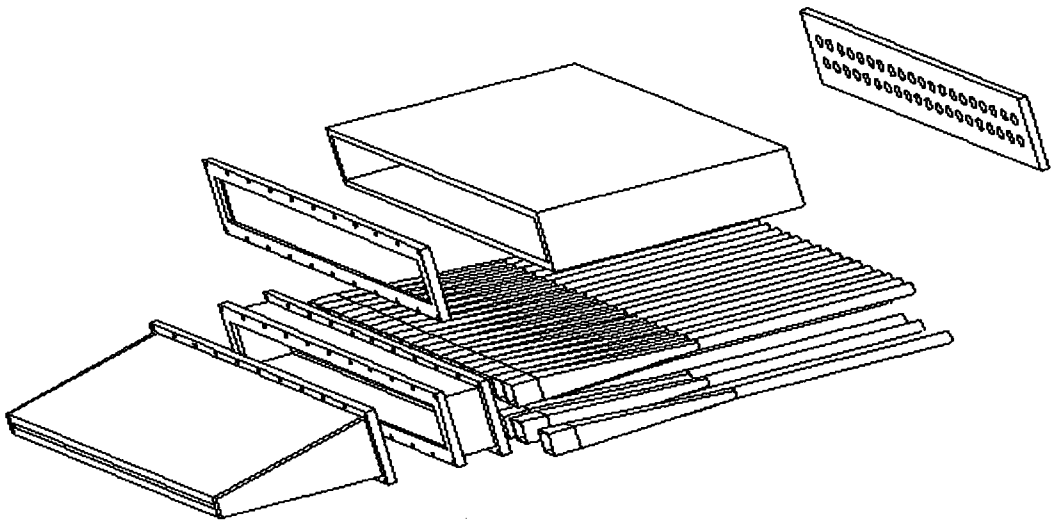

Figure 4.2 Experimental headbox drawing (from Shariati 2002).

The headbox drawing is shown in Figure 4.2. In the flow loop, water is pumped from the reservoir tank to the headbox through the pipes and rectifier tubes. The rectifier tubes (or diffusers)

are round at the inlet and rectangular at the outlet with slowly increasing cross sectional areas. They are used to provide turbulence energy for the flow and to generate a fairly uniform velocity profile at the converging section inlet. In this headbox model, there are 40 rectifier tubes, two rows in the vertical or height direction and 20 each in the spanwise or horizontal direction. The headbox section starts with a rectangular channel, which remains constant in the cross section area until the length reaches 0.075 m. Table 4.1 shows the geometry of the converging section. By means of LDV, Shariati (2002) measured the mean velocity and the rms velocity along the centerline of the converging section.

Parameters	**Values (m)**
Width	0.75 (constant)
Inlet height	0.075
Slice height	0.0075
Contraction ratio	10
Length	0.3

Table 4.1 The geometry of the converging section.

4.2.2 Numerical simulation of the converging section

The numerical method is the same as that of chapter 3 for fully developed channel flow. The Poisson equation is solved with FFT and CGSTAB method. The subgrid model uses the constant Smagorinsky model or the ADM model. All the calculations are performed with parallel computation, as described in chapter 3, on the P4-Xeon Cluster with a Myrinet network at the University of British Columbia.

The computational domain is shown in Figure 4.3. In the z direction, no-slip wall boundary conditions are imposed along the solid walls. The spanwise direction, y, is treated as periodic. At the inlet plane the unsteady distributions for the velocity components are generated by a separate LES of

fully developed channel flow. Different inflow conditions that simulate the turbulence produced by the rectifier tubes are discussed later. At the exit plane, one possibility is to set all derivatives in the direction normal to the boundary to zero. This condition is often used in steady flow. For unsteady flow, the convective boundary condition (Kaltenbach 1998, Kaltenbach *et al.*1999)

$$\frac{\partial u_i}{\partial t} + U_c \frac{\partial u_i}{\partial x} = 0 \tag{4.1}$$

is employed. U_c is set to the mean streamwise velocity at the exit plane. This condition (4.1) eliminates most of the problems caused by pressure waves reflecting from the outflow condition. The dimensions of the computational domains are the same as the dimensions of the experimental apparatus shown in Figure 4.2 except for the width in the spanwise direction. The computational domain spanwise width is approximately three inlet heights. The $64\times64\times64$ mesh is used. The meshes are uniform in the streamwise direction and the spanwise direction. A non-uniform grid is used in the normal wall direction to resolve the near wall region as in chapter 3 (formula 3.49).

The measured and calculated mean streamwise velocities along the centerline of the converging section (line ABC in Figure 4.4) are shown in Figure 4.5. The velocity is non-dimensionalized with the bulk velocity at the inlet of the converging section, $U^* = U / U_b$. Here $X^* = x / Lx$ is the x position normalized with the total length of the converging section L_x. The computed values of the mean velocity agree well with the measured values. The resolved rms fluctuations u', v' and w' normalized by u' at the inlet (u'_{in}) are presented in Figures 4.6 – 4.8. The rms fluctuation of the velocity in the x direction, u' diminishes towards the exit, while w' in the z direction increases. The trend of the calculated results from u' and w' is the same as that of the experimental results, but there are some differences between them, particularly in the region between the inlet of the converging section and the first third of the converging section. The computed v' increases along the center line, while the measured v' decreases in the same region. These

differences can be attributed to the difference between the measured and assumed inflow conditions. Also the expermental flows settings have some errors that produce secondary flows. From the experiment, the two rows of tubes can generate much higher turbulence than the single channel which is used as the model in above calculations. It can also be observed that the computational inlet turbulence intensity is less than one half of the measured value at 0.03m from the inlet plane (DE line in Figure 4.4) in Figure 4.10. Figure 4.9 shows the turbulence kinetic energy k nondimensionalized by k at the inlet of the position 0.006m after the convergence starts. The turbulent kinetic energy predicted by LES and the standard $k-\varepsilon$ model in most of regions is close to the measured values, but the computed values with the standard $k-\varepsilon$ model increase rapidly towards the exit. The reason is that the standard $k-\varepsilon$ model includes a turbulence generation term that depends on $\partial U/\partial x$. That term becomes very large close to the exit of the converging section and causes a break down of the model. Also, the standard $k-\varepsilon$ often fails to predict the turbulence kinetic energy where the turbulence is significantly anisotropic such as the case in the region close to the exit of the converging section.

To consider the effect of the different inflow conditions, a "two-channel" inflow condition is constructed. The inflow condition is linearly interpolated from two half-inlet heights of the converging section channels where one channel is located above the other channel (Figure 4.11). Each channel is then 0.037 m high and the wall thickness is 0.001 m, the total of the two channels and wall thickness making up the 0.075m inlet height of the headbox. The wall thickness is explicitly considered in the generation of the inflow condition. The comparison of the mean streamwise velocity along the centerline of the converging section is shown in Figure 4.12 with the "two-channel" inflow conditions. There is no significant difference between the two velocity variations. Figures 4.13-4.15 present the comparison of rms fluctuations u', v' and w' normalized by u' at the inlet (u'_{in}) with two inflow conditions. The results of the "two-channel" inflow conditions are better

than that of the one channel inflow condition, matching the trend of the measured values from u' and w' but not reproducing them with real accuracy. There is no improvement with "two-channel" inflow conditions for v'. This appears to be related to the impossiblity to set accurately the flow in the experiment and to the inflow data used in the simulations. The inflow turbulence condition clearly affects the numerical result and better agreement could probably be obtained if the turbulence at the inflow section could be more precisely modelled in the calculations.

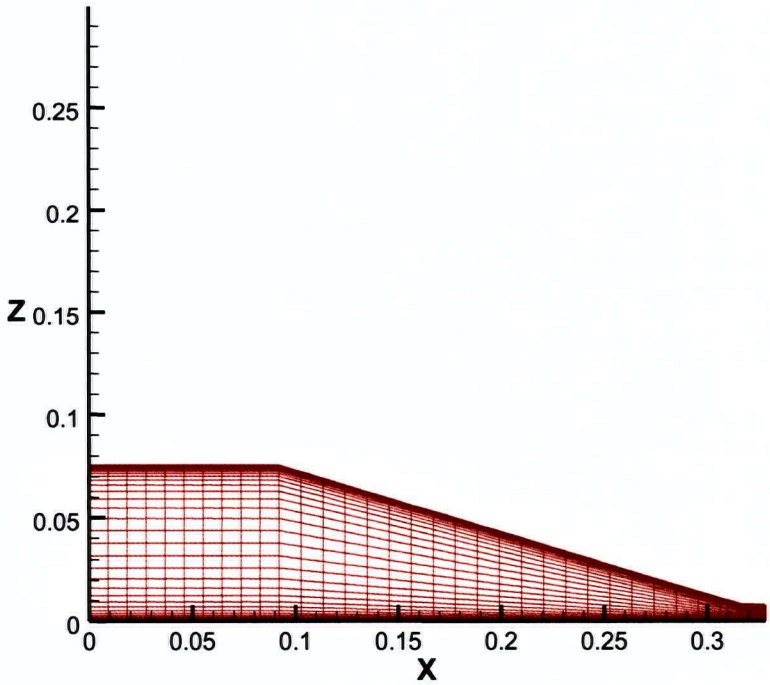

Figure 4.3 Computational domain for the converging section. Only a subset of the actual grid is plotted.

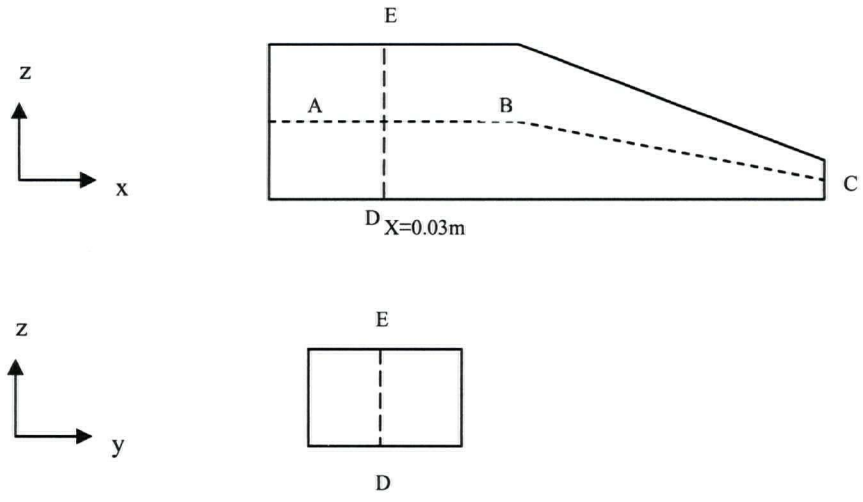

Figure 4.4 Measurement locations along the centerline of the converging section (line ABC) and the vertical line at 0.03m after inlet (line DE).

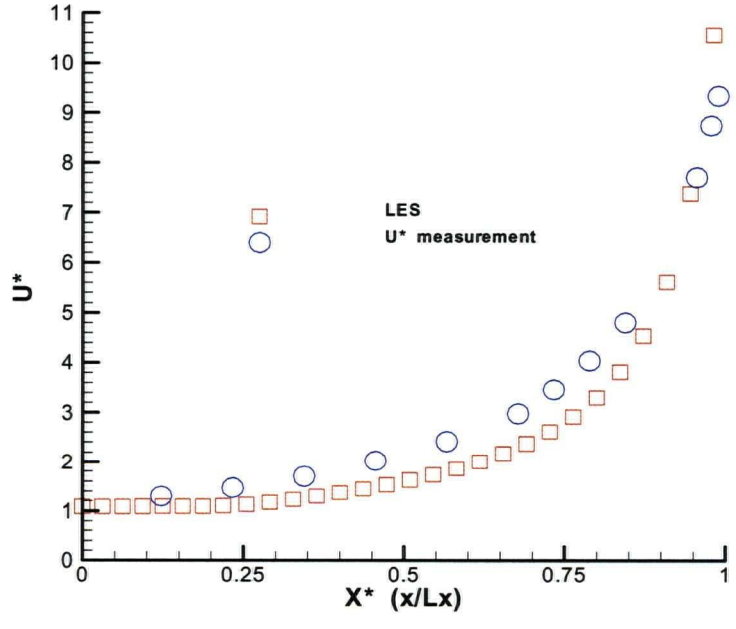

Figure 4.5 Comparison of the mean velocity at the centerline of the converging section.

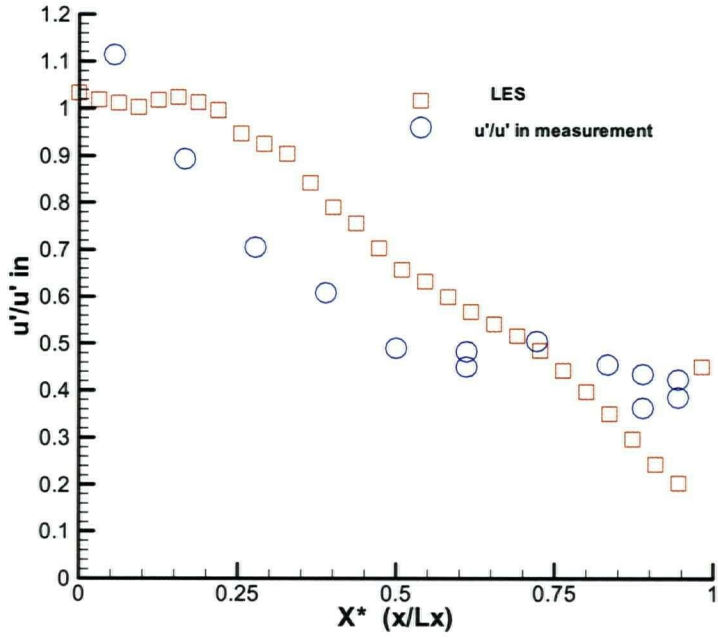

Figure 4.6 Comparison of rms value of the velocity fluctuation u' normalized by u'_{in}.

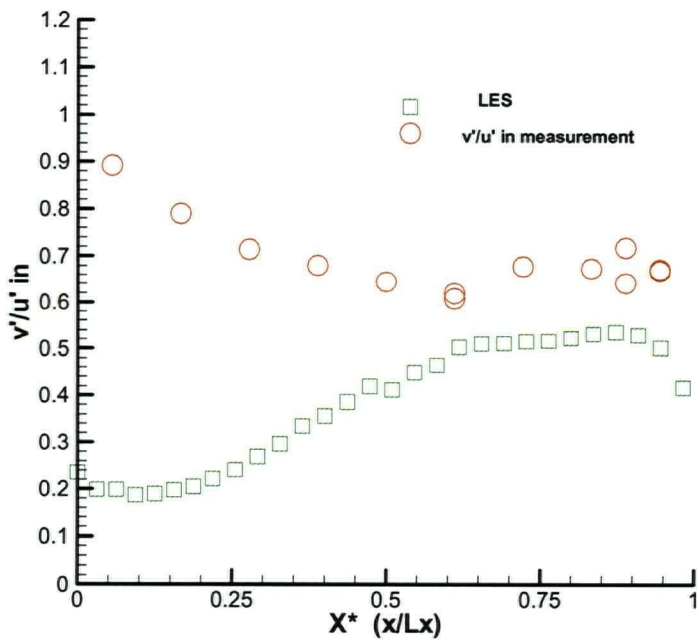

Figure 4.7 Comparison of rms value of the velocity fluctuation v' normalized by u'_{in}.

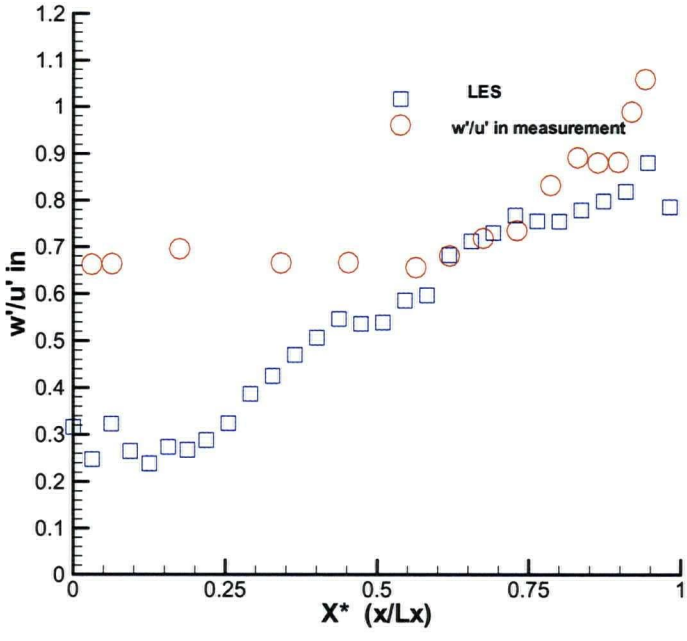

Figure 4.8 Comparison of rms value of the velocity fluctuation w' normalized by u'_{in}.

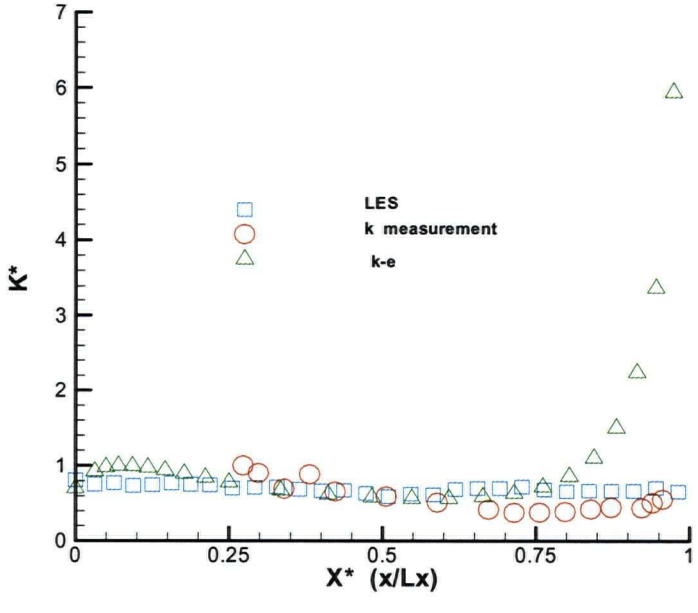

Figure 4.9 Comparison of turbulence kinetic energy k nondimensionalized by k at the inlet of the position 0.006m after the convergence starts.

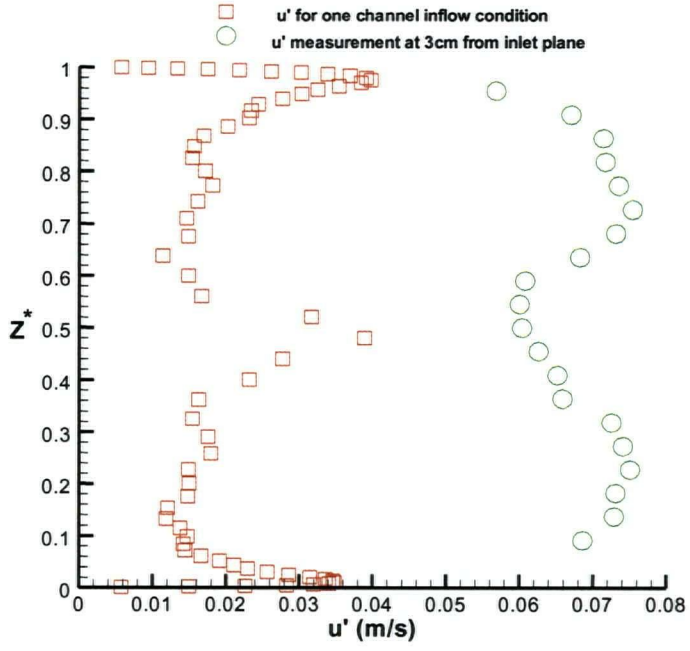

Figure 4.10 Comparison of the fluctuating velocity u' at inlet for one channel inflow condition with the measured value at the vertical line (DE line in Figure 4.4) at the location 0.03m from the inlet.

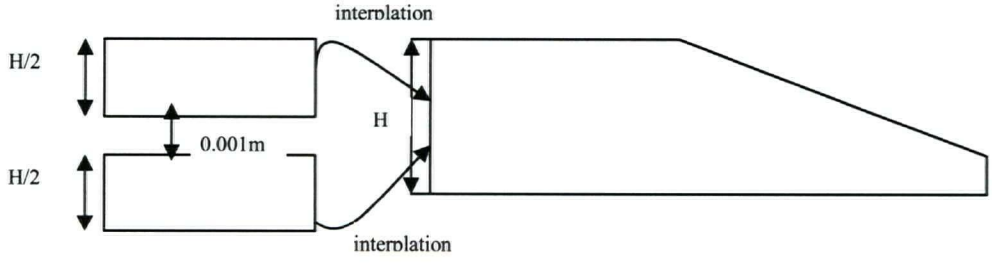

Figure 4.11 The diagram of " two-channel " inflow condition.

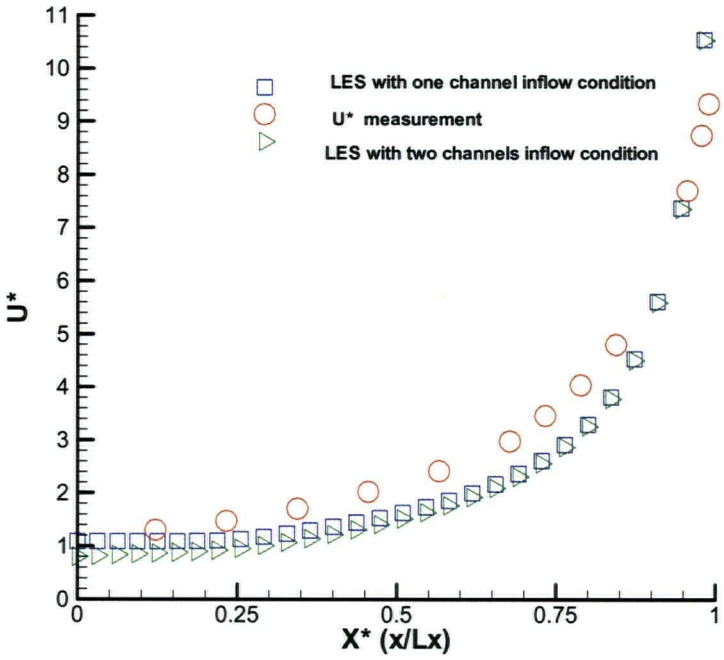

Figure 4.12 Comparison of the mean velocity at the centerline of the converging section with different inflow conditions.

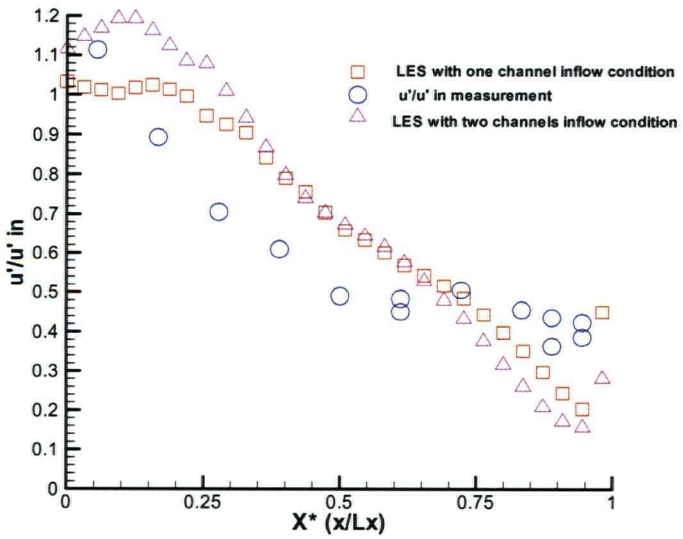

Figure 4.13 Comparison of rms value of the velocity fluctuation u' normalized by u'_{in} with different inflow conditions.

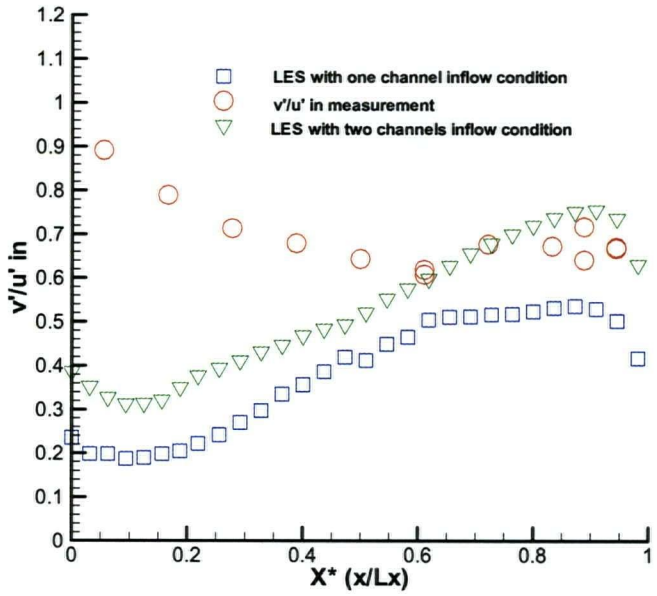

Figure 4.14 Comparison of rms value of the velocity fluctuation v' normalized by u'_{in} with different inflow conditions.

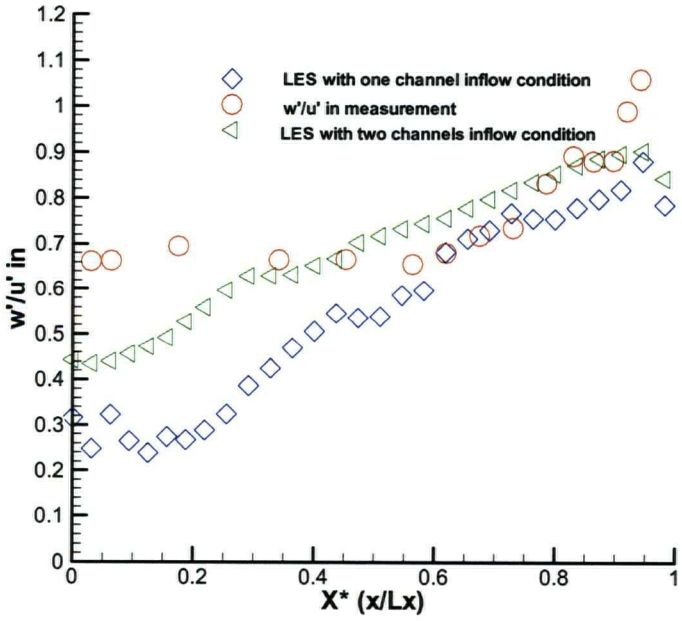

Figure 4.15 Comparison of rms value of the velocity fluctuation w' normalized by u'_{in} with different inflow conditions.

4.2.3 Alternative methods for the generation of inflow data

It appears that the turbulence levels near the inlet of the channel are lower than measured values so that some new method for prescribing inlet conditions needs to be considered. The most straightforward way to get the appropriate inflow condition for the converging section is to include the entire length of rectifier tubes in the calculation. This procedure would be a very costly venture in terms of computational effort. Furthermore, the inflow condition for the rectifier tubes is also needed to start this calculation. The simplest way to generate turbulent inflow conditions is to superpose random fluctuations on a desired mean velocity profile. The amplitude of the fluctuations can be estimated from a desired set of one–point second-order turbulence statistics. This approach has been employed to generate the inflow condition in, for example, Lee *et al.* (1992) and Rai and Moin (1993). This method requires a fairly lengthy straight section to allow for the development of the appropriate organized turbulent motion, which is not available in this converging section application. Bonnet *et al.* (1997) propose an approach to recover the two-point correlations of the inflow by using linear stochastic estimation. But this requires knowledge of the time history of the velocity at a few reference points and of the two-point spatial correlations tensor. These requirements can not be met from the experimental data. Lund *et al.* (1998) developed an extracting/rescaling technique to generate turbulent inflow data for spatially developing boundary layer simulations. Their method consists of the following steps:

1. Extract mean values and fluctuations from a down stream plane.
2. Rescale the preceding values according to boundary-layer similarity.
3. Reintroduce the rescaled values at the inlet plane.

This method is shown to be highly accurate for spatially developing boundary layer simulations from Lund *et al.* (1998). For the converging section, there is no boundary layer similarity theory. Nevertheless, a modified Lund's method is constructed to generate the inflow data in this case. The geometry is the same as the channel flow geometry. The inflow obtained using the random

fluctuation method (see appendix C) is set to have the similar mean profile and Reynolds stress tensor distributions as those produced by Shariati (2002) using the RSM model for the inlet condition of the converging section. As before, the outflow condition is the convective boundary condition (4.1). The simulation is run to a statistically stationary state. The fluctuation values are extracted from a rescaling station (middle plane of the channel) shown in Figure 4.16. The rescaling values are not obtained from boundary-layer similarity as was done by Lund *et al.* (1998). In the present case, they all have a common factor, the ratio of the computational rms velocity fluctuation u' and the experimental value at the centerline of the converging section. The rescaled values are put back as the inflow data. After many time steps, the instantaneous velocity distribution on the exit plane is written to disk as the inflow data for the converging section.

The new inflow rms velocity fluctuation u' and the measured value at 0.03m from the inlet plane (line DE in Figure 4.4) are shown in in Figure 4.17. The result is much better than that in Figure 4.10. Figure 4.18 shows the new inflow mean streamwise velocity and the measured value of the same velocity along a vertical line near the channel entrance (line DE in Figure 4.4). Note that the measured values are for a location slightly downstream of those used for the inlet conditions but that there would be essentially no change in the streamwise direction if the channel were long and had fully developed flow. There is a reasonable agreement between the new inflow values and their measured counterparts.

Using the new inflow data, the calculation of the converging section in section 4.2.2 is repeated. Figure 4.19 shows the new mean streamwise component of the velocity along the vertical line (line DE in Figure 4.4). The computational velocity profile is similar to the measured profile. The values of the streamwise fluctuating component of velocity at the same location as Figure 4.19 are presented in Figure 4.20. The computational results are in reasonable agreement with the measured data. It is observed that there are still differences between the computational values and the experimental results in the middle region. One reason for this difference could be that the mesh is

coarse in the middle region because the streching mesh is used in the wall direction. The mean streamwise velocity along the centerline of the converging section is shown in Figure 4.21. The computed values of the mean velocity agree well with the measured values. The resolved rms fluctuations u', v' and w' normalized by u' at the inlet (u'_{in}) are presented in Figures 4.22 –4.24. The Figures 4.22 and 4.24 are almost the same as those computed from the earlier one channel inlet condition and plotted in Figures 4.6 and 4.8. From Figure 4.23, the resolved rms fluctuation v' with the new inflow condition is better than that using the one channel inflow condition of Figure 4.7. The difference between w' from LES and the measured values remains quite large near the inlet region. The inlet conditions need further improvement. The turbulence kinetic energy k non-dimensionalized by k at the inlet of the position 0.006m after the convergence starts with the new inflow condition is shown in Figure 4.25. There is little difference between the new inlet condition and one-channel inlet condition.

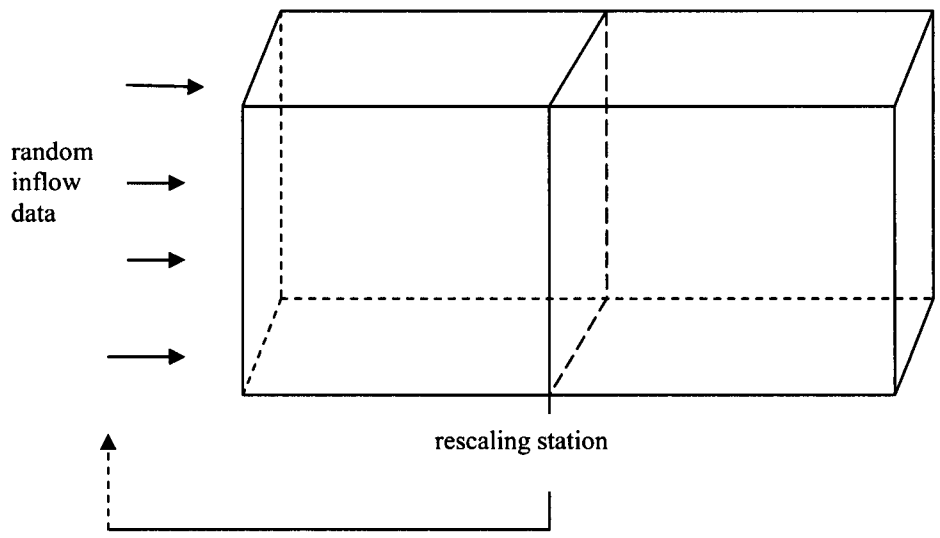

Figure 4.16 Schematic of new inflow generation technique.

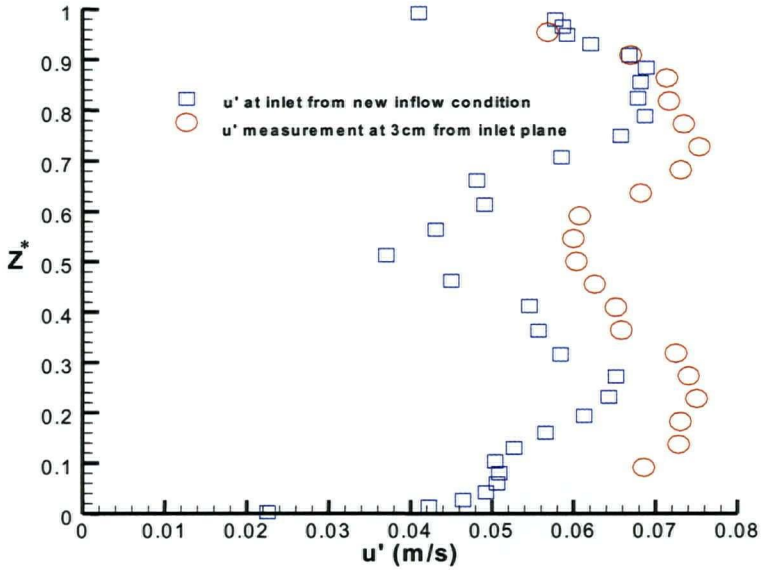

Figure 4.17 Comparison of rms value of the velocity fluctuation u' at inlet with the measured value at the vertical line (line DE in Figure 4.4) of the location 0.03m from the inlet.

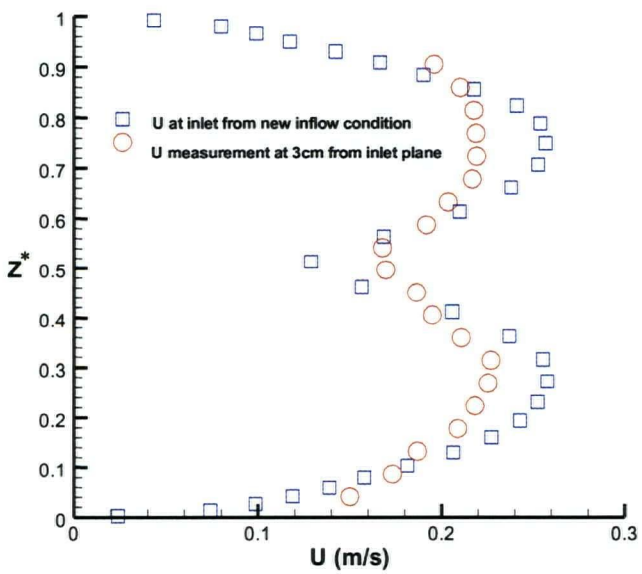

Figure 4.18 Comparison of streamwise component of the mean velocity at the inlet with the measured value at the vertical DE line (in Figure 4.4) located 0.03m from the inlet.

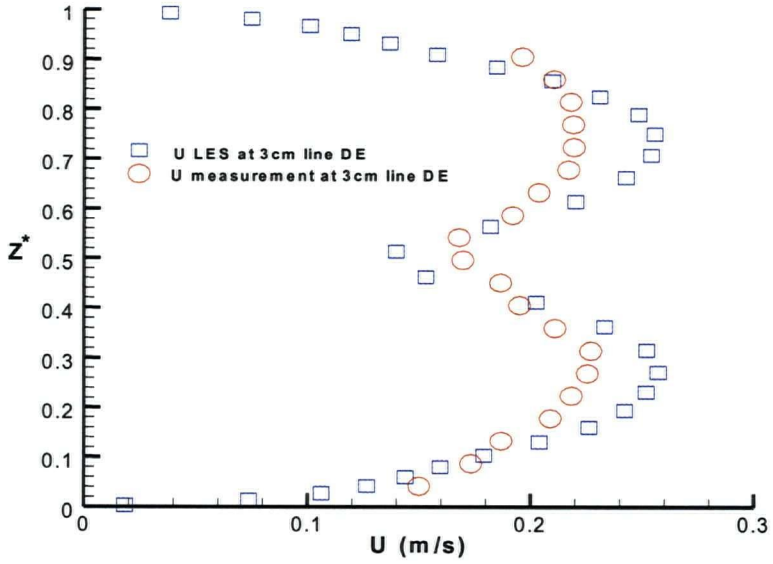

Figure 4.19 Mean streamwise velocities calculated with the new inflow condition at the vertical line (DE line in Figure 4.4) compared with measured values at the same location.

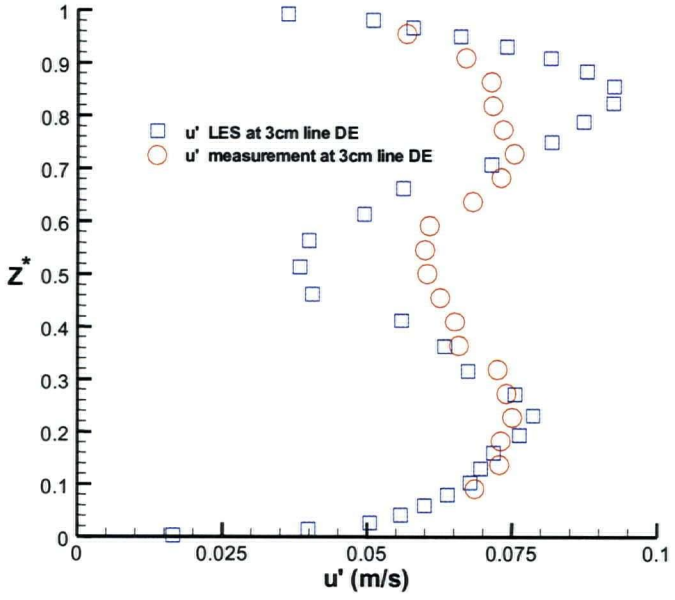

Figure 4.20 Comparison of rms value of the velocity fluctuation u' at the vertical line (DE line in Figure 4.4) with new inflow condition.

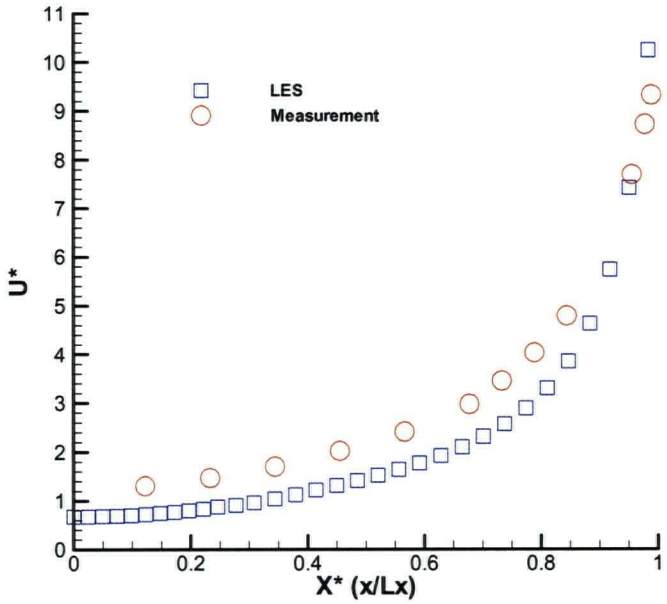

Figure 4.21 Mean velocity at the centerline of the converging section calculated with new inflow condition compared to measured values at the same location.

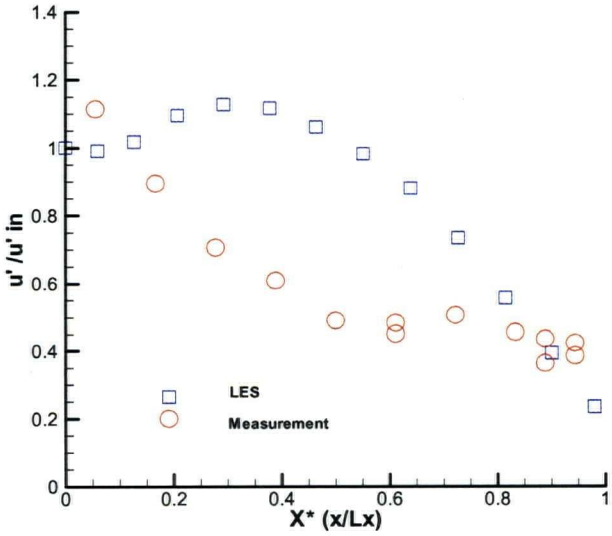

Figure 4.22 Comparison of rms value of the velocity fluctuation u' normalized by u'_{in} calculated with the new inflow condition.

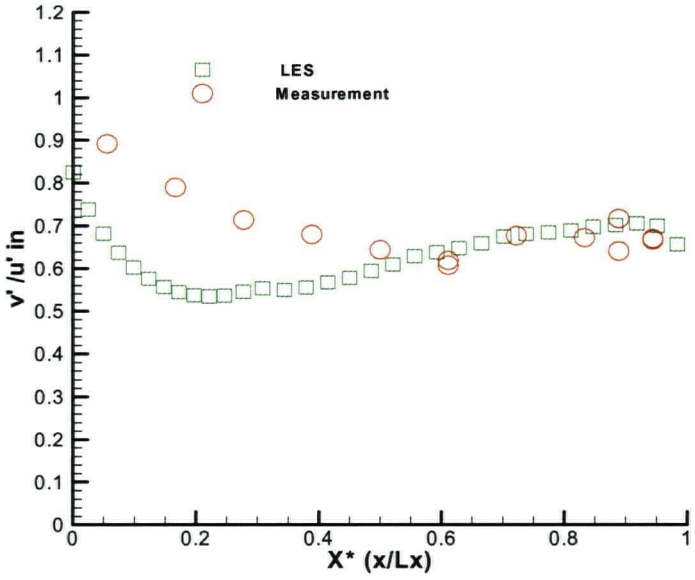

Figure 4.23 Comparison of rms value of the velocity fluctuation v' normalized by u'_{in} calculated with the new inflow condition.

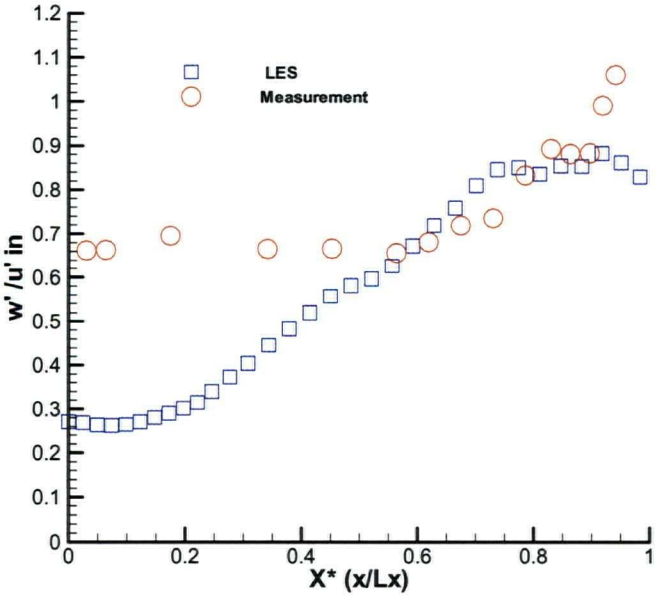

Figure 4.24 Comparison of rms value of the velocity fluctuation w' normalized by u'_{in} calculated with the new inflow condition.

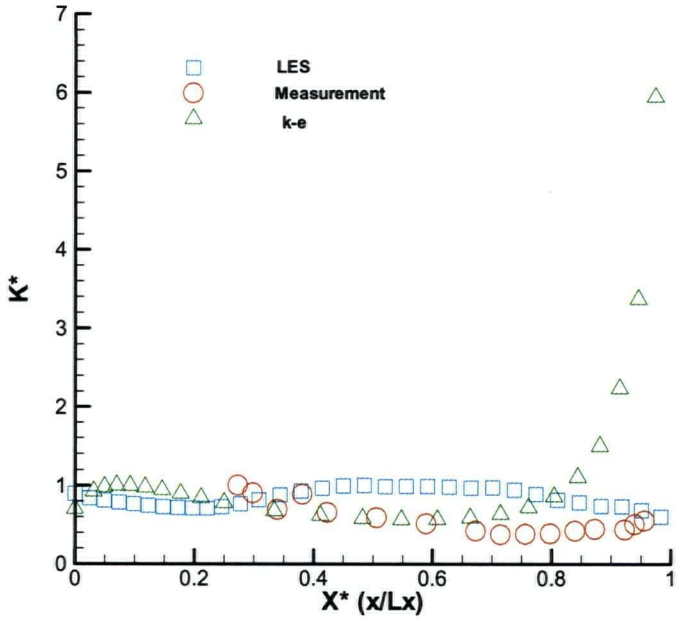

Figure 4.25 Comparison of turbulence kinetic energy k nondimensionalized by k at the inlet of the position 0.006m after the convergence starts with the new inflow condition.

4.3 Discussion

One possible reason for the apparent difference between measured and predicted results is that an effectively two-dimensional periodic condition is imposed in the spanwise direction while in the experimental apparatus there are walls on both sides of the channel. Another explanation involves the accuracy of the experimental data. In the experiment, there is the possibility of different flow rates in the adjacent rectifier tubes. From Shariati (2002), it is known that the velocity profile is different for the top and the bottom rectifier tube in the experimental measurements. This will lead to inflow conditions that are unique to the apparatus and impossible to model with precision.

In this section, the sensitivity of the simulation results with respect to grid size and the subgrid model is tested. This is necessary to assess whether the computational results represent a realistic converged solution.

4.3.1 Dependence on grid resolution

For the present configuration questions of adequate resolution and proper representation of the inflow conditions are closely related. From chapter 3 for fully developed channel flow, LES requires rather fine mesh spacing to resolve the large scales of motion. The Smagorinsky model with $64\times64\times64$ mesh can provide a good inflow condition for the converging section, but it still needs a finer mesh to resolve the core region of the channel flow. Here we use one case: $64\times64\times96$ to test the effect of grid refinement in the normal direction to the wall. It is known that 64 grids in the spanwise direction are enough to resolve the large scales for fully developed channel flow in chapter 3. The spanwise length of the converging section is the same as that of the channel flow. We can therefore expect that 64 grids in the spanwise direction will be sufficient for the converging section.

The grid parameters for different cases are shown in Table 4.2. The comparison of mean streamwise velocity along the centerline of the converging section between Case 1 and Case 2 is shown in Figure 4.26. Comparisons of resolved rms fluctuations u' and w' normalized by u' at the inlet (u'_{in}) between Case 1 and Case 2 are presented in Figures 4.27 –4.28. The meshes of Case 2 in the x direction are double those of Case 1. The results of Case 2 are almost the same as those of Case 1. A comparison of the mean streamwise velocity along the centerline of the converging section for Case 1 and Case 3 is shown in Figure 4.29. The comparisons of resolved rms fluctuations u' and w' normalized by u' at the inlet (u'_{in}) for Case 1 and Case 3 are presented in Figures 4.30–4.31. The results from a fine mesh Case 3, $64\times64\times96$ are slightly closer to the experimental data than those of the coarser mesh case but there is not a great change or improvement from a refined mesh. If a finer mesh, such as $64\times64\times128, 64\times64\times256$, would be used, the results would be expected to improve. However the computational cost would become prohibitive.

Case	*Nx*	*Ny*	*Nz*	$\Delta x/\delta$	$\Delta y/\delta$	$\Delta z_{min}/\delta$	$\Delta z_{max}/\delta$
1	64	64	64	0.03125	0.025	0.002531	0.01277
2	128	64	64	0.015625	0.025	0.002531	0.01277
3	64	64	96	0.03125	0.025	0.00166	0.008517

Table 4.2 Grid parameters. Nx, Ny, Nz denote the number of meshes in the streamwise, spanwise and wall-normal directions, respectively. δ is half of the inlet height of the converging section.

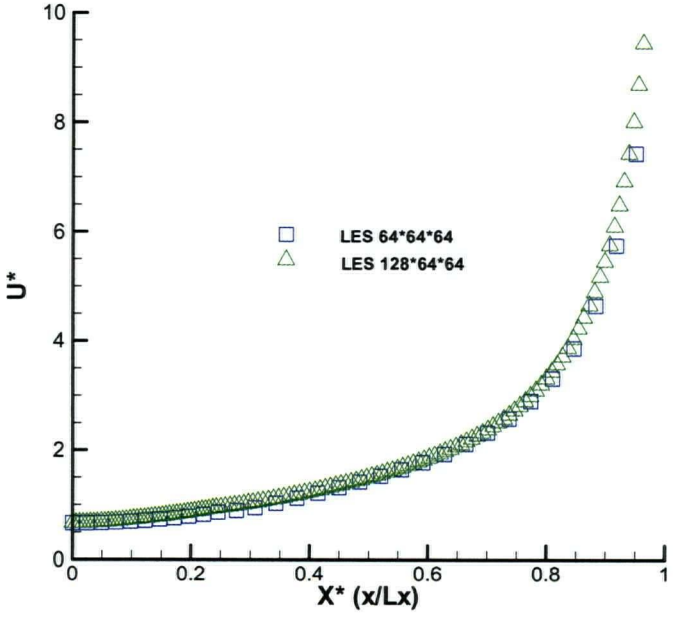

Figure 4.26 Comparison of the mean velocity at the centerline of the converging section with Case 1 and Case 2.

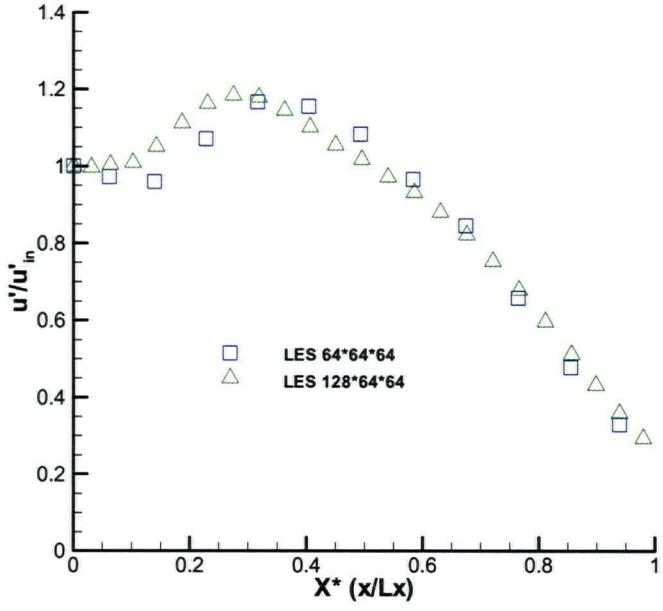

Figure 4.27 Comparison of rms value of the velocity fluctuation u' normalized by u'_{in} with Case 1 and Case 2.

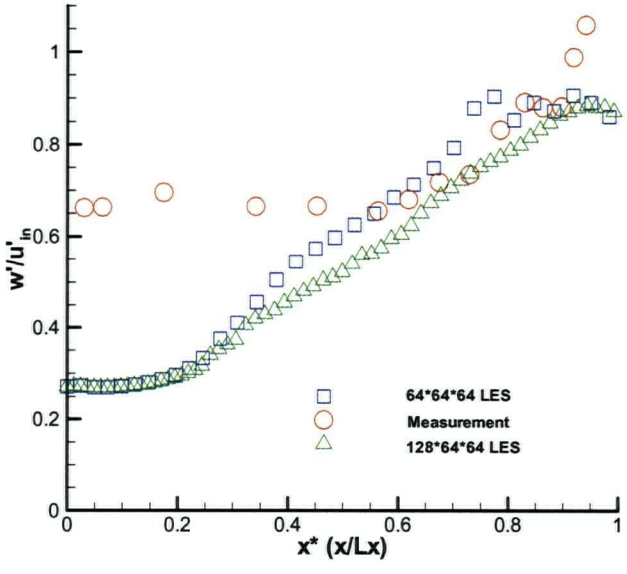

Figure 4.28 Comparison of rms value of the velocity fluctuation w' normalized by u'_{in} with Case 1 and Case 2

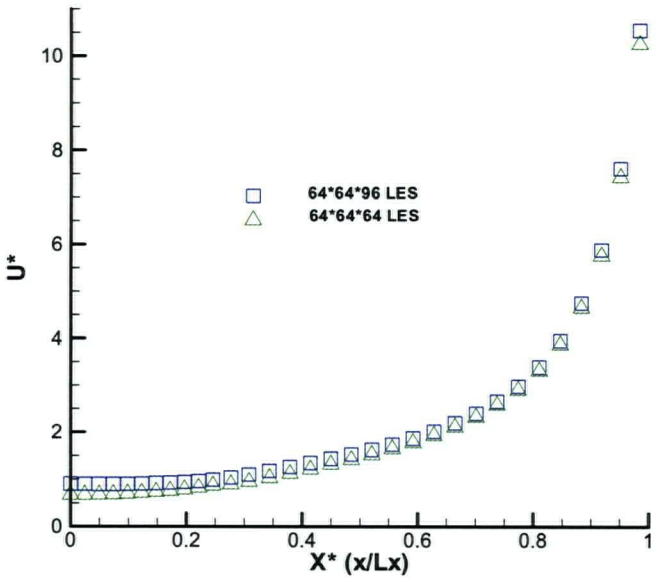

Figure 4.29 Comparison of the mean velocity at the centerline of the converging section with Case1 and Case 3.

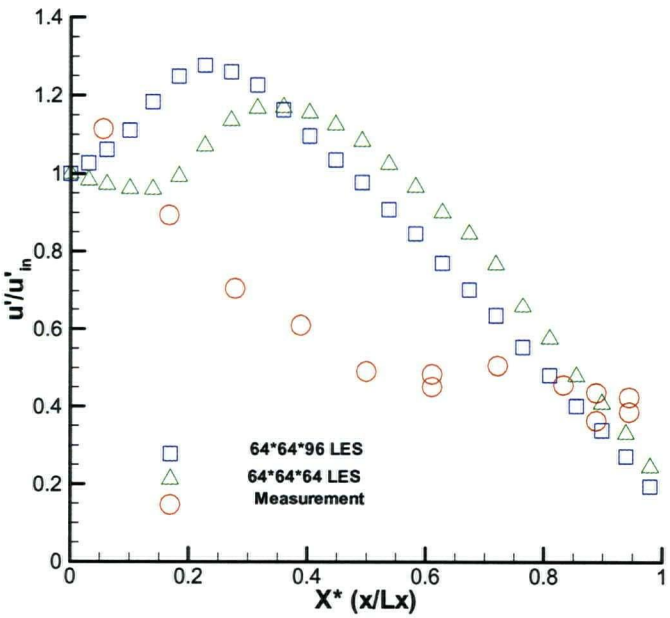

Figure 4.30 Comparison of rms value of the velocity fluctuation u' normalized by u'_{in} with Case1 and Case 3.

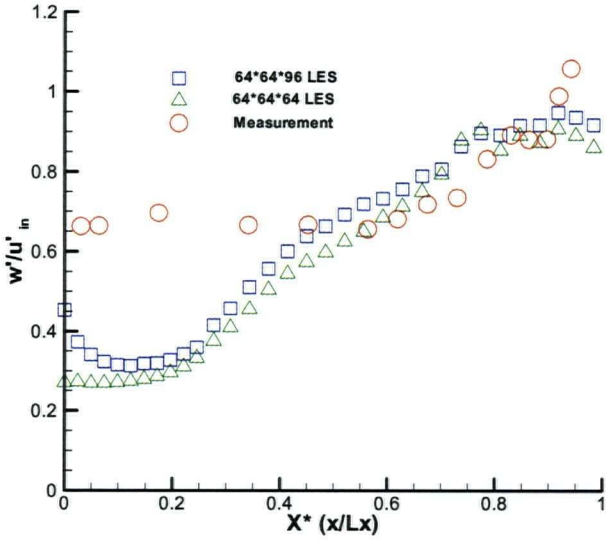

Figure 4.31 Comparison of rms value of the velocity fluctuation w' normalized by u'_{in} with Case1, and Case 3.

4.3.2 Effects of the different subgrid models

To consider the effect of the different subgrid models for the converging section, the ADM model is used with the $64\times64\times64$ mesh. The comparison of mean streamwise velocity along the centerline of the converging section among the different subgrid models is shown in Figure 4.32. The comparisons of resolved rms fluctuations u', v' and w' normalized by u' at the inlet (u'_{in}) between two different subgrid models are presented in Figures 4.33–4.35.

From the results, there is not much difference for two different subgrid models. It is noted that there is a little difference from w' in Figure 4.35. The reason is that different filter operations are used in non-uniform meshes at z direction. For the Smagorinsky model, there is an implicit filter which involes one cell. The explicit filter operation, which involes five cells in each direction, is used for the ADM model. The Smagorinsky model is therefore adequate for the converging section.

The ratio of the SGS eddy viscosity to the molecular viscosity, ν_T / ν, is shown with the Smagorinsky model along the centre of the converging section in Figure 4.36. The value is less than 6 in most of region. The maximum value reaches around 13 near the exit. This indicates that the effect of the different subgrid models is not large.

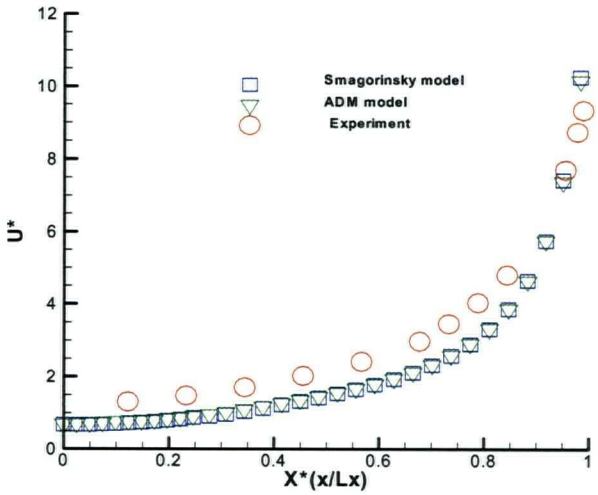

Figure 4.32 Comparison of the mean velocity at the centerline of the converging section with different subgrid models.

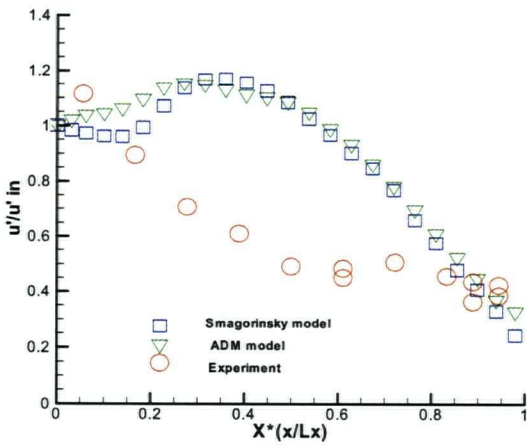

Figure 4.33 Comparison of rms value of the velocity fluctuation u' normalized by u'_{in} with different subgrid models.

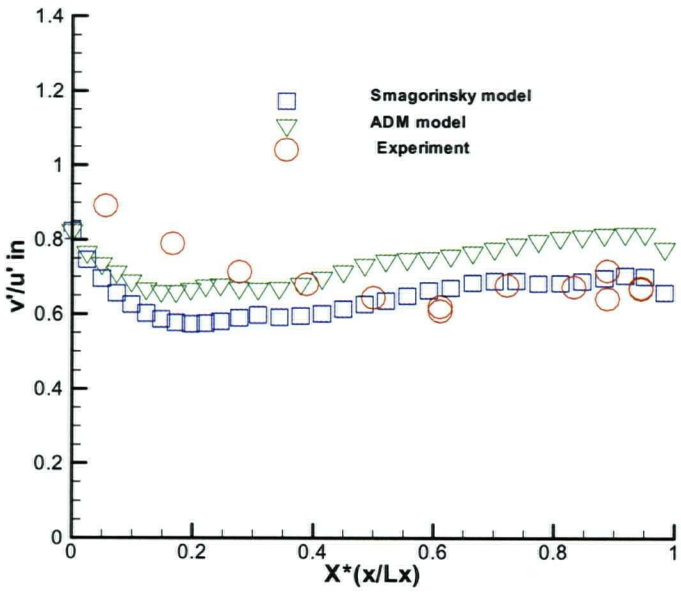

Figure 4.34 Comparison of rms value of the velocity fluctuation v' normalized by u'_{in} with different subgrid models.

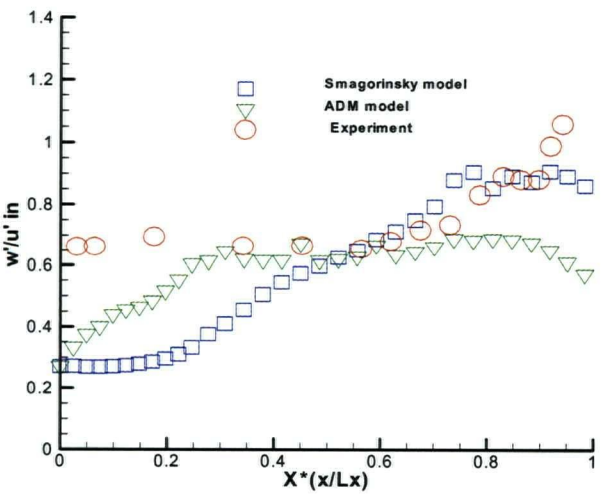

Figure 4.35 Comparison of rms value of the velocity fluctuation w' normalized by u'_{in} with different subgrid models.

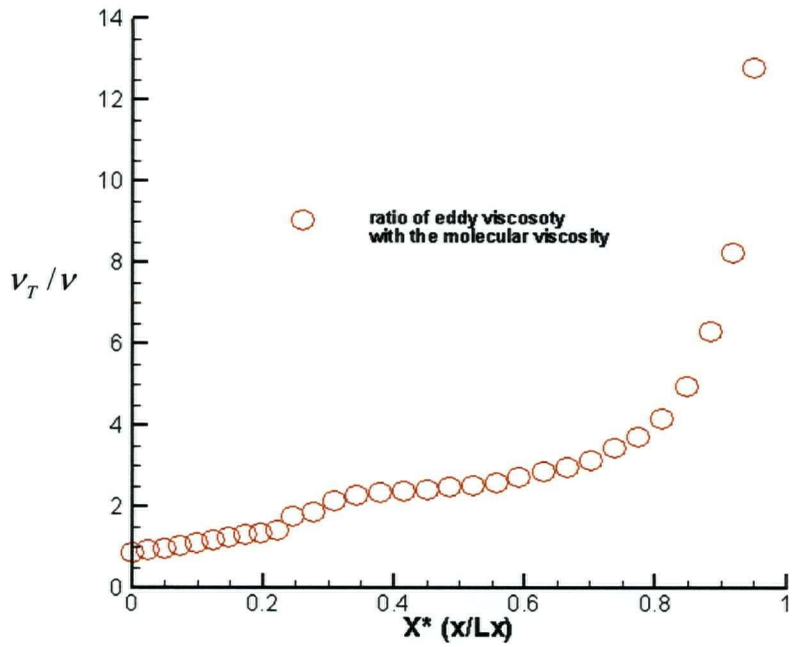

Figure 4.36 Ratio of SGS eddy viscosity to molecular viscosity: ν_T / ν with the Smagorinsky model.

4.4 Summary

The large eddy simulation method has been used to compute the turbulent flow through an asymmetric converging section. An important feature of this flow is that the turbulence is extremely non-isotropic near the exit where the standard $k-\varepsilon$ model fails to predict the correct kinetic energy.

The proper inflow condition is challenging for present quantitative predictions. The most straightforward approach to get the inflow condition for the converging section is to start the calculation by completely modelling the rectifier tubes. This procedure would be very time consuming. A one channel inflow condition is first employed to compute the turbulent flow in the converging section. This approach is also used by Kaltenbach *et al.* (1999), where a channel flow is used to generate inflow conditions for a plane diffuser. The computed values of the mean velocity agree well with the measured values. For rms fluctuations, the trend of the calculation results is similar to that of the experimental results, but there are some differences between the numerical

results and the measured results from the inlet of the converging section to the first third of the way through the converging section. The use of a "two-channel" to represent the inflow condition is also tested. The different inflow conditions can indeed affect the fluctuation results. The "two-channel" inflow condition is better than the one channel inflow condition, but one problem evident in the results using the "two-channel" inflow conditions is that the computational streamwise fluctations are only half of the measured values at 0.03m from the inlet of converging section. An alternative generation of inflow conditions method is therefore proposed. The idea is based on the extracting/rescaling technique developed by Lund *et al.* (1998). The computed streamwise fluctations and mean velocity using this new inflow data agree reasonably well with the measured values at 0.03m from the inlet of converging section. For the results along the centerline of the converging section, they are almost the same as those with one channel inflow condition. The v' with the new inflow condition is better than that with one channel inflow condition.

The grid dependence study also reveals a sensitivity to the inflow condition. The more fine mesh in the wall-normal direction can make the predicted rms values of the velocity fluctuations along the centerline of the converging section more similar to the measured values. The reason is that the value of the velocity fluctuation w' at the inlet is closer to the measured values with a fine mesh in the wall-normal direction.

The agreement of rms values of velocity fluctuations between the computational results and the measured values is less satisfactory. The remaining disagreement is likely to be partly related to the coarse meshes in the wall-normal direction. As indicated by our grid dependence study, a finer mesh would probably improve the numerical results somewhat. Another possible reason for the apparent difference between measured and predicted results is that we use an effectively two-dimensional periodic condition in the spanwise direction while in the experimental apparatus there are walls on both sides of the channel. Another explanation involves the accuracy of the experimental data. In the experiment, there is the possibility of different flow rates in the adjacent

rectifier tubes. From Shariati (2002), we know that the velocity profile is different for the top and the bottom rectifier tube in the experimental measurements. This will lead to inflow conditions that are unique to the apparatus and impossible to model with precision.

The numerical code has been used to simulate the turbulence through a converging section. The objective 3, described in chapter 1, is achieved.

Chapter 5 Fiber Concentration and Orientation

5.1 Introduction

The numerical flow simulations have been performed with LES as described in chapters 3 and 4 for fully developed channel flow and turbulent flow through a converging section. In this chapter, a fiber model is coupled with LES to study the fiber concentration in turbulent channel flow and fiber orientation in a headbox.

Screening is an important process in both chemical and mechanical pulping (Kumar 1991, Olson 1996, Gooding 1986, 1996, Gooding *et al.* 2001, Dong 2002). Understanding the fiber motion and fiber concentration in the flow approaching the screen plate is a key part of predicting the screen fractionation efficiency. In section 5.2, numerical results are given to simulate numerically the fiber concentration in a 3D turbulent channel flow that is similar in many ways to the flow upstream of the screen.

Fiber orientation in the paper determines the quality of the paper and the study of fiber orientation in the paper machine headbox becomes more and more important. Zhang (2001) measured the fiber orientations along the centerline of an asymmetric headbox. He also predicted the fiber orientation in both symmetric and asymmetric headboxes using a fiber model, but only using the mean flow field obtained from the $\kappa-\varepsilon$ model. His comparison between the experiment and predicted results showed that the simulated orientations tend to align more with the flow than the experimentally observed orientations because the turbulence was not taken into consideration in his calculation. Dong *et al.* (2002) partially considered the turbulence effect with a single fixed velocity field found through LES simulation. In section 5.3, the fiber calculation executes one step after which the flow is updated with LES. This means the flow distribution for fibers is changed at each

time step to consider more realistic turbulence effects in the simulation. The summary is given in section 5.4.

5.2 Fiber concentration

Olson (1996) experimentally determined the detailed distribution of fiber concentration for a range of fiber lengths. The channel velocity in the experiment is 7.1 m/s and the channel Reynolds number is about 71,000 based on the channel half-height and bulk velocity. Dyed nylon fibers of length 0.0031m, 0.0020m and 0.0011m with diameter 40 microns were used. The fiber concentration was less than 5000 fibers/litre so that the fiber-fiber interaction was negligible.

Since the fiber suspension is dilute, the fiber-fiber interaction and the effects of the fiber on the turbulent flow are neglected in the present simulation. If a particle with density ρ_p and radius a moves in a fluid with dynamic viscosity μ and friction velocity u_τ, the Stokes number (Crowe *et al.* 1985) can be defined as $St = \frac{\tau_p}{\tau_f}$ which is essentially the ratio of the particle response time $\tau_p = \frac{2\rho_p a^2}{9\mu}$ and some fluid time scale $\tau_f = \frac{\delta}{u_\tau}$ (Rouson and Eaton, 1994, δ is the channel half-height). If the Stokes number is very small, then the particle follows the flow exactly. If it is very large, the particle will not be affected by turbulent fluctuations. If the Stokes number is in the order of one, the particle will be affected by the turbulence and will not follow the mean flow exactly (Fessler, *et al.*, 1994). In the current simulation, if a is taken as the typical long radius of the spheroid used to represent the fiber, the Stokes number St is about 1.9. So the fiber is then expected to be affected by the turbulence and may not exactly follow the mean flow.

5.2.1 Fiber model and wall model

The first investigation of the motion of a rigid, neutrally buoyant, ellipsoidal particle in a Stokes flow was conducted by Jeffery (1922). The Jeffery theory could be used to describe the

motion of rigid fibers (Anczurowski and Mason 1967). Pulp fibers have high aspect ratios and can have considerable flexibility which could not be modelled well by Jeffery's theory (Mason 1954). A flexible fiber model based on Euler-Bernoulli beam bending theory was introduced in Lawryshyn (1996). The immersed boundary method was used in Stockie and Green (1998) to simulate the motion of flexible pulp fibers. Their work was restricted to two-dimensional simulations. A flexible fiber model was proposed by Ross and Klingenberg (1997). It was further developed by Dong (2002) to account for fiber-wall interaction. In this model, each fiber consists of N rigid spheroids connected through $N-1$ joints (see Figure 5.1). The lengths a, $b(b \leq a)$ are the major and minor axes of each spheroid. The fiber can bend and twist much like a real fiber because of the rotational freedom in each joint. The motion of the fiber is determined by solving each spheroid's translation and rotation equations which are derived from Newton's second Law and the law of moment of momentum.

Fibers frequently touch the wall in pulp and paper equipment, so that a wall model that can efficiently deal with the fiber-wall interaction is needed. For a smooth wall, a two-dimensional wall model was developed in Olson (1996). The idea is that a reaction force normal to the wall is exerted on the fiber to stop the fiber passing through the solid wall, and the friction force tangential to the wall is proportional to the normal force on the fiber. Dong (2002) extended the Olson's model to a three-dimensional universal wall model, which can deal with the fiber interaction in any wall geometry. We will use the fiber model and the wall model developed by Dong (2002) in the following simulations.

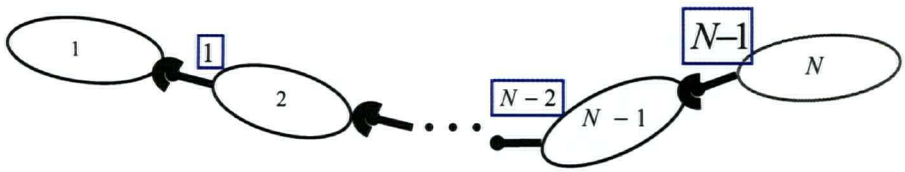

Figure 5.1 A fiber consisting of spheroids connected through ball and socket joints (from Ross and Klingenberg (1997)).

5.2.2 Numerical results

The schema of the channel flow is shown in Figure 5.2. The height of the channel is 0.02m (z direction), which is the about the same as that of Olson (1996). The numerical methods have been described in chapter 3. The comparison between numerical and experimental results for channel flow can be found in Dong, *et al.* (2003).

In order to record the fiber positions, several stations are set along the channel length. The channel height is divided into equal height intervals. The concentration ratio C / Cav is calculated by the ratio of the number of fibers at each height interval at each station to the average number of the fibers across the channel height. 8000 rigid fibers of 0.001m, 0.002m, 0.003m are initially chosen across the channel with random height and random orientations such that the number of fibers is about the same at each height interval.

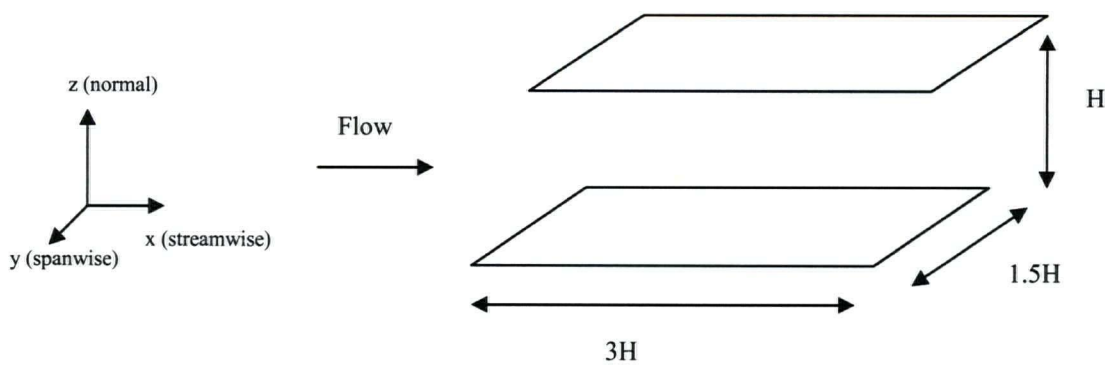

Figure 5.2 Schema of the channel flow

After the flow field from LES is statistically steady, the fibers are put in. Then each LES time step calculation is followed by one step of the fiber motion. Figure 5.3 shows the comparison of concentration for 0.001m, 0.002m, 0.003m fibers. We can see that the concentration curve of 0.002m and 0.003m fibers are very close to the Olson's fitted curve. Olson's fitted concentration curve (Olson 1996) is

$$C/C_{avg} = \begin{cases} 3.22\, z/L, & z/L < 1/3.22, \\ 1, & z/L \geq 1/3.22. \end{cases} \tag{5.1}$$

where L is the fiber length, z is the fiber center position in normal wall direction.

The 0.001m fiber does not have the same curve. The grid size in x direction (0.0006m) is probably too coarse for 0.001m fiber simulation.

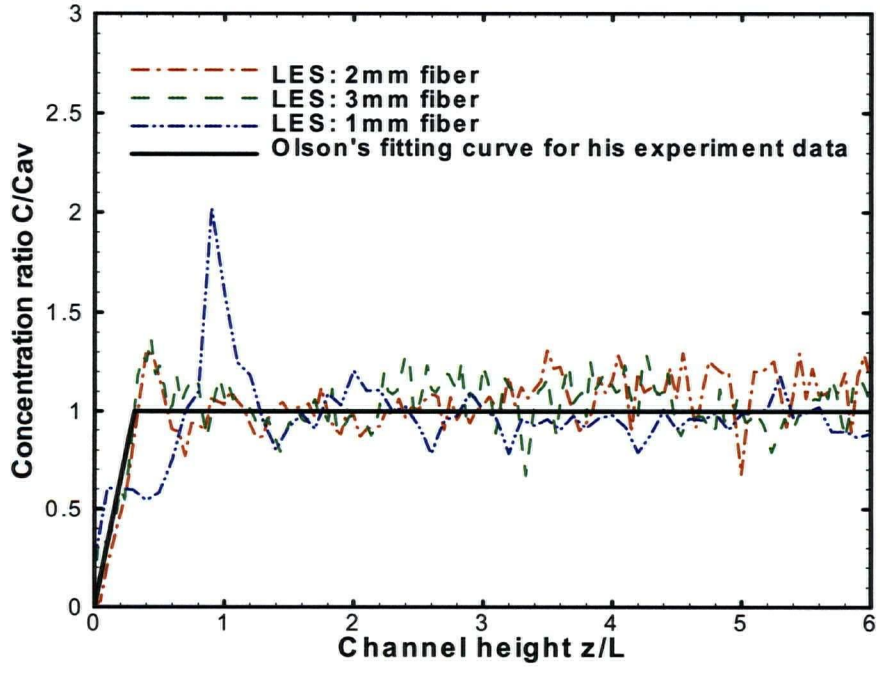

Figuer 5.3 Concentration for 0.001m, 0.002m, 0.003m fiber vs. channel height scaled by fiber length with LES

5.3 Fiber orientation in the headbox

In addition to LDV measurements, fiber experiments had been conducted by Zhang (2001) who measured the orientation of dyed nylon fibers moving in the Shariati's headbox (Shariati 2002). The fibers are made of nylon and have a nominal length of 0.003m and the diameter of 44 μm. The suspension is well within the dilute regime, with the consistency of no more than 0.001%, which means there is little interaction between fibers. In the experiment, video pictures were taken of fibers in motion at several locations along the center of the converging section.

5.3.1 Initial conditions

The fiber's position can be defined by three variables: fiber center (x_c, y_c, z_c), polar angle $0 \le \theta \le \pi$, which is the angle between the fiber main axis and Z-axis, and the azimuthal angle $0 \le \phi \le \pi$, which is the angle between the Y-axis and the projection of the fiber main axis on XY plane (see Figure 5.4). It is noted that one end of the fiber is not distinguishable from the other.

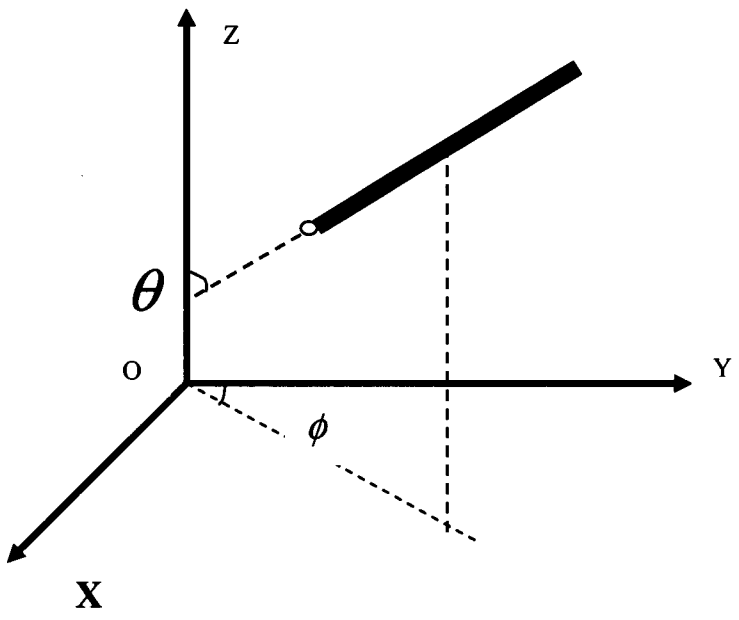

Figure 5.4 A fiber's initial position.

Eight thousand (8,000) rigid fibers of 0.003m length are initially chosen across $0.04\ m$ region ($0.0175\ m \le z \le 0.0575\ m$) in the center of the inlet height with random height and random orientation. Random orientation is implemented by choosing the fiber angles θ and ϕ with random number generators. The angles θ and ϕ are not chosen randomly from uniform distributions $\theta \in [0,\pi]$ and $\phi \in [0,\pi]$, since the area element $d\Omega = \sin\theta d\phi d\theta$ is a function of θ on the surface of a unit sphere. So the angles are selected with the following formula (Zhang 2001):

$$\theta = \cos^{-1}(2a_1 - 1) \tag{5.2}$$

$$\phi = \pi a_2 \tag{5.3}$$

where a_1 and a_2 are random variables between $[0,1]$.

5.3.2 Numerical results

The projections of the orientation of fibers can be obtained in three different planes. The fiber orientation was only measured in both the plane of the paper (x-y) and in the plane of contraction (x-z) at the central streamline of the converging section along the axis of the headbox in Zhang (2001). The measurements were taken at several points along the headbox as shown in Figure 5.5. So the projections on two of the planes, x-y and x-z planes, are considered here. The fiber orientation angle α ($-\frac{\pi}{2} \le \alpha \le \frac{\pi}{2}$), either on the x-y or on the x-z projection plane, is defined to be the angle between the projection of the fiber axis on that plane and the machine direction (x axis). Figure 5.6 shows the initial fiber orientation distributions in the computation. The horizontal axis represents the orientation angle α. The vertical axis stands for the statistical probability density $p(\alpha)$, such that:

$$\int_{-\frac{\pi}{2}}^{\frac{\pi}{2}} p(\alpha)d\alpha = 1 \tag{5.4}$$

If the fiber orientations are uniform, then $p(\alpha) = 1/\pi(\approx 0.318)$. It can be seen that the initial random fiber orientation distribution is almost uniform from Figure 5.6. Figures 5.7-5.13 show the fiber orientation distributions at different stations. Most of the alignment occurs near the end of converging section, beyond $x = 0.227m$, where the velocity gradient is the highest. The LES results predict the fiber orientation reasonably well when compared to the experimental data from Zhang (2001). From Figures 5.10-5.12, the $k-\varepsilon$ simulated fiber orientations tend to align more with the flow compared to experimental and LES results. At the exit where $x = 0.31m$, both $k-\varepsilon$ and LES predict that the fibers are highly aligned in the flow direction in $x-z$ plane as shown in Figure 5.13. But the peak value of LES is lower than that of $k-\varepsilon$. Unfortunately there is no experimental data of fiber orientation at the exit in the $x-z$ plane, because the channel is too narrow and the flow speed is too high at that location to get clear fiber images (Zhang 2001). From Figure 5.13, the fiber alignments in the $x-z$ plane are stronger than that in the $x-y$ plane. This phenomenon agrees with the observation in Zhang (2001) and Olson (2002). The statistical probability density $p(\alpha)$ gives little information except for the trend of the fiber alignments in the flow direction.

The first moment ($\sum_i \alpha_i p(\alpha_i)\Delta\alpha_i$), second moment ($\sum_i \alpha_i^2 p(\alpha_i)\Delta\alpha_i$) and third moment ($\sum_i \alpha_i^3 p(\alpha_i)\Delta\alpha_i$) of the probability distribution from numerical results and experimental measurements are shown in Table 5.1 and Table 5.2. The LES results are somewhat closer to the experimental data than $k-\varepsilon$ results in the $x-z$ plane from Table 5.1.

The first moment ($\sum_i \alpha_i p(\alpha_i)\Delta\alpha_i$) at different stations in the $x-z$ plane and the $x-y$ plane are presented in Figures 5.14-5.15. The first moment indicates the mean angle value of the probability density $p(\alpha)$. The LES results of the first moment are closer to the experimental data

than the $k-\varepsilon$ results near the exit in Figure 5.14. The first moment values from $k-\varepsilon$ simulations in the $x-y$ plane are better than those from LES simulations in Figure 5.15.

The second moment ($\sum_i \alpha_i^2 p(\alpha_i)\Delta\alpha_i$) at different stations in the $x-z$ plane and the $x-y$ plane are shown in Figures 5.16-5.17. The second moment values from LES simulations are closer to the experimental data than $k-\varepsilon$ simulations in the $x-z$ plane and the $x-y$ plane from Figures 5.16-5.17. The second moment indicates that the fiber is whether alignment in the flow direction or not. This is important for the design of a headbox. The second moment is decreasing along the converging section from station 0.192m to the exit. The fiber is close to random at the entrance and that gives a large value of the second moment. As the fiber gets closer to the exit it gets aligned with the flow. Turbulence is counteracting this alignment. The fiber angle is affected by the strain rate in the flow. The normal strain rate $\frac{\partial u}{\partial x}$ is large near the exit of the converging section. It is not surprising that the fibers tend to align themselves in the flow direction. There are only mean quantities in the $k-\varepsilon$ simulations. The mean strain rate $\frac{\partial U}{\partial x}$ dominates in the flow along the center of the converging section near the exit. For LES simulations, the flow contains two parts: the mean part and the resolved fluctuation part. The fluctuation velocity gradient $\frac{\partial w'}{\partial x}$ is large as seen in Figure 4.24 from chapter 4. The shear strain rate $\frac{\partial w}{\partial x}+\frac{\partial u}{\partial z}$ is not a negligible value. This shear strain rate reduces the effect of the normal strain rate $\frac{\partial u}{\partial x}$. That works against aligning the fibers in the flow direction. The turbulence tends to randomize the fiber orientation. So the LES simulations give the better comparison with experimental data for the second moment than the $k-\varepsilon$ simulations.

The third moment ($\sum_i \alpha_i^3 p(\alpha_i)\Delta\alpha_i$) at different stations in the $x-z$ plane and the $x-y$ plane are presented in Figures 5.18-5.19. The third moment value indicates the skewness of the probability density $p(\alpha)$. If the third moment is large, the $p(\alpha)$ is very asymmetric. The third moment has small variation along the length of the converging section. There is some asymmetry but not very significant. The geometry and the flow are not completely symmetric. From Figures 5.18 and 5.19, the third moments from LES are close to experiment data at some stations. But there are some differences between LES results and experimental data at some stations. One obvious difference occurs at 0.262m station. One possible reason is that the fiber number is not large enough in the LES simulations near the exit.

It is difficult to compare the results accurately. One reason is that the number of fibers used in the experiments and computations is not large enough. The initial $8,000$ fibers are put into more than half channel height. The actual fibers at the center of converging section are less than 500. Much more computational time is needed with more fibers. From Zhang (2001), the experimental fiber number is less than 1500 at some stations. Another very likely reason is the lack of accuracy of flow measurement data as mentioned earlier in chapter 4. The problems in the experimental measurements discussed in chapter 4 have an influence on the fiber calculations as well. The changes in alignment near the exit are very abrupt. Accurate measurements near the exit of the converging section are difficult to make and the precise location is hard to define.

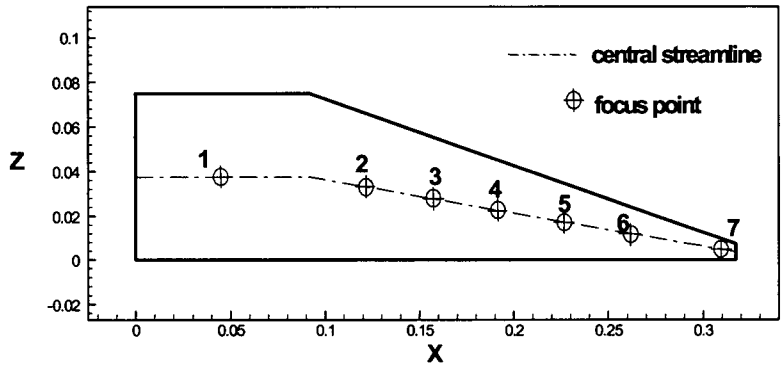

Figure 5.5 Measurement points along the headbox, unit m.

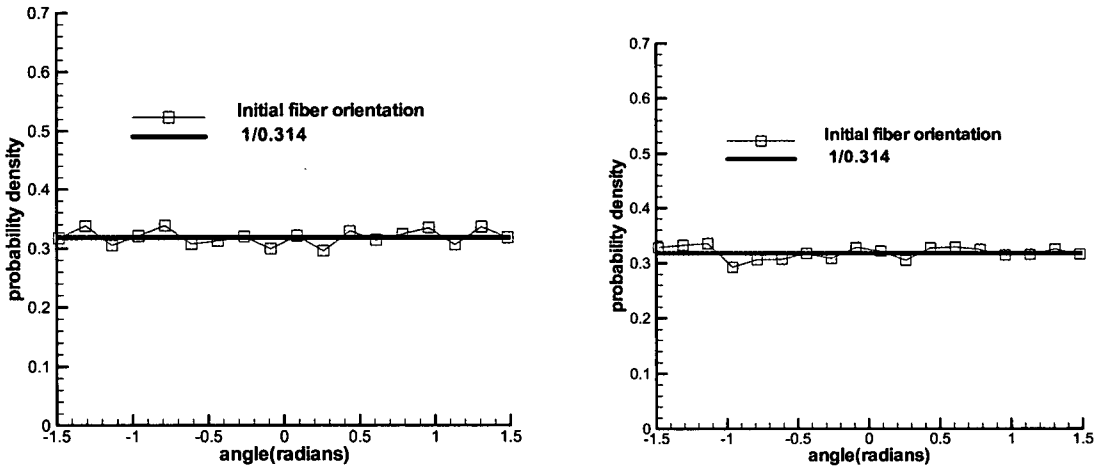

(a) (b)

Figure 5.6 Initial fiber orientation distribution, (a) in x-z plane, (b) in x-y plane

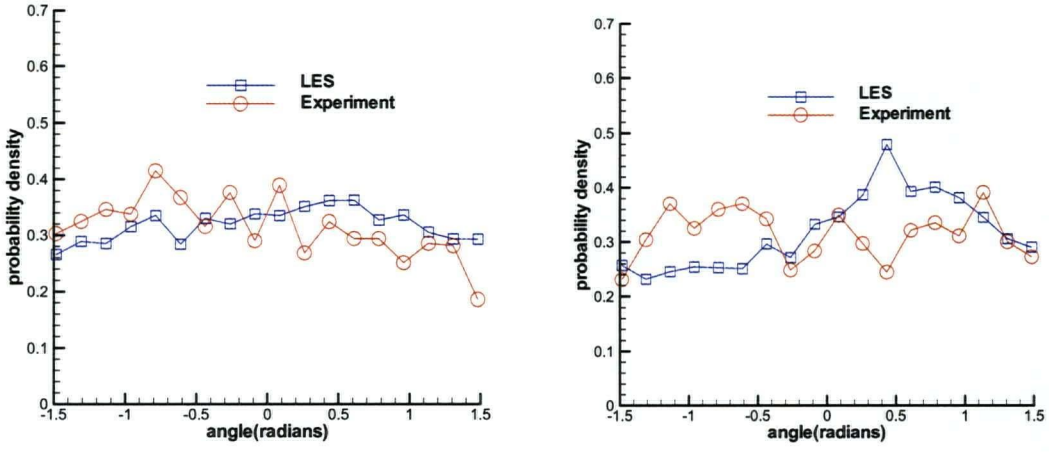

(a) (b)

Figure 5.7 Fiber orientation distribution at x = 0.045m, (a) in x-z plane, (b) in x-y plane

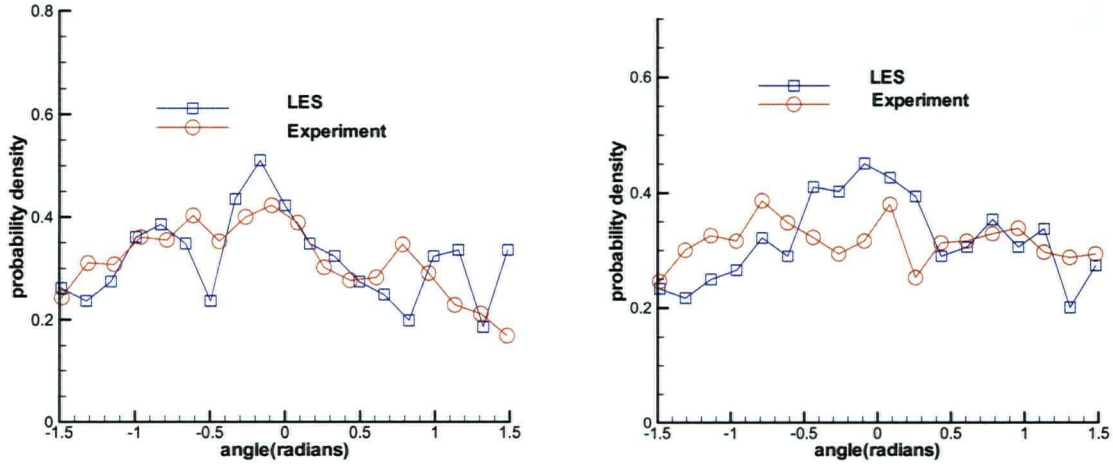

(a) (b)

Figure 5.8 Fiber orientation distribution at x = 0.122m, (a) in x-z plane, (b) in x-y plane

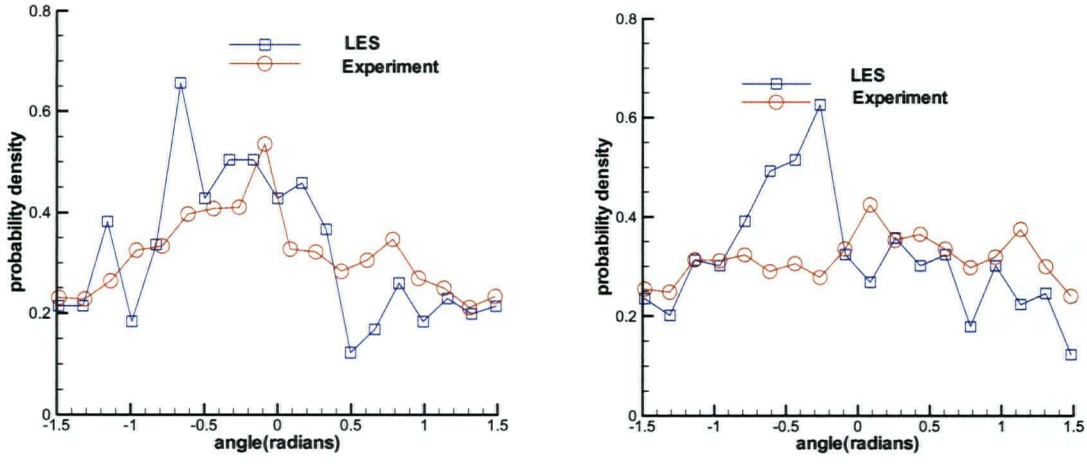

(a) (b)

Figure 5.9 Fiber orientation distribution at x = 0.157m, (a) in x-z plane, (b) in x-y plane

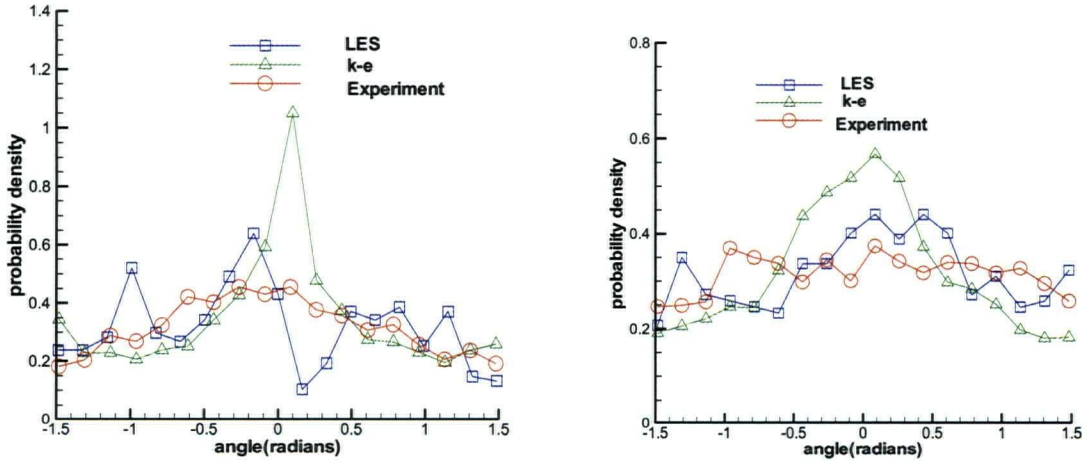

(a) (b)

Figure 5.10 Fiber orientation distribution at x = 0.192m, (a) in x-z plane, (b) in x-y plane

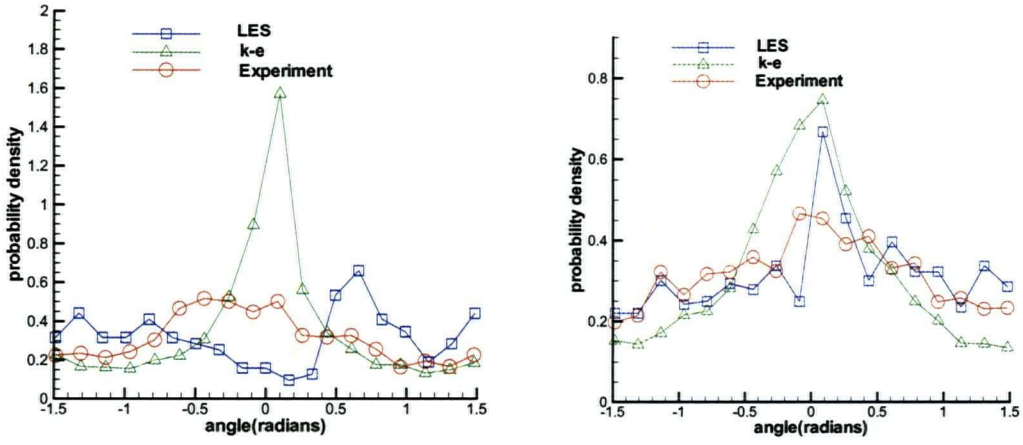

(a) (b)

Figure 5.11 Fiber orientation distribution at x = 0.227m, (a) in x-z plane, (b) in x-y plane

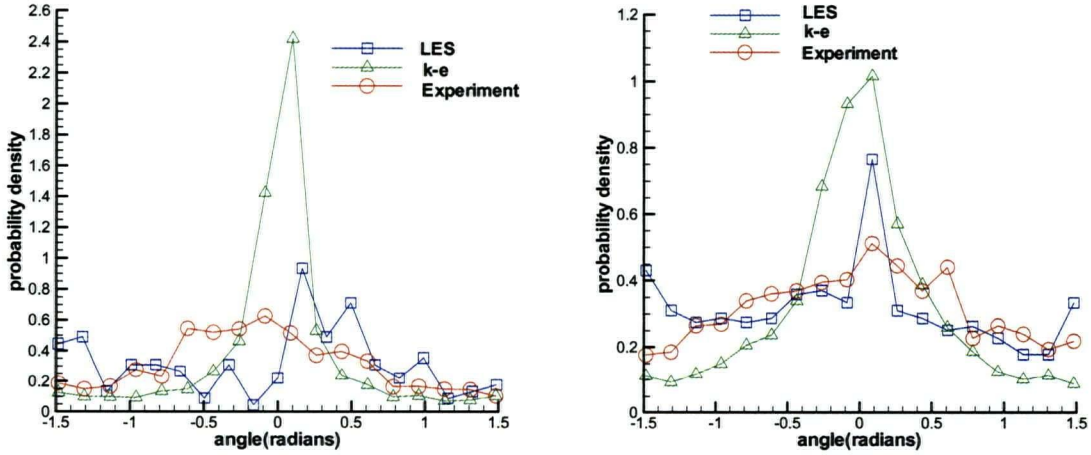

(a) (b)

Figure 5.12 Fiber orientation distribution at x = 0.262m, (a) in x-z plane, (b) in x-y plane

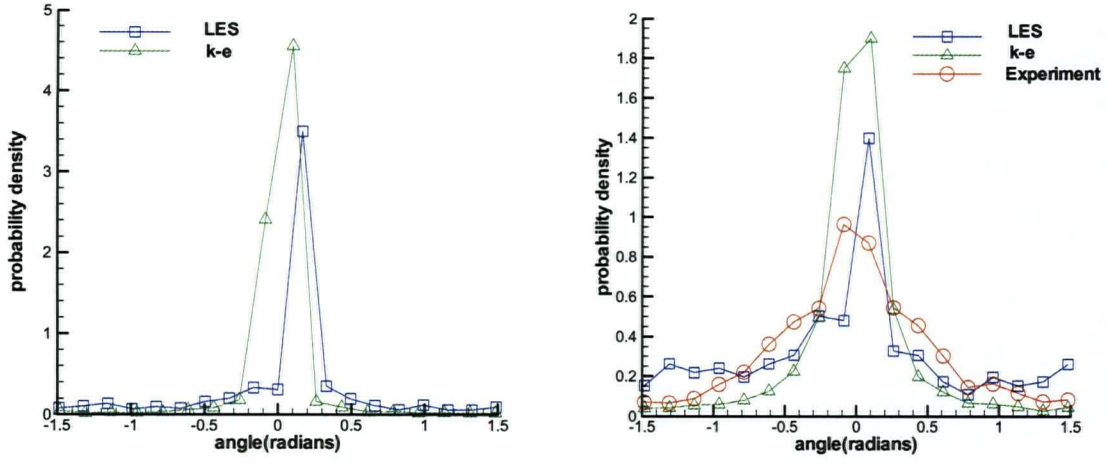

(a) (b)

Figure 5.13 Fiber orientation distribution at the converging section exit,
(a) in x-z plane, (b) in x-y plane

	First moment (experiment)	Second moment (experiment)	Third moment (experiment)	First moment (LES)	Second moment (LES)	Third moment (LES)	First moment ($k-\varepsilon$)	Second moment ($k-\varepsilon$)	Third moment ($k-\varepsilon$)
0.045m	-0.093	0.753	-0.125	0.027	0.769	0.029			
0.122m	-0.094	0.689	-0.118	-0.032	0.775	0.009			
0.157m	-0.039	0.670	-0.021	-0.050	0.675	-0.052			
0.192m	-0.025	0.623	-0.008	-0.067	0.652	-0.088	-0.001	0.663	-0.043
0.227m	-0.074	0.594	-0.053	-0.028	0.611	-0.002	0.001	0.481	-0.035
0.262m	-0.094	0.482	-0.085	-0.070	0.584	-0.205	0.006	0.295	-0.026
exit				0.090	0.262	-0.016	0.033	0.082	-0.013

Table 5.1 The first moment ($\sum_i \alpha_i p(\alpha_i)\Delta\alpha_i$), second moment ($\sum_i \alpha_i^2 p(\alpha_i)\Delta\alpha_i$) and third moment ($\sum_i \alpha_i^3 p(\alpha_i)\Delta\alpha_i$) of the probability distribution in x-z plane.

	First moment (experiment)	Second moment (experiment)	Third moment (experiment)	First moment (LES)	Second moment (LES)	Third moment (LES)	First moment ($k-\varepsilon$)	Second moment ($k-\varepsilon$)	Third moment ($k-\varepsilon$)
0.045m	-0.001	0.794	0.020	0.052	0.753	0.045			
0.122m	-0.005	0.776	0.012	0.027	0.689	0.046			
0.157m	0.032	0.737	0.029	-0.025	0.695	-0.027			
0.192m	0.020	0.745	0.034	0.045	0.727	0.042	-0.011	0.571	-0.017
0.227m	0.001	0.659	0.012	0.026	0.710	0.038	-0.008	0.468	-0.014
0.262m	0.004	0.611	0.013	-0.020	0.574	-0.108	-0.008	0.350	-0.012
exit	-0.007	0.325	0.001	-0.027	0.538	-0.006	0.002	0.161	-0.004

Table 5.2 The first moment ($\sum_i \alpha_i p(\alpha_i)\Delta\alpha_i$), second moment ($\sum_i \alpha_i^2 p(\alpha_i)\Delta\alpha_i$) and third moment ($\sum_i \alpha_i^3 p(\alpha_i)\Delta\alpha_i$) of the probability distribution in x-y plane.

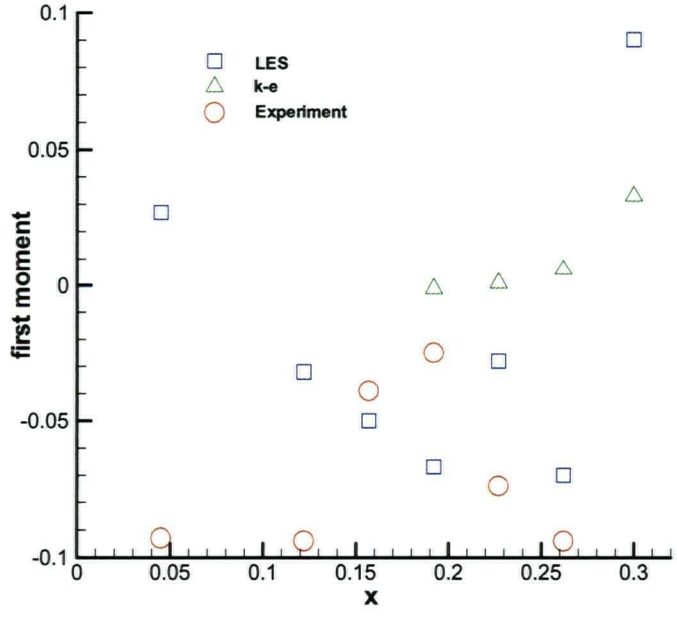

Figure 5.14 The first moment ($\sum_i \alpha_i p(\alpha_i)\Delta\alpha_i$) at different stations in x-z plane.

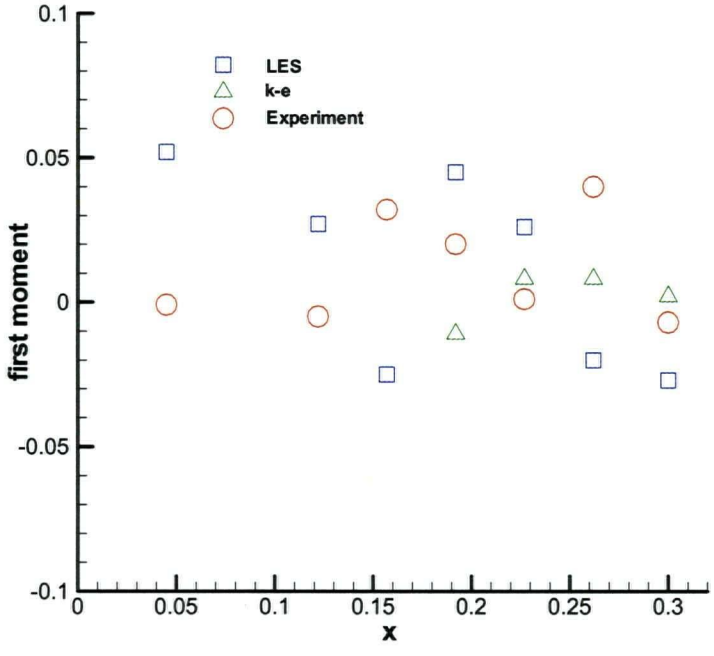

Figure 5.15 The first moment ($\sum_i \alpha_i p(\alpha_i)\Delta\alpha_i$) at different stations in x-y plane.

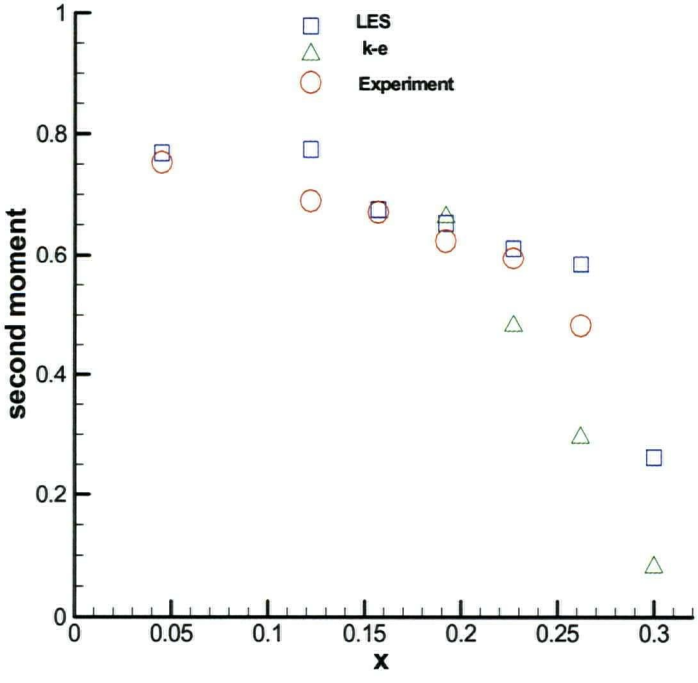

Figure 5.16 The second moment ($\sum_i \alpha_i^2 p(\alpha_i)\Delta\alpha_i$) at different stations in x-z plane.

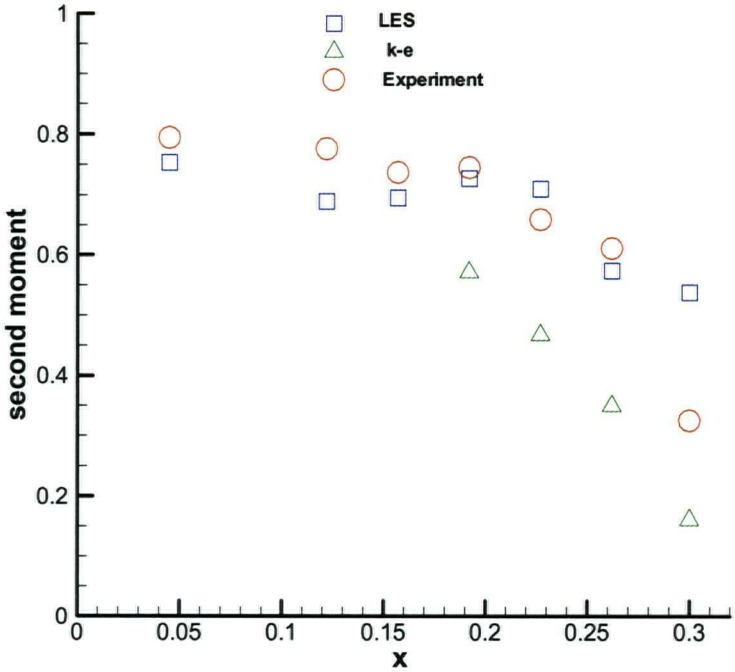

Figure 5.17 The second moment ($\sum_i \alpha_i^2 p(\alpha_i)\Delta\alpha_i$) at different stations in x-y plane.

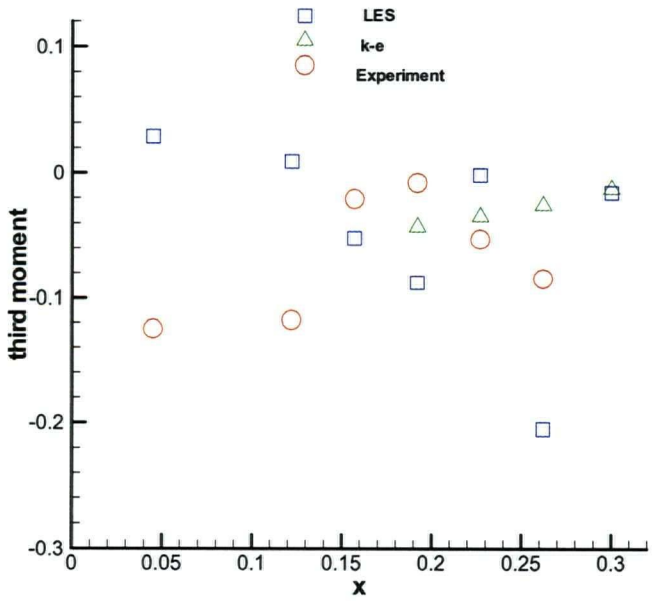

Figure 5.18 The third moment ($\sum_i \alpha_i^3 p(\alpha_i)\Delta\alpha_i$) at different stations in x-z plane.

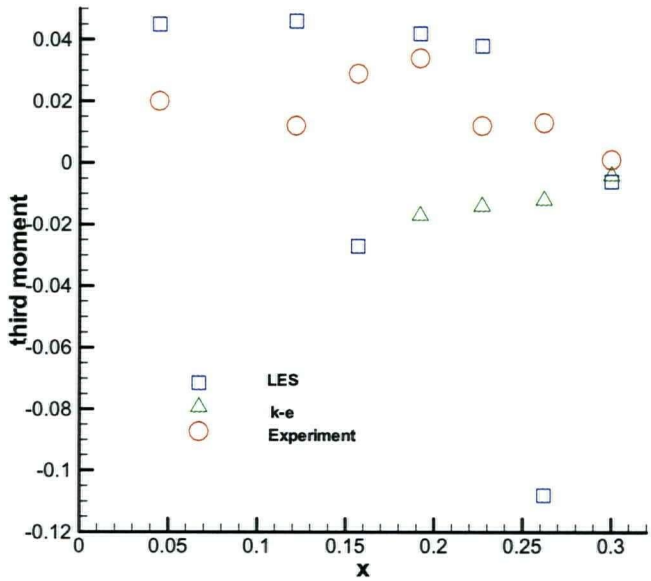

Figure 5.19 The third moment ($\sum_i \alpha_i^3 p(\alpha_i)\Delta\alpha_i$) at different stations in x-y plane.

5.3.3 Discussion

In the above calculations, 8,000 fibers are used for the fiber orientation distribution calculation. In order to verify that 8000 fibers represent the fibers with sufficient accuracy, the use of 16,000 and 24,000 fibers are also tested. Figure 5.20 shows a comparison of fiber orientation distribution at x = 0.157m in x-y plane with 8000, 16,000 and 24,000 fibers where the error bars stand for the standard deviation from the mean of these three sets of data. The result shows that the three sets of data produce no significant difference in the x-y plane. Consequently 8,000 fibers are used for the calculation.

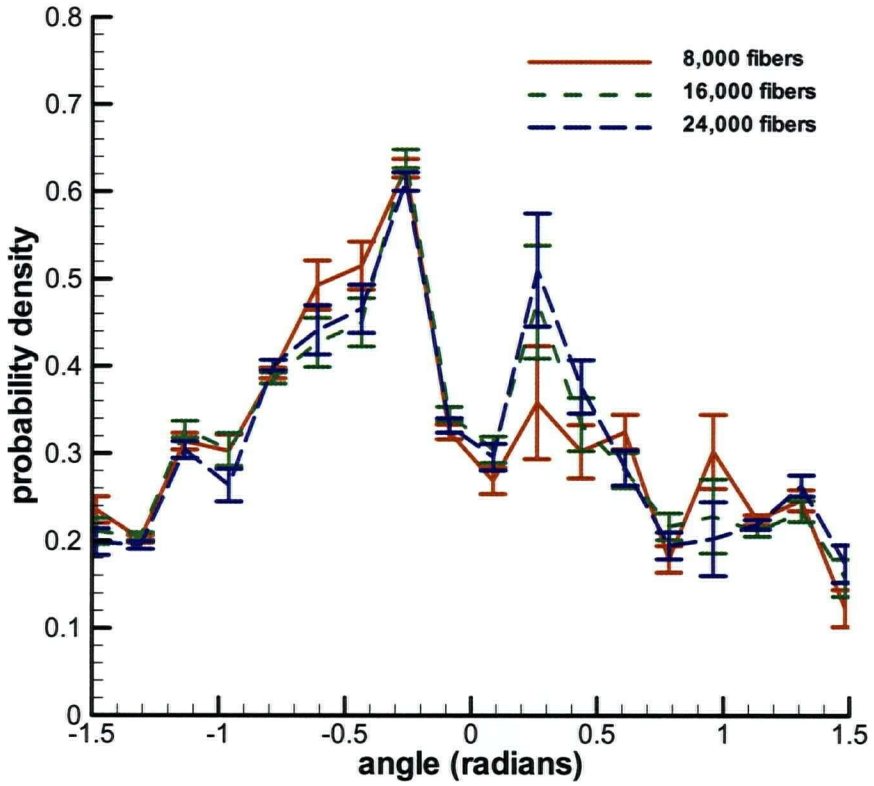

Figure 5.20 Fiber orientation distribution at x = 0.157m in x-y plane with 8000, 16,000 and 24,000 fibers

5.4 Summary

Using the LES method with different length fibers, the concentration curves of the 0.002m and 0.003m fibers are similar to the experiments of Olson (1996).

The LES and a fiber motion model have been coupled for predicting the orientation of rigid fibers in dilute suspensions. The effects of turbulence that would tend to randomize the fibers are included in these simulations of fiber motion. Random initial fiber orientations are set at the inlet of the channel. The statistical expressions of the orientation of a large number of fibers are evaluated at each station by computing the orientation of each single fiber along the central streamline. The LES results predict the fiber orientation reasonably well when compared to the experimental data. The

predicted orientation distributions with LES are better than the $k-\varepsilon$ simulated fiber orientations near the exit of the converging section. The numerical results show that the LES calculation scheme can provide a useful method for the simulation of the interaction between fibers and complex fluid flow patterns.

The LES code is coupled with a suitable fiber model to study the statistical orientation of nylon "fibers" in the converging section. The objective 4, described in chapter 1, is achieved.

Chapter 6 Simulation of a Typical Industrial Headbox

6.1 Introduction

A numerical tool to simulate turbulence in a headbox has been developed in chapter 3, where its use for simulating the flow through the converging section of a laboratory headbox has been described. However, the Reynolds number for the laboratory headbox is much lower than that for an industrial headbox, and it is therefore still challenging to simulate the turbulence in a typical industrial case. As far as the LES method used for the present simulations is concerned, the higher Reynolds number should be an advantage, because the spectral separation between inertial and dissipative scales, being greater in the high Reynolds number case, allows for very clear and distinct simulation of the larger scales.

In this chapter, the flow through the converging section of a typical generic headbox is simulated with LES. Two inflow conditions are investigated in section 6.2. Some observations are presented in section 6.3.

6.2 Flow simulation

6.2.1 Computational geometry

The geometry of the converging section is shown in Figure 6.1. The length of the converging section in the streamwise or x direction is $0.665\ m$. The inlet height of the converging section is $0.105\ m$. The contraction ratio is 7. The actual length in the cross-stream or y direction is $8.64\ m$. In the numerical simulation presented here, the dimension in the y direction is set to $0.1575\ m$ because periodic boundary conditions are used in the y direction, assuming that the flow

is essentially two-dimensional.

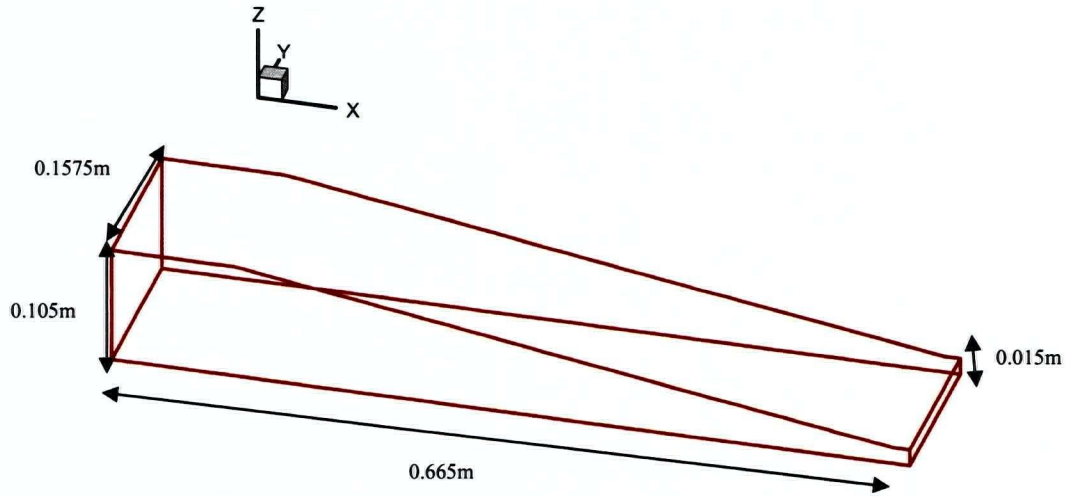

Figure 6.1 The geometry of the converging section.

6.2.2 Inflow conditions

In the z direction, which is normal to the walls at entry, no-slip wall boundary conditions are imposed along the solid walls. As noted above, the spanwise direction, y, is treated as periodic. At the exit plane, the convective boundary condition (Kaltenbach 1998, Kaltenbach et al.1999) is imposed.

At the inlet plane, two inflow conditions are tested. One is to use the unsteady distribution for the velocity components generated by a separate LES of fully developed channel flow (Figure 6.2). The other is a "five-channel" inflow condition, simulating the flow from the outlets of a series of five equal smaller channels, typical of the turbulence generators often used in commercial headboxes. The inflow condition is linearly interpolated from five small height channels (Figure

6.3). Each channel is then 0.019 m high and each wall separating the five channels is 0.0025 m thick, the total of the five channels and four intervening walls making up the 0.105 m inlet height of the headbox. The wall thickness is explicitly considered in the generation of the inflow condition. The mean velocity profiles at the inlet for the one channel inflow and "five-channel" are shown in Figure 6.4. Z^* is the z position from the bottom plane normalized with the total height at the same location. The corresponding resolved rms fluctuations u', v' and w' at the inlet are presented in Figures 6.5-6.7. From these graphs, some zero values for the "five-channel" inflow condition can be seen due to the wall thickness.

The volume flow rate is $0.208\ \mathrm{m}^3/s$ (per unit width) which is close to the maximum volume flow rate expected for a commercial headbox. The same mass flow rate is imposed for the two inflow conditions. As already noted, the wall thickness between small channels for the "five-channel" inflow condition is 0.0025 m and each small channel height is $0.019\ m$.

The numerical method is the same as that of chapter 4. The ADM model and the constant Smagorinsky model are used to consider the effect of subgrid scales. All the calculations are performed with parallel computation, as described in chapter 3, on the P4-Xeon Cluster with a Myrinet network at the University of British Columbia.

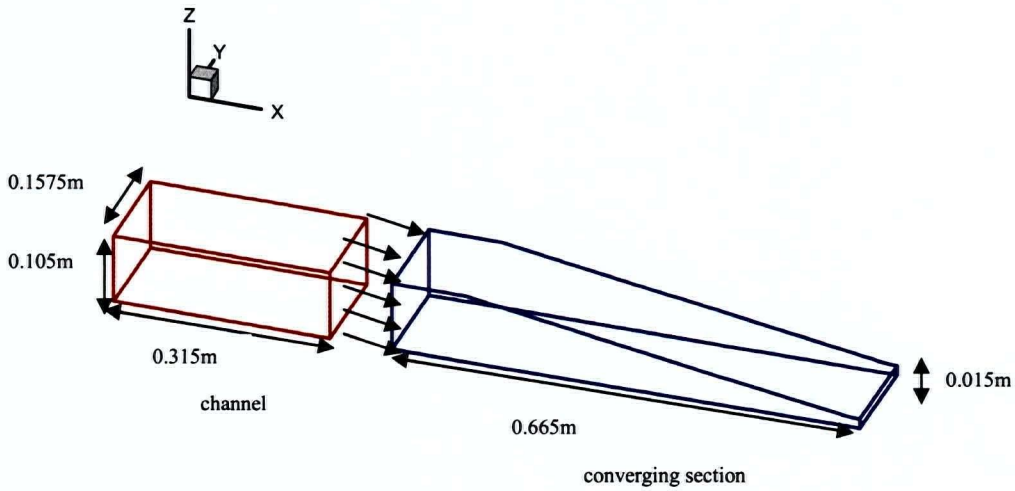

Figure 6.2 One-channel inflow condition for the converging section.

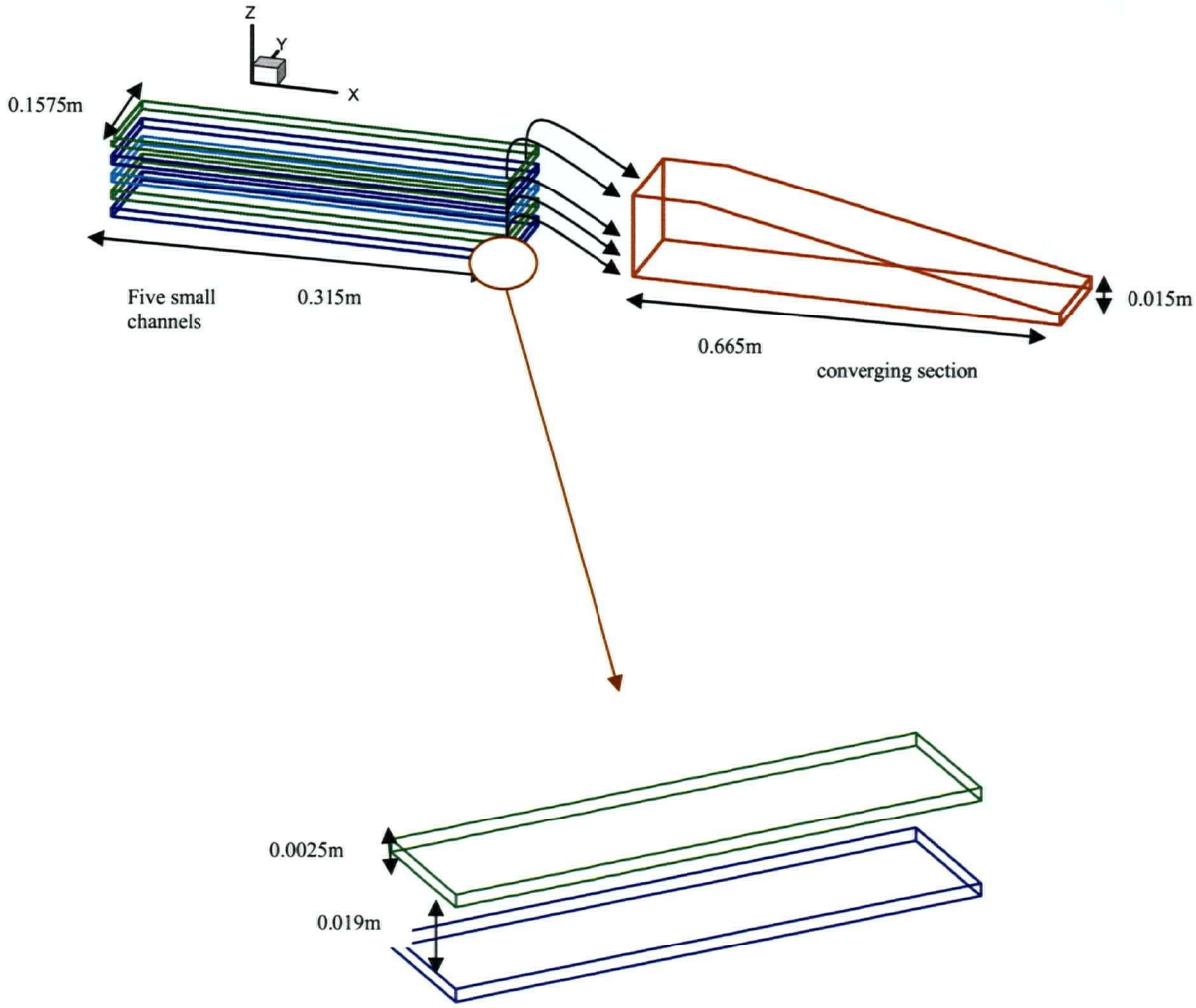

Figure 6.3 Schematic diagram of the "five-channel" inflow condition showing the details of one of the five identical channels

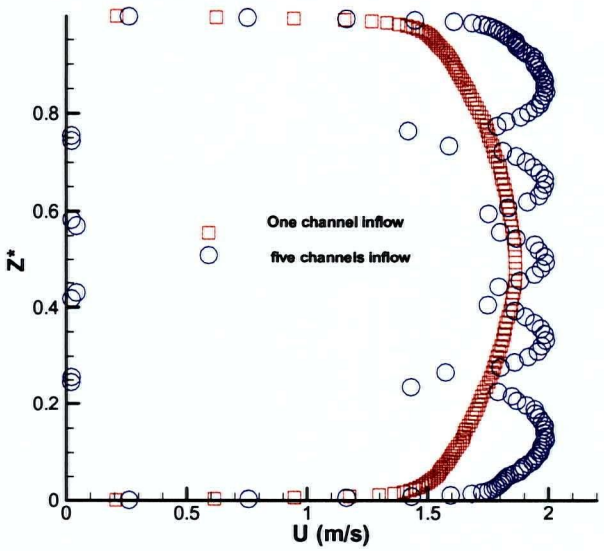

Figure 6.4 Comparison of the mean velocity at the inlet.

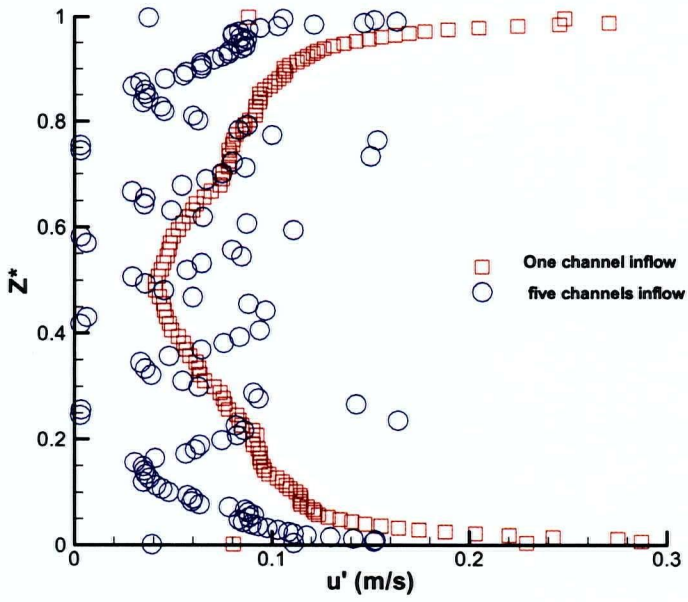

Figure 6.5 Comparison of rms value of the velocity fluctuation u' at the inlet.

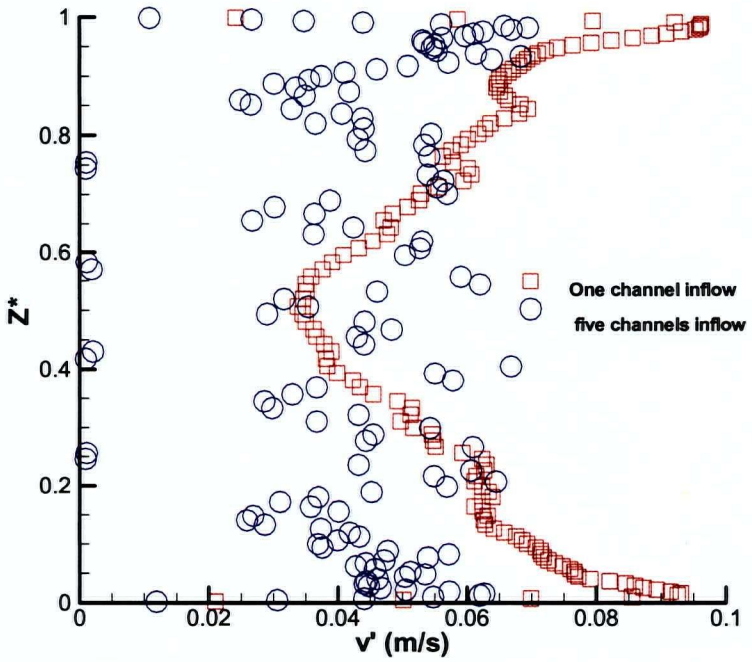

Figure 6.6 Comparison of rms value of the velocity fluctuation v' at the inlet.

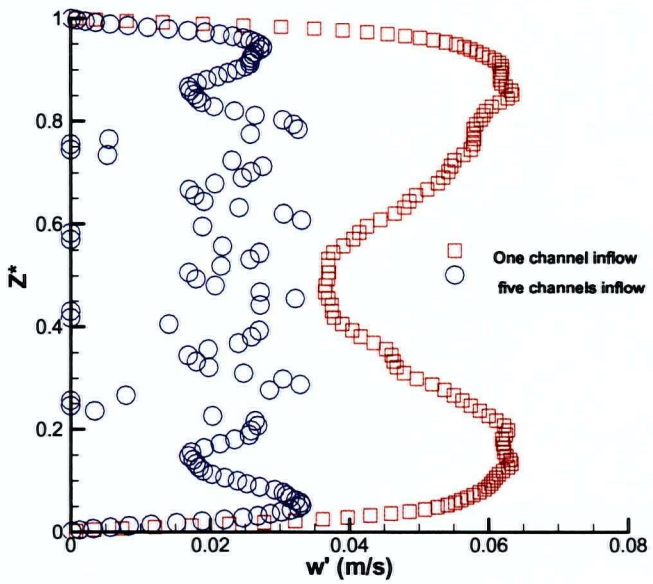

Figure 6.7 Comparison of rms value of the velocity fluctuation w' at the inlet.

6.2.3 Numerical results

The flow characteristics are taken at several positions along the converging section. The first position is located at one sixth of the full length where the converging section starts (AB line in Figure 6.8). The second position is at one third of the whole length (CD line in Figure 6.8). The third position is at two thirds of the whole length (EF line in Figure 6.8). The last position is at the outlet.

The $96\times96\times128$ mesh is used. The meshes are uniform in the streamwise direction x and the spanwise direction y. A non-uniform grid is employed in the normal wall direction z to resolve the near wall region as described in chapter 3.

The mean streamwise velocity profiles computed from two inflow conditions are shown in Figure 6.9 at the first station AB with the ADM model. They are very similar even at this first station. The resolved rms fluctuations u', v' and w' are presented in Figures 6.10-6.12 at the first station AB with the ADM model. From Figures 6.5-6.7, the fluctuations from the two inflow conditions have a significant difference at the inlet. The differences from two inflow conditions are reduced a great deal at the first station from Figures 6.10-6.12. The fluctuations from "five-channel" inflow conditions grow more quickly, presumably due to the energy produced by the more non-uniform inlet mean velocity profile that is present in the "five-channel" case.

The mean streamwise velocity profiles from the two inflow conditions are shown in Figure 6.13 at the second station CD derived from use of the ADM model. Not surprisingly, there is little difference between these two distributions. The resolved rms fluctuations u', v' and w' are presented in Figures 6.14-6.16 at the second station CD with the ADM model. The fluctuations from "five-channel" inflow conditions are slightly greater than those from the one channel inflow conditions at this second station, showing that more turbulence is generated at one third of the whole length from the "five-channel" inflow conditions.

The mean streamwise velocity profiles from the two inflow conditions are presented in Figure 6.17 at the third station EF. The resolved rms fluctuations u', v' and w' are shown in Figures 6.18-6.20 at the third station EF. The trend is the same as that at the second station.

The mean streamwise velocity profiles from the two inflow conditions are shown in Figure 6.21 at the outlet. Essentially identical mean velocity profiles are obtained at the outlet from the two different inflow conditions. The resolved rms fluctuations u', v' and w' are presented in Figure 6.22-6.24 at the outlet. The fluctuations u' from the two inflow conditions show little difference here. However, the fluctuations v' and w' from the "five-channel" inflow conditions are greater than that from one channel inflow conditions at the outlet, implying that more turbulence is indeed generated using the "five-channel" inflow conditions, and that this increased turbulence lasts to the outlet of the headbox.

As an alternative to the results produced by the ADM model, some simulations are repeated with the Smagorinsky model simulating the small scales of turbulence. The mean streamwise velocity profiles from the two inflow conditions are shown in Figure 6.25 at the outlet with the constant Smagorinsky model. The mean velocity profile is not symmetric near the upper wall region. This can be a result of the inflow condition that was interpolated from the asymmetrical channel flow. The resolved rms fluctuations u', v' and w' at the outlet are presented in Figures 6.26-6.28. The fluctuations u' from the two inflow conditions have little difference at the outlet. However, as before at the outlet, the fluctuations v' and w' from "five-channel" inflow conditions are greater than that from the one channel inflow conditions, showing that essentially similar results are obtained when using either model of small-scale turbulence.

The ratios of resolved rms fluctuations v'/u' and w'/u' are presented in Figures 6.29-6.30 at different positions with the ADM model. From these graphs, the turbulence is close to isotropic at the first and second stations in most regions. The anisotropy of the turbulence grows at the third

position. At the outlet, the turbulence is very anisotropic in most regions. The maximum value of v'/u' can be up to 3.5 at the outlet of the converging section.

Figures 6.31-6.32 show the ratio of v'/u' and w'/u' at the outlet with the two inflow conditions. There is little difference in these plots for the two inflow conditions.

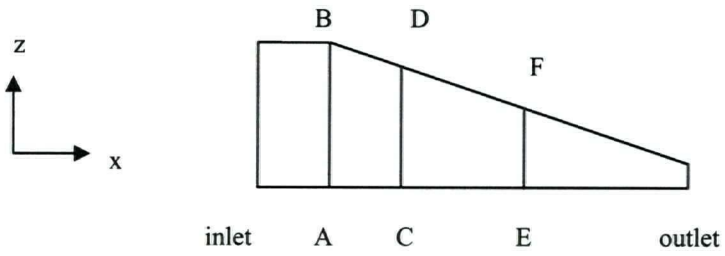

Figure 6.8 Comparison positions along the headbox.

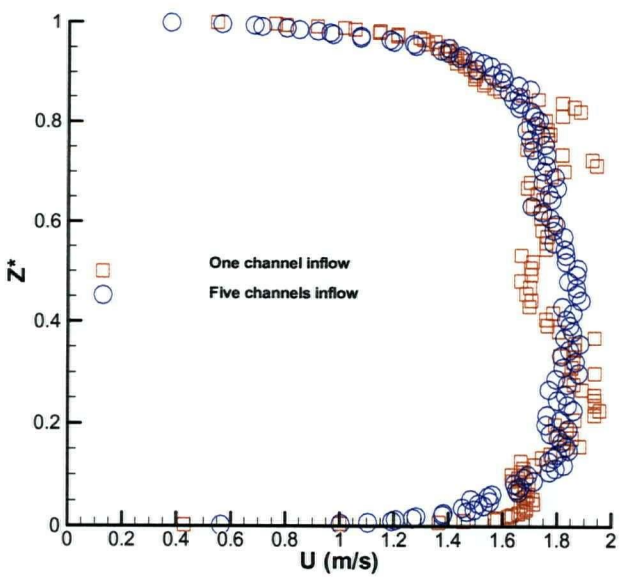

Figure 6.9 Comparison of the mean velocity at the first station AB.

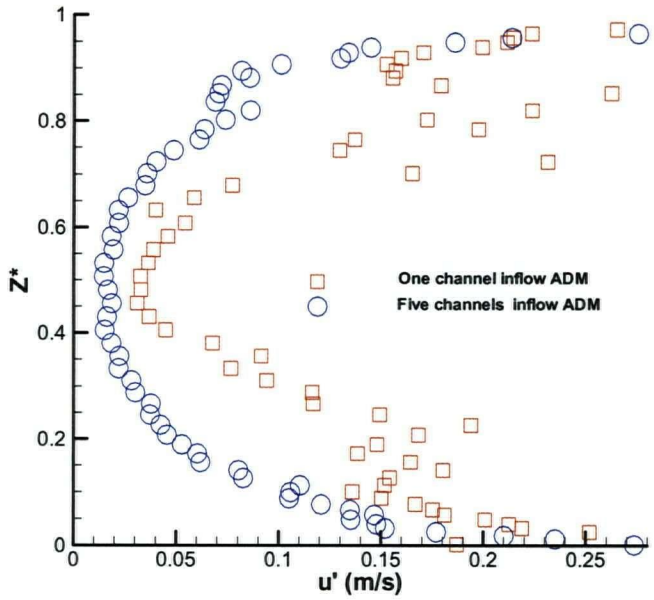

Figure 6.10 Comparison of rms value of the velocity fluctuation u' at the first station AB.

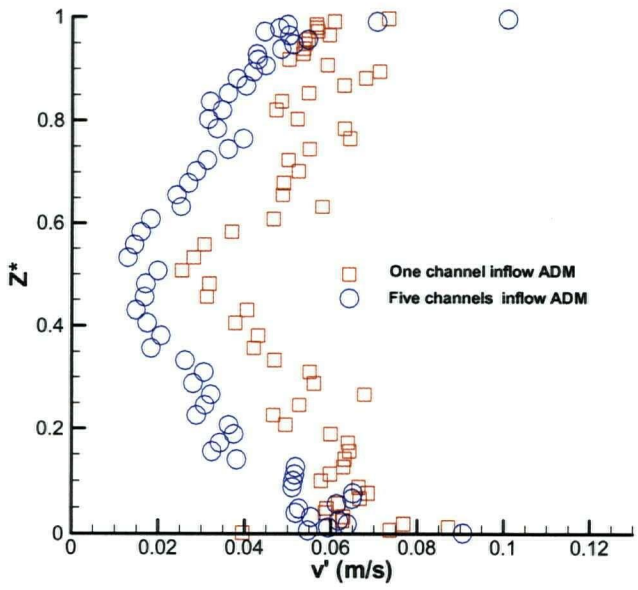

Figure 6.11 Comparison of rms value of the velocity fluctuation v' at the first station AB.

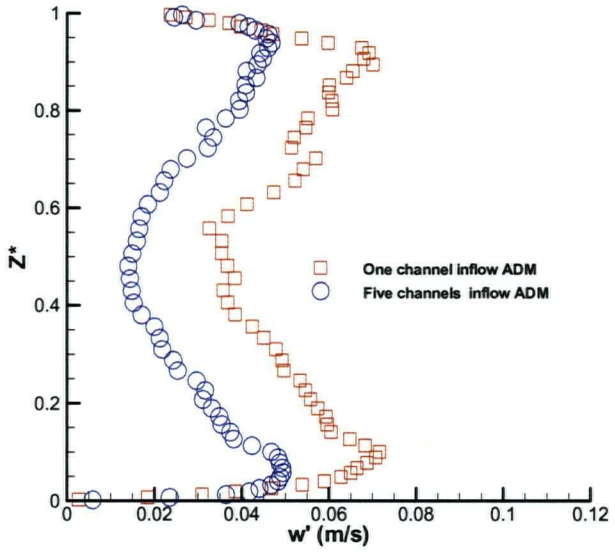

Figure 6.12 Comparison of rms value of the velocity fluctuation w' at the first station AB.

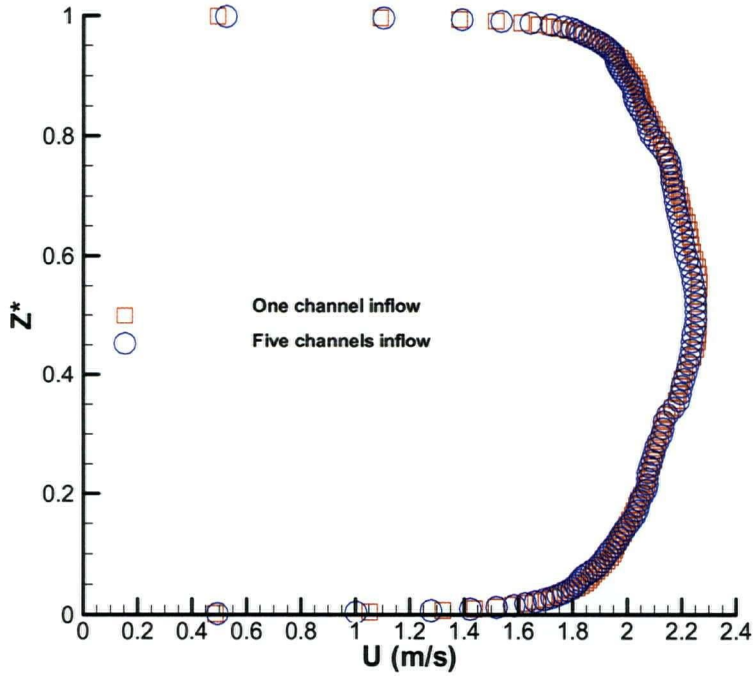

Figure 6.13 Comparison of the mean velocity profiles at the second station CD.

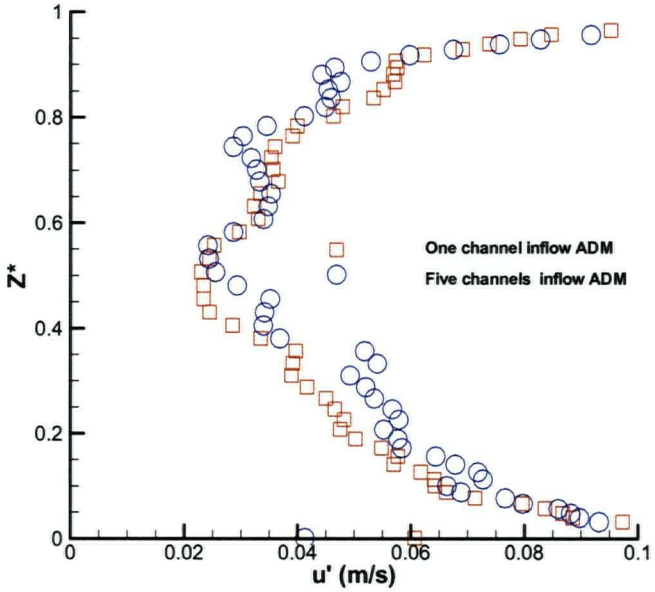

Figure 6.14 Comparison of rms value of the velocity fluctuation u' at the second station CD.

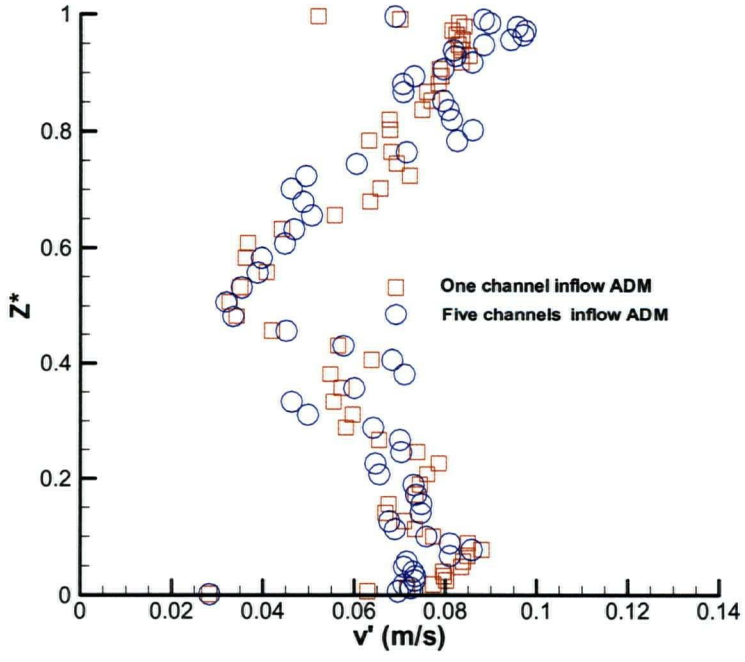

Figure 6.15 Comparison of rms value of the velocity fluctuation v' at the second station CD.

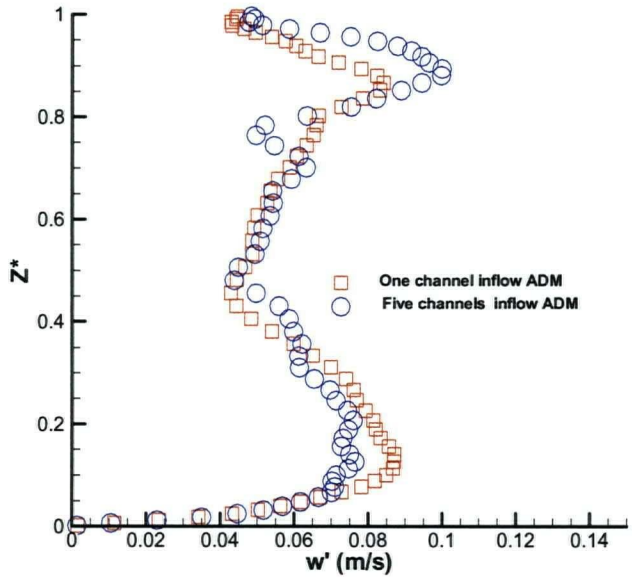

Figure 6.16 Comparison of rms value of the velocity fluctuation w' at the second station CD.

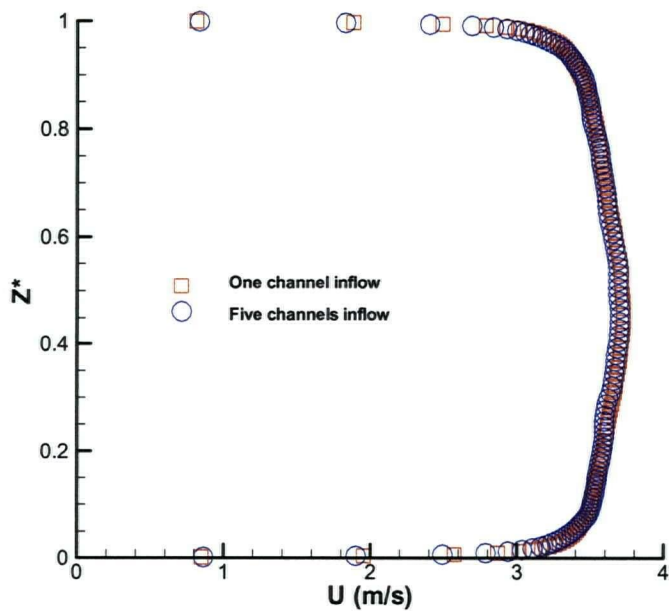

Figure 6.17 Comparison of the mean velocity at the third station EF.

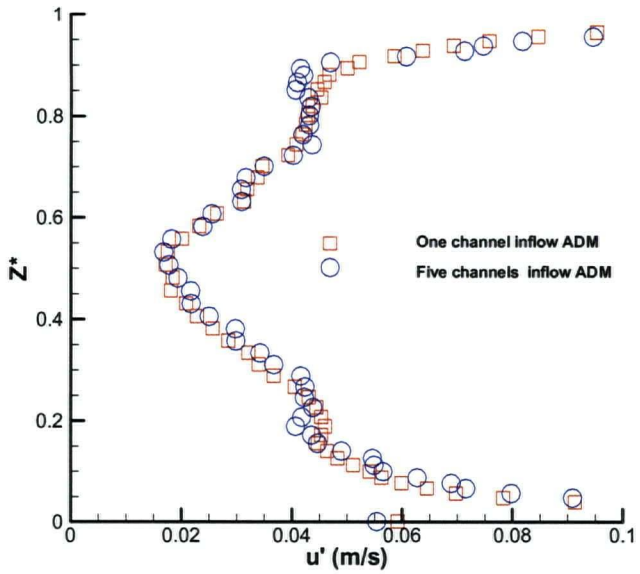

Figure 6.18 Comparison of rms value of the velocity fluctuation u' at the third station EF.

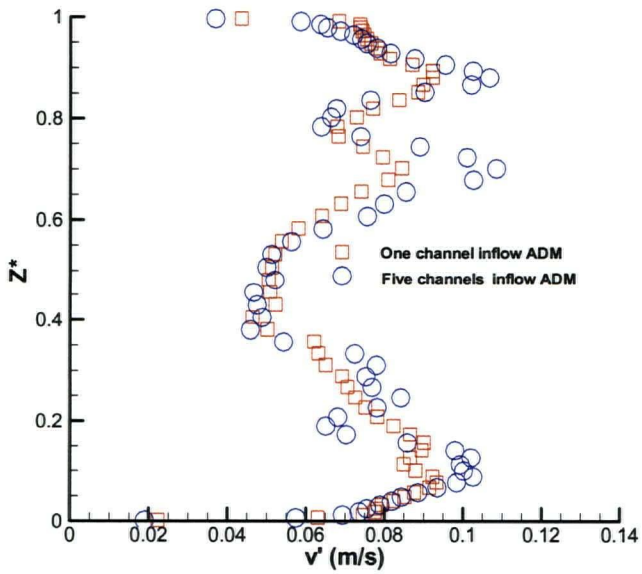

Figure 6.19 Comparison of rms value of the velocity fluctuation v' at the third station EF.

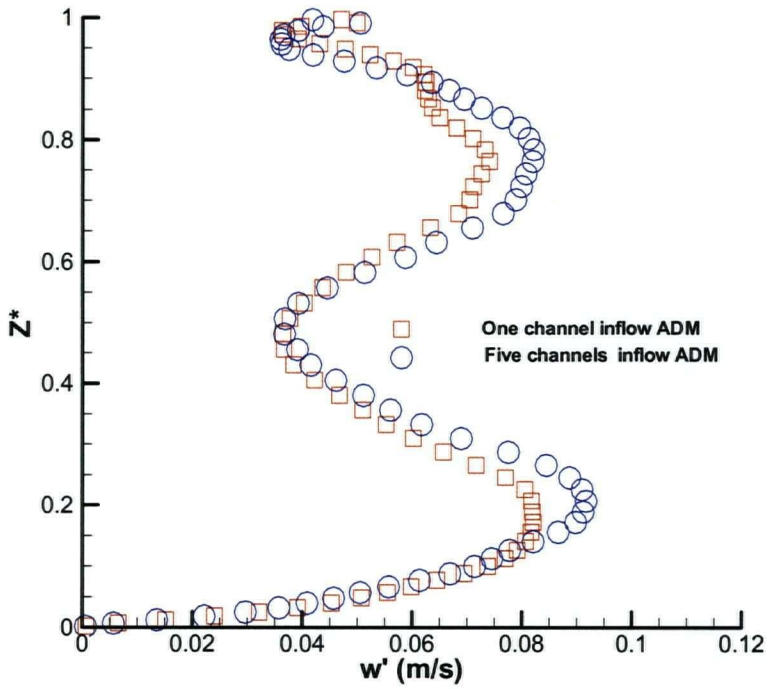

Figure 6.20 Comparison of rms value of the velocity fluctuation w' at the third station EF.

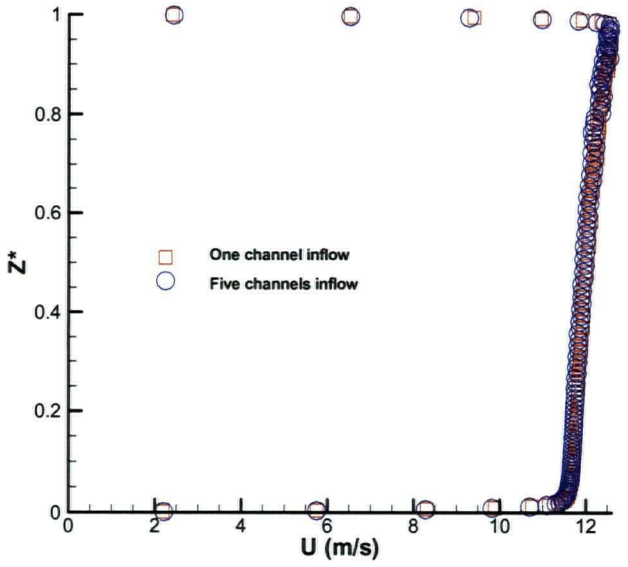

Figure 6.21 Comparison of the mean velocity at the outlet.

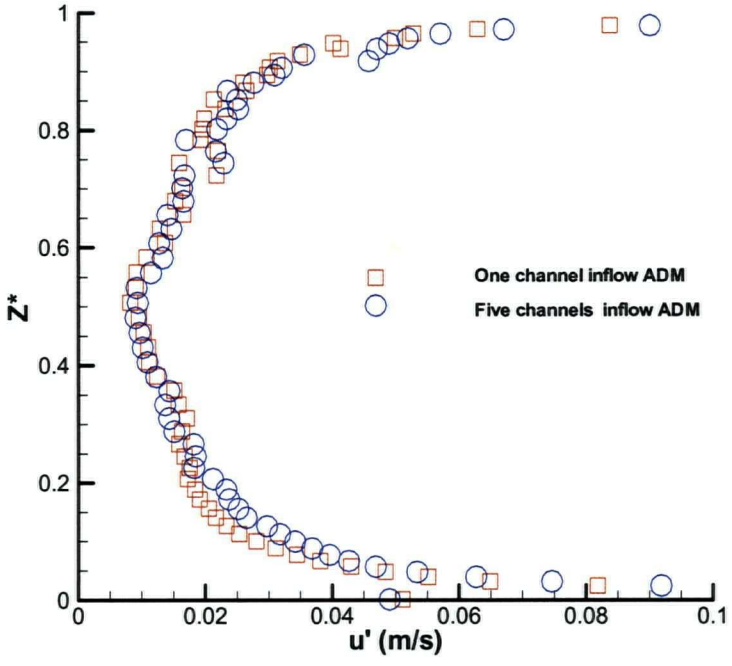

Figure 6.22 Comparison of rms value of the velocity fluctuation u' at the outlet.

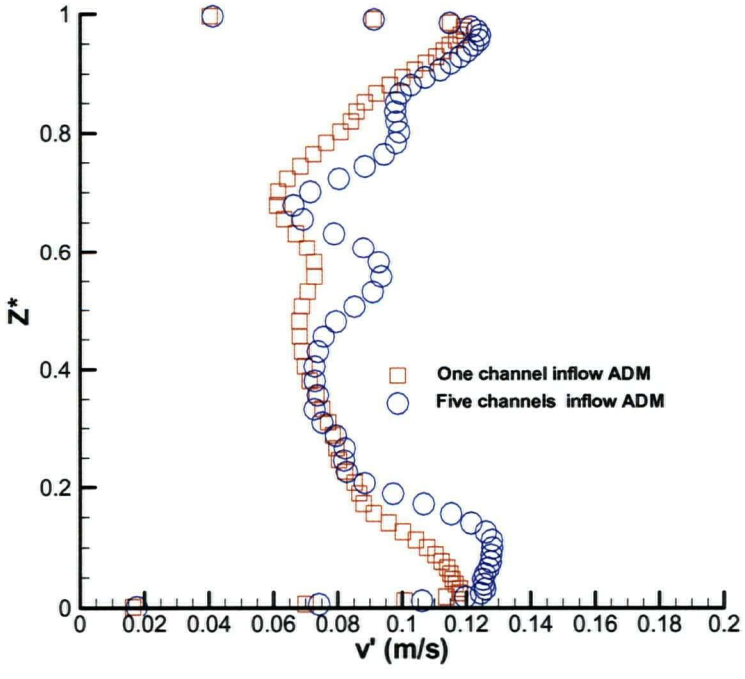

Figure 6.23 Comparison of rms value of the velocity fluctuation v' at the outlet.

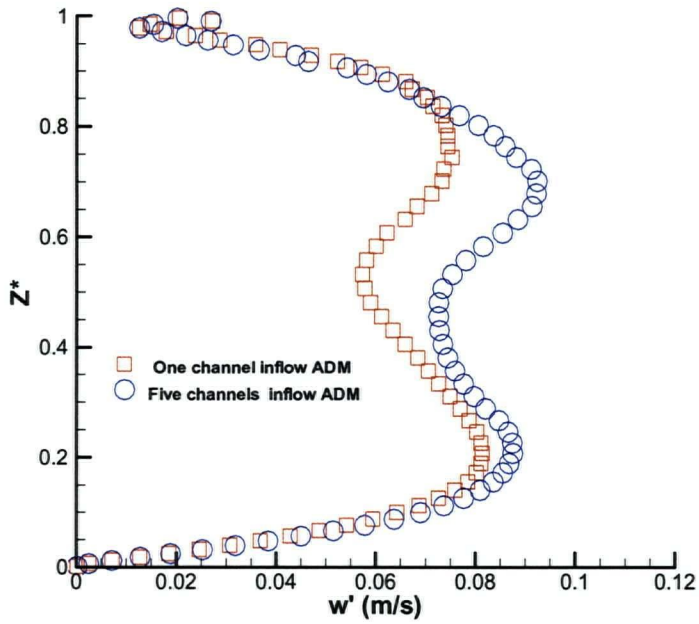

Figure 6.24 Comparison of rms value of the velocity fluctuation w' at the outlet.

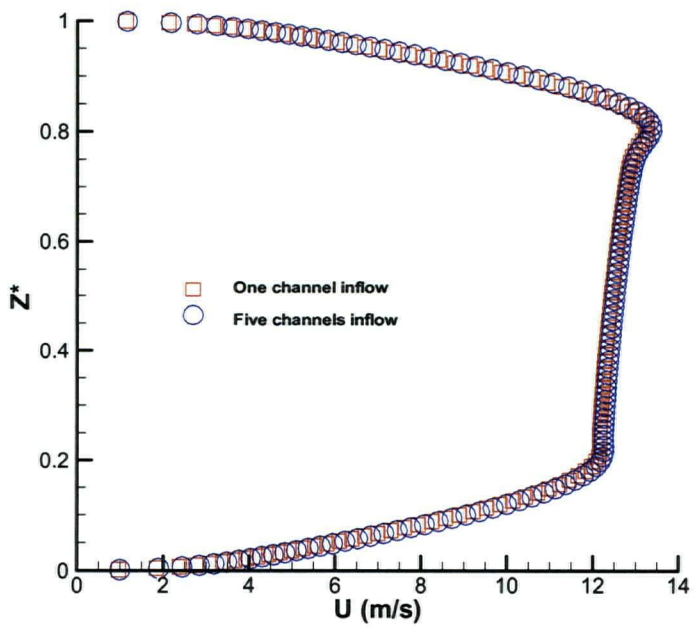

Figure 6.25 Comparison the mean velocity profiles at the outlet with the Smagorinsky model.

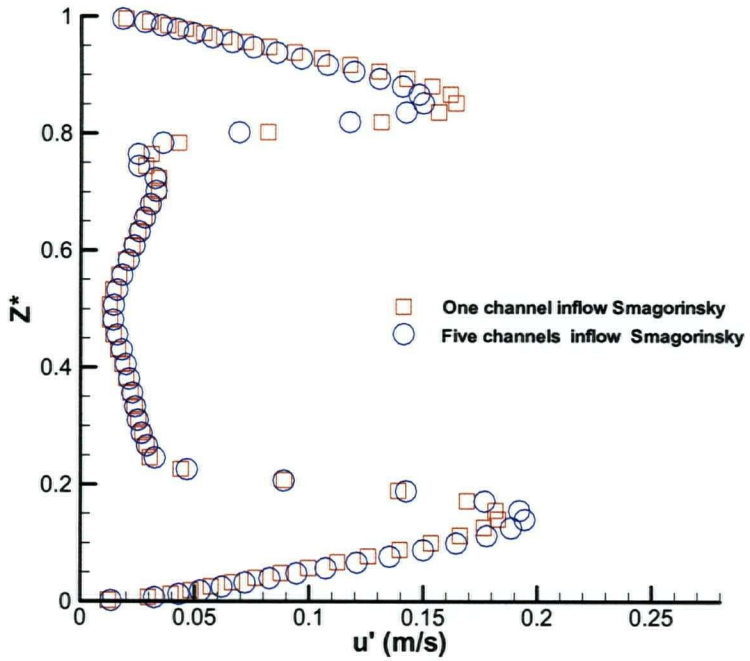

Figure 6.26 Comparison of rms value of the velocity fluctuation u' at the outlet with the Smagorinsky model.

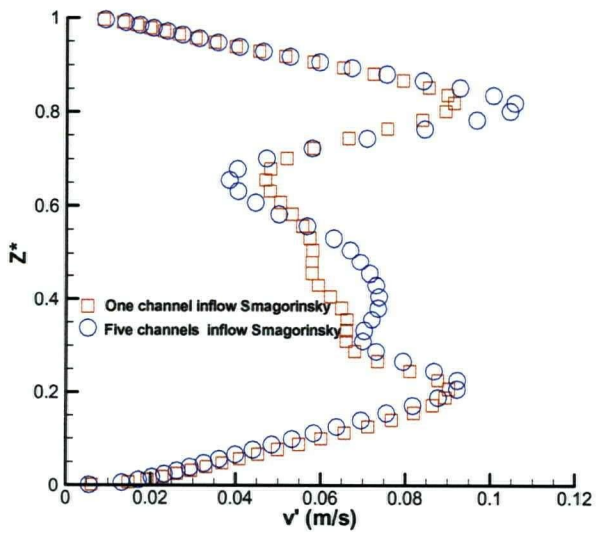

Figure 6.27 Comparison of rms value of the velocity fluctuation v' at the outlet with the Smagorinsky model.

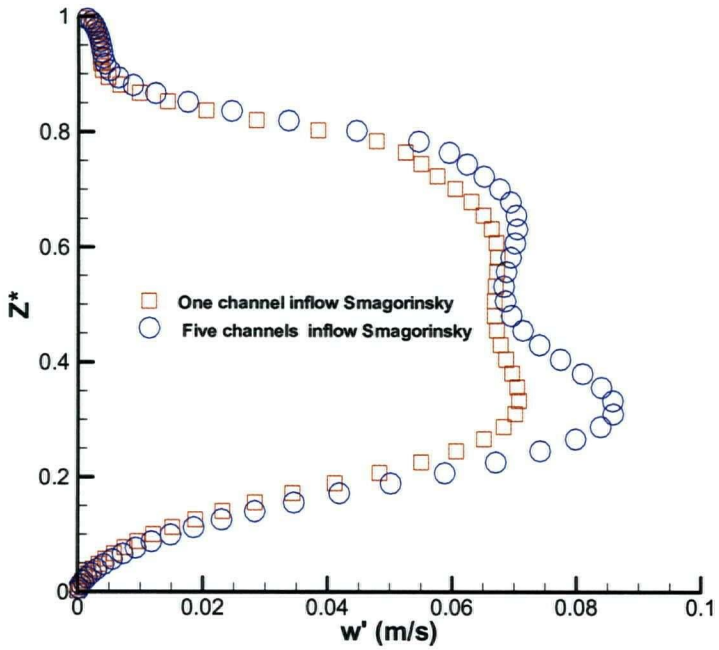

Figure 6.28 Comparison of rms value of the velocity fluctuation w' at the outlet with the Smagorinsky model.

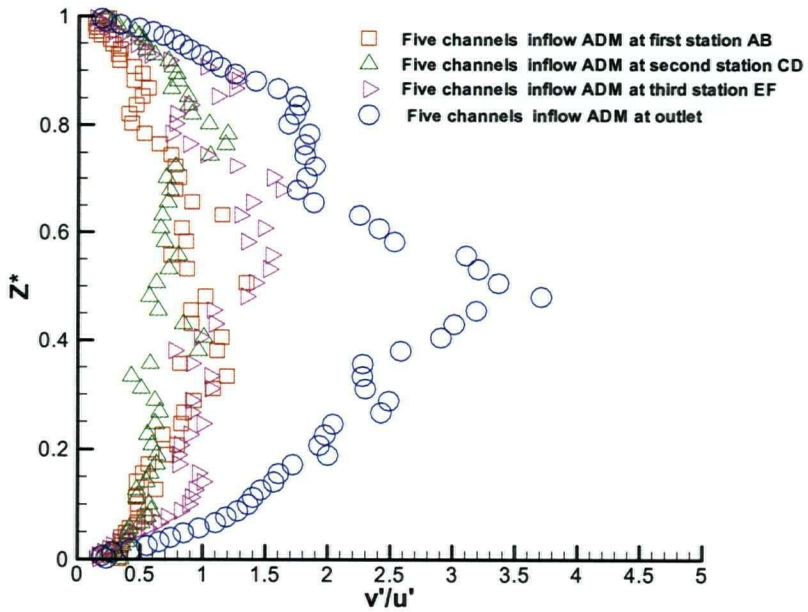

Figure 6.29 Comparison of the ratio v'/u' at different positions.

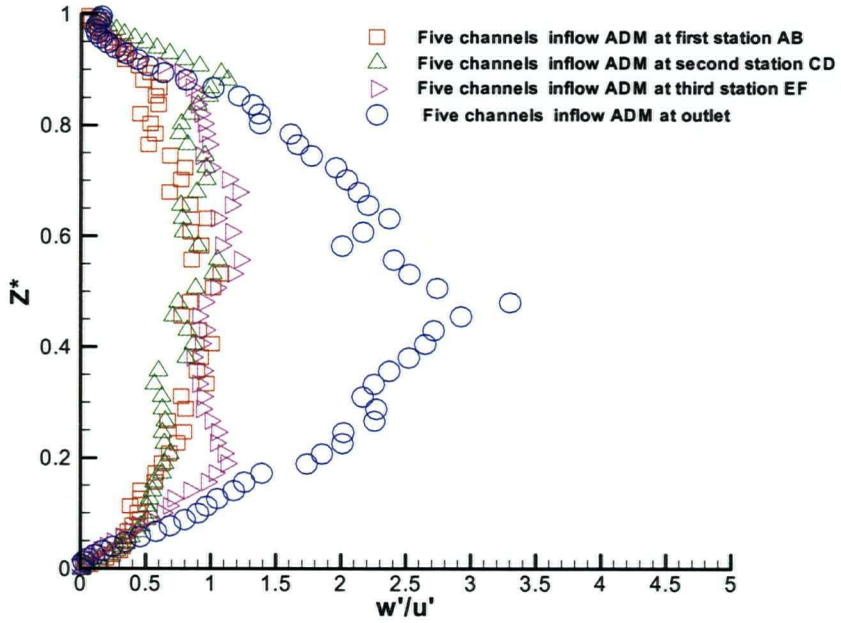

Figure 6.30 Comparison of the ratio w'/u' at different positions.

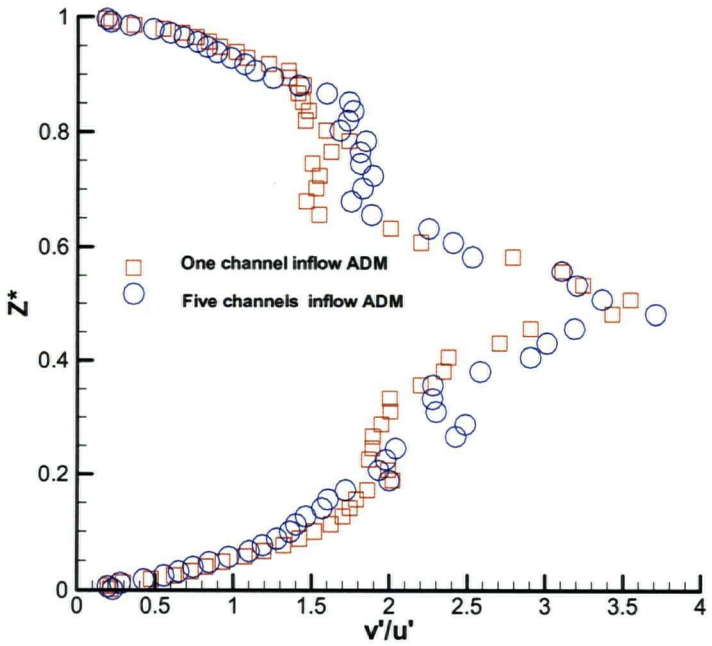

Figure 6.31 Comparison of the ratio v'/u' at the outlet with the two different inflow conditions.

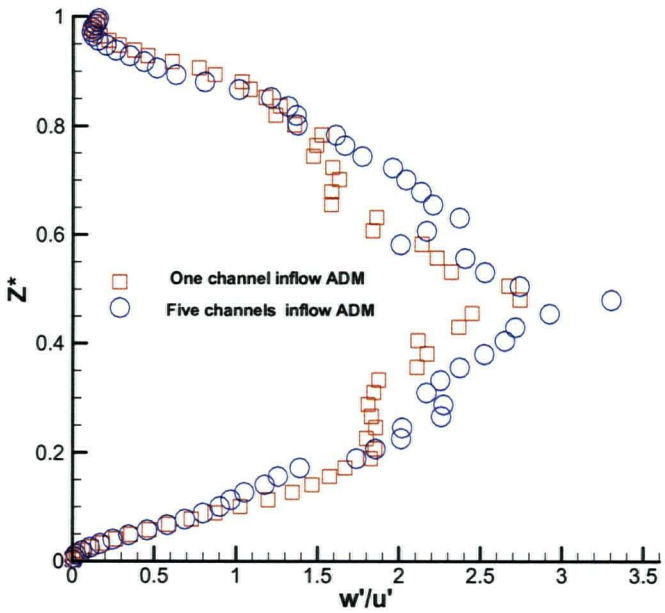

Figure 6.32 Comparison of the ratio w'/u' at the outlet with the two different inflow conditions.

6.3 Summary

Large eddy simulations are carried out for a commercial sized headbox. Two inflow conditions for the converging section, a one-channel inlet and a "five-channel" inlet, are investigated and two alternative subgrid models are compared.

The two inflow conditions are significantly different at the inlet of the converging section. At one-sixth of the whole length position, this difference is reduced. The turbulence generated from "five-channel" inflow conditions is greater than that from one-channel inflow conditions at one third of the whole length position. At the outlet of the headbox, more turbulence is indeed generated using the "five-channel" inflow. However, the difference at the outlet between the two inflow conditions is not large.

From the simulations, it is clear that the turbulence is close to isotropic at the first and second stations in most regions, but the anisotropy of the turbulence grows quickly near the outlet. At the outlet, the turbulence is very anisotropic in most regions.

One limitation of our calculations is that the periodic boundary condition is applied in the spanwise direction for all calculations. In the real commercial headbox, there are walls placed at regular intervals in the y direction in the five channel turbulence-producing tubes that form the entry for the "five-channel" condition in the present simulations. Since the length in the y direction is very large ($8.64\ m$) compared to the length in the streamwise direction ($0.665\ m$), the effects of wall conditions for mean flow and turbulence would be expected to be small at the outlet. Removal of the periodic boundary conditions in the spanwise direction, while certainly possible, would require a major change in the calculation procedure and so is being left for future work.

The turbulence generated in the tubes decays significantly in the converging section. Even the low level of turbulence intensity observed toward the exit of the converging section seems to be very important for the fiber distribution. This conclusion was reached in chapter 5, when computing fiber trajectories considering only the main flow as compared with computing them with turbulence fluctuations accounted for in a laboratory headbox calculation. The fibers move essentially with the same mean speed as the fluid so that the absolute turbulence intensity is of importance to them, not the apparently small relative turbulence intensity. The objective 5, described in chapter 1, is achieved.

Chapter 7 Summary and Conclusions

In this thesis, a numerical tool has been developed to simulate turbulence in a headbox. Using this tool, the flow through the headbox converging section has been investigated with parallel computing techniques and the large eddy simulation turbulence model. In addition, the statistical orientation of fibers passing through a headbox has been simulated by coupling the flow calculation with a suitable fiber model. The major findings of this thesis are summarized below:

7.1 Parallel computing

In chapter 3, two methods, the direct method and the CGSTAB method, are employed to solve the Poisson equation. The MPI library is used to implement the message passing between processors.

Parallel computation with the direct method is straightforward using ALL-TO-ALL (MPI command) to exchange the data. For the CGSTAB method, Incomplete LU (ILU) is used as a preconditioner. A staircase parallelization algorithm is therefore used for the parallel implementation with the CGSTAB method. The advantage of this algorithm is that the serial and parallel versions have the same behavior with respect to convergence. The CGSTAB method is slower than the direct method, but it can be applied in more general cases. For parallel computation of a large eddy Simulation, the domain decomposition approach is used to partition the data. Each sub-domain data is assigned to one processor to calculate the quantities and exchange the boundary data with neighbors. The parallel efficiency is still higher than 80% for the parallel computation of a large eddy simulation. The computational time can be reduced much more with more processors. This makes numerical simulation of complex problems possible using parallel computation.

7.2 LES for turbulent flow through a converging section

The Navier-Stokes equations were solved using a staggered finite volume method for a generalized curvilinear coordinate system. The fractional step method was used to solve the momentum equations. A Poisson equation for pressure was obtained to satisfy the continuity equation. For the channel flow, the fast Fourier transform and the cyclic reduction method were presented to solve the Poisson equation. CGSTAB method was used to solve the Poisson equation for the converging section flow.

The channel flow at Re_τ = 395 was modelled first with three different SGS models utilizing three alternative mesh sizes. The coarse mesh case did not predict the logarithmic layer well, which can be arributed to an inadequate grid resolution. The fine mesh case was close to the reference DNS result. The medium case was close to the fine mesh case. The Smagorinsky SGS model shows little difference from results obtained with the dynamic SGS model. The peak value of the dynamic coefficient was 10% higher than the Smagorinsky coefficient. In most of the computational region, the difference between the dynamic model coefficient and the Smagorinsky coefficient is less than 2%. The ADM model improves the mean velocity profile compared to the Smagorinsky model. The reason is that the ADM model uses an explicit filter and recovers a part of small scales from the large scales directly. The resolved turbulence intensities with the ADM model are close to the Smagorinsky model results.

At the higher Reynolds number Re_τ = 1655, the channel flow was computed by using two different mesh sizes. The trend in the calculations was similar to that of the low Reynolds number case.

The Smagorinsky model with $64\times64\times64$ mesh can provide a good representation of channel flow and is used to provide inflow conditions for the modelling of the converging section as described in chapter 4.

The proper inflow condition is challenging for the present quantitative predictions. The most straightforward approach to obtain the inflow conditions for the converging section is to start the calculation by completely modeling the upstream rectifier tubes. This procedure would be very time consuming. One channel inflow condition was employed to compute the turbulent flow in the converging section. This approach was also used by Kaltenbach *et al.* (1999), where a channel flow was used to generate inflow conditions for a plane diffuser. The computed values of the mean velocity agreed well with the measured values. For rms fluctuations, there were some differences between the numerical results and the measured results over the first third of the converging section length. The use of a "two-channel" inflow condition was also tested. Different inflow conditions can indeed affect the fluctuation results. The "two-channel" inflow condition was better than one channel inflow condition, but one evident problem in the results using the "two-channel" inflow condition was that the computational streamwise fluctations were only half of the measured values at 0.03m from inlet of converging section.

A new generation of inflow conditions method was proposed. The idea was based on the extracting/rescaling technique developed by Lund *et al.* (1998). The computed streamwise fluctations and mean velocity using this new inflow data agreed reasonably well with the measured values at 0.03m from inlet of converging section. For the results along the centerline of the converging section, they were almost the same as those with one channel inflow condition. The values of v' with the new inflow condition were better than those with the one channel inflow condition.

The grid dependence study also revealed a sensitivity to the inflow condition. A finer mesh in the wall-normal direction can provide better agreement between the predicted and measured rms values of the velocity fluctuations along the centerline of the converging section. This is because the values of the velocity fluctuations v' and w' at the inlet were closer to the measured values when a fine mesh was used in the wall-normal direction.

The agreement of rms values of velocity fluctuations between the computational results and the measured values was less satisfactory. The disagreement can be partially related to the coarse mesh in the wall-normal direction. The grid dependence study suggested that a finer mesh would probably improve the numerical results. Another possible reason for the apparent difference between measured and predicted results was that a periodic condition in the spanwise direction was used while in the experimental apparatus there was a wall. Finally, it must be noted that in the experiment, there was also the possibility that flow rates in the adjacent rectifier tubes were different. From Shariati (2002), it is known that the velocity profile is different for the top and the bottom rectifier tube in the experimental measurements. This will lead to inflow conditions that are unique to the apparatus and impossible to model with precision.

7.3 Fiber orientation

The LES and a fiber motion model have been coupled for predicting the orientation of rigid fibers in dilute suspensions. The effects of turbulence that would tend to randomize the fibers were included in the fiber motion simulations. Random initial fiber orientations were set at the inlet of the channel. The statistical distribution for the orientation of a large number of fibers was evaluated at each station by computing the orientation of each single fiber along the central streamline. The LES results predicted the fiber orientation reasonably well when compared to the experimental data. The predicted orientation distributions near the exit of the converging section were better with LES than with those using the $k-\varepsilon$ model for turbulence.

7.4 Simulation of a typical industrial headbox

High Reynolds number large eddy simulations were carried out for a commercial sized headbox. Two inflow conditions for the converging section were investigated.

The two inflow conditions were significantly different at the inlet of the converging section. At the sixth of the whole length position, this difference was reduced. The turbulence generated from "five-channel" inflow conditions was greater than that from one channel inflow conditions at one third of the whole length position. At the outlet of the headbox, more turbulence was indeed generated using the "five-channel" inflow. However, the difference at the outlet between the two inflow conditions was not large.

From the simulations, it was known that the turbulence was close to isotropic at the first and second stations in most regions, but the anisotropy of the turbulence grew quickly near the outlet. At the outlet, the turbulence was very anisotropic in most regions.

The turbulence generated in the tubes decayed significantly in the converging section. Even the low level of turbulence intensity observed toward the exit of the converging section seemed to be very important for the fiber distribution. This conclusion was reached in chapter 5, when computing fiber trajectories considering only the mean flow as compared with computing them with turbulence fluctuations accounted for in a laboratory headbox calculation.

From the above summary, the most important conclusions are listed below:

- The techniques for parallel computation of a large eddy simulation are necessary and successful. The parallel efficiency can be higher than 80%. This makes numerical simulation of this complex problem possible.
- For the channel flow, the dynamic model is very close to the Smagorinsky model. The Smagorinsky model with $64\times64\times64$ mesh can provide a good representation of the channel flow. The ADM model can improve the mean velocity profile using the explicit filter, but the ADM model needs much more computational time than the Smagorinsky model.

- Computations in an asymmetrical converging section show that the turbulence is very anisotropic, especially toward the exit of the converging section. Turbulence which survives the convergence will be strongly non-isotropic near the exit of any strongly converging section.
- The standard $k-\varepsilon$ model fails to predict the values of turbulence kinetic energy and therefore it should not be used in strongly converging sections.
- For inflow conditions mimicking both one and two upstream channels, the mean flow computations agree with the experimental values. The computed turbulence fluctuations reproduce the experimental trends but the quantitative agreement is less good especially in the first third of the converging section length.
- The LES coupled with a suitable fiber model to predict the orientation of nylon "fibers" in the converging section, gives statistical results similar to experimental data.
- For the industrial headbox, multiple channels give somewhat higher turbulence at the exit compared to a single inlet channel, but the inlet turbulence has a limited effect on the turbulence at the exit.

Chapter 8 Recommendations for Future Work

This thesis has developed a parallel numerical tool to simulate the large scales of turbulence in a headbox using the LES model for turbulence. The fiber orientation in a headbox has been studied using this tool when coupled with a suitable fiber model. Further development can be done to provide a more accurate simulation of the turbulence inside the headbox. Some recommendations are as follows:

The inflow condition for the headbox is still a challenging topic. In the present thesis a modified method that is similar to the random method is used to generate the inflow field. But the computational inflow condition still cannot represent the experimental inflow condition accurately. This may result in a difference between numerical and experimental results near the exit of a headbox. It would be better to simulate the complete rectifier tubes upstream of the converging section together with the converging section in the future. There may also be significant effects of non-uniform flow entering the rectifier tubes; there is some suggestion that the present experimental data is contaminated by such an effect. Sample calculations which introduce known non-uniform inflow conditions could quantify the downstream effects of upstream flow spatial non-uniformities.

In the converging section simulations, the boundary condition assumed in the cross-machine direction is periodic. This assumption is economical and reasonable for focusing on the middle region of the converging section. The wall boundary condition in the spanwise direction in the incoming turbulence tubes and possibly in the converging section itself must be used if we consider the actual headbox converging section. In this situation, the fast FFT cannot be used. The parallel CGSTAB method in chapter 3 could be used to solve the Poisson equation. This would require more CPU time however, which may be practical in the near future.

Bibliography

Aidun, C. and Kovacs, A.E., Hydrodynamics of the forming section: the origin of non-uniform fiber orientation, *TAPPI Journal*, 78(11), pp. 97-106, 1995.

Anczurowski, E. and Mason, S.G., The kinetics of flowing dispersions. II. Equilibrium orientations of rods and discs (experimental), *J. Colloid Interface Sci.* 23, pp.533-546, 1967.

Banhakavi, V. S. and Aidun, C. Analysis of turbulent flow in the converging zone of a headbox, *TAPPI* Engineering/Process and Product Quality Conference & Trade Fair, pp.1135-1154, 1999.

Bastian, P., and Horton, G., Parallelization of robust multigrid methods: ILU factorization and frequency decomposition method, *SIAM. J. Stat. Comput.* 12, pp.1457-1470, 1991.

Bonnet, J.P., Delville, J., Druault, P., Sagaut, P. and Grohens, R., Linear stochastic estimation of LES inflow conditions. (Advances in DNS/LES, Liu, C. and Liu, Z. eds.) Greyden Press, pp. 341-348, 1997.

Britt, K.W., Handbook of pulp and paper technology, Van Nostrand Reinhold, 1970.

Burden, R.L. and Faires, J.D., numerical analysis, (5th Ed.). PWS Publishing Company, 1993.

Carati, D., Winckelmans, G. and Jeanmart, H. On the modelling of the subgrid-scale and filtered-scale stress tensors in large-eddy simulation, *J. Fluid Mech.* 441, pp.119-138, 2001.

Chorin, A.J., Numerical solution of the Navier-Stokes equations, *Math. Comput.*, 23, pp. 341-354, 1968.

Chowdhury, D., Introduction to the Renormalization Group method and turbulence modelling, Fluent inc., TM-107 (cross-reference), 1993.

Clark, J.H., Ferziger, J. H. and Reynolds, W. C., Evaluation of subgrid-scale models using an accurately simulated turbulent flow, *J. Fluid. Mech.*, 91, pp. 1-6, 1978.

Crowe, C.T., Gore, R. A. and Troutt, T. R., Particle dispersion by coherent structures in free shear flows, *Part. Sci. Tech.* 3, pp.149-158, 1985.

Dahl, H. K. and Weiss, H. G., A new hydraulic principle for headboxes, *TAPPI Journal*, 58(11), pp. 72-77, 1975.

Deardodff, J.W. Three dimensional numerical study of turbulence in an entrained mixing layer. In AMS Workshop in Meteorology, American Meteorological Society, 1973.

Deardorff, J.W., A numerical study of three-dimensional turbulent channel flow at large Reynolds numbers. *J. Fluid Mech.* 41, 1970.

Dong, S., Modelling of Fiber motion in pulp and paper equipment, Ph.D. thesis, University of British Columbia, 2002.

Dong, S., Feng, X., Salcudean M. and Gartshore, I., Concentration of pulp fibers in 3D turbulent channel flow, *Inter. J. Multiphase Flow,* vol. 29, 1, pp. 1-21, 2003.

Dong, S., Feng, X., Salcudean, M., Gartshore, I. and Shariati, M., Turbulence and Fiber Orientation in the Converging Section of a Paper-machine Headbox, The 4th ASME/JSME/KSME Symposium on Computational Techniques for Fluid/Thermal/Chemical Systems with Industrial Applications, Vancouver, Canada, 2002.

Ferziger, J. and Peric, M. Computational methods for fluid dynamics, Springer Verlag, Second Edition,1999.

Fessler, J. R., Kulick, J. D. and Eaton, J. K., Preferential concentration of heavy particles in a turbulent channel flow, *Phys. Fluids* 6, 11, pp.3742-3749, 1994.

Gavelin, G., Paper machine design and operation- descriptions and explanations-, Angus Wilde Publications Inc., 1998.

Germano, M., Poimelli, U., Cabot, W.H., and Moin, P. A dynamic subgrid scale eddy viscosity model. *Phys. Fluids* A, 3(7), pp.1760-1765, 1991.

Ghosal, S., An analysis of numerical errors in large-eddy simulation of turbulence, *J. comput. Phys.*, 125, pp. 187-206, 1996.

Ghosal, S., Lund, T., Moin, P. and Akselvoll, K., A dynamic localization model for large eddy simulation of turbulent flows. *J. Fluid Mech.*, 286, pp. 229-255, 1995.

Gooding, R. W., The passage of fibres through slots in pulp screening, M. A. Sc thesis, University of British Columbia, 1986.

Gooding, R. W., Flow Resistance of Screen Plate Apertures, Ph. D thesis, University of British Columbia, 1996.

Gooding, R. W., Kerekes, R. J. and Salcudean, M., The Flow Resistance of Slotted Apertured in Pulp Screens, *The Science of Papermaking,* 1, pp. 287-338, 2001.

Golub, G., H. and van Loan, C. F., Matrix Computations (The Johns Hopkins University Press, New York), 1993.

Gullbrand, J. and Chow, F. K., The effect of numerical errors and turbulence models in large-eddy simulations of channel flow, with and without explicit filtering, *J. Fluid Mech.*, 495, pp. 323-341, 2003.

Gustafsson, I., A class of first order Factorization methods, *BIT*, 18, pp. 142-156, 1978.

Hämäläinen, J., Mathematical modelling and simulation of fluid flows in the headbox of paper machines. Ph.D. Thesis, University of Jyväskylä, 1993.

He, P. and Salcudean, M., A numerical method for 3D viscous incompressible flows using non-orthogonal grids, *Int. J. Numer. Methods in Fluids*, 18, pp. 449-469, 1994.

He, P., Bibeau, E. L., Hua, L., Salcudean, M. and Gartshore, I., Fluid dynamics of the flow distribution in a headbox, *CPPI* conference, Montreal, 1998.

Horiuti, K. Comparison of conservative and rotational forms in large eddy simulation of turbulent channel flow. *J. Comp. Phys.* 71, 1987.

Hackbusch, W., Multi-grid methods and applications, Springer, Berlin, 1985.

Hua, L, Bibeau, E. L., He, P., Salcudean. M. and Gartshore, I., Flow distribution in a hydraulic headbox." *TAPPI* conference, Anaheim, 1999.

Hua, L., He, P., Salcudean, M., Gartshore, I. and Bibeau, E. L., Turbulent flow in hydraulic headbox, *TAPPI* conference, Vancouver, 2000.

Jeffery, G. B., The motion of ellipsoidal particles immered in a viscous fluid. *Proc. Royal Soc.*, A102, pp.161-179, 1922.

Joubert, W., Oppe, T., Janardhan, R. and Dearholt, W., Fully Parallel Global M/ILU Preconditioning for 3-D Structured Problems. 2000.

Kaltenbach,H., Towards a near-wall model for LES of a separated diffuser flow. *Annual Research Briefs*, Center for Turbulence Research, NASA Ames/Stanford Univ., pp.255-265, 1998.

Kaltenbach,H., Fatica, M., Mittal, R., Lund, T.S. and Moin, P., Study of flow in a planar asymmetric diffuser using large-eddy simulations, *J. Fluid Mech.*, 390, pp. 151-185, 1999.

Kim,J. and Moin,P., Application of fractional-step method to incompressible Navier-stokes equations. *J. Comp. Phys.*, 59, pp.308-323, 1985.

Kim,J., Moin,P. and Moser, R. D., Turbulence statistics in fully developed channel flow at low Renolds number, *J. Fluid Mech.*, 177, pp. 133-166, 1987.

Kumar, A., Passage of fibers through screen apertures. Ph.D. thesis, University of British Columbia, 1991.

Lawryshyn, Y. A., Statics and dynamics of pulp fibers, Ph.D. thesis, University of Toronto, 1997.

Lee, S., Lele, S. K. and Moin, P., Simulation of spatially evolving turbulence and the applicability of Taylor's hypothesis in compressible flow, *Phys. Fluids* A 4, pp. 1521-1530, 1992.

Lesieur,M. and Metais, O. New trends in large-eddy simulations of turbulence, *Annu. Rev. Fluid. Mech.* 28, pp.45-82,1996.

Lilly,D.K. On the application of the eddy viscosity concept in the inertial sub-range of turbulence, NCAR Manuscript No. 123,1966.

Lilly,D.K., A proposed modification of the Germano subgrid scale closure method, *Phys. Fluids* A *4*, pp.663-665, 1992.

Lund, T. S., On the use of discrete filters for large eddy simulation. *Annual Research Briefs*, Center for Turbulence Research, NASA Ames/Stanford Univ., pp.83-95, 1997.

Lund, T. S., Wu, X., and Squires, K. D., generation of turbulent inflow data for spatially-developing boundary layer simulations, *J. Comp. Phys.*, 140, pp.233-258, 1998.

Loewen, S. R., Fiber orientation optimization, *Pulp Paper Can.*, 98(10), pp67-71, 1997.

Mason, S.G., Fiber motions and flocculation, *TAPPI Journal*, **37**(11), pp.494-501, 1954.

Moin, P. and Kim, J. Numerical investigation of turbulent channel flow, *J. Fluid Mech.* 118, pp.341-377, 1982.

Moser, R. D., Kim, J. and Mansour, N. N., Direct numerical simulation of turbulent channel flow up to $\mathrm{Re}_\tau = 590$, *Phys. Fluids*, 11, pp.943-945, 1999.

Najjar, F.M. and Tafti, D. K., Study of discrete test filters and finite difference approximations for the dynamic subgrid-scale stress model , *Phys. Fluids*, 8, pp.1076-1088, 1996.

Olson, J. A., The effect of fiber length on passage through narrow apertures, Ph.D. thesis, University of British Columbia, 1996.

Olson, J. A., Analytic estimate of the fiber orientation distribution in a headbox flow, *Nordic Pulp Paper Res. J.* ,17 (3), pp. 302-306, 2002.

Olson, J. A., Frigaard, I., Chan, C. and Hämäläinen, J., Modelling a turbulent fiber suspension flowing in a plannar contraction: The one-dimensional headbox, *Inter. J. Multiphase Flow,* vol. 30, 1, pp. 51-66, 2004.

Parsheh, M. and Dahlkild, A.A. Modelling the flow around elastic guiding vanes and turbulence in a two-dimensional contraction, *TAPPI* Engineering/Process and Product Quality Conference & Trade Fair, pp.1433-1452, 1999.

Peel, J. D., Paper science and paper manufacture, Angus Wilde Publications, 1999.

Piomelli, U., Moin, P. and Ferziger, J.H., Model consistency in large eddy simulation of turbulent channel flows. *Phys. Fluids*. 31, 1988.

Pougatch, K., Salcudean, M., Gartshore, I. and Abdullah, Z., A computational analysis of a headbox flow: a case study, Practical Papermaking conference, Milwaukee, WI, 2005.

Rai, M.M. and Moin, P., Direct numerical simulation of transition and turbulence in a spatially evolving boundary layer, *J. Comp. Phys*. 109, pp. 169-192, 1993.

Reynolds, W. C., The potential and limitations of Direct and Large Eddy Simulations. *Whither Turbulence? Turbulence at the Crossroads*, J. L. Lumley, Ed., vol.357, Lecture Notes in Physics, Ithaca, New York, pp. 313-343, 1989.

Rogallo,R.S. and Moin, P. Numerical simulation of turbulent flows. *Ann. Rev. Fluid Mech*. 16, pp.99-137, 1984.

Rosenfeld, M., Kwak, D. and Vinokur, M., A fractional step solution method for the unsteady incompressible Navier-Stokes equations in generalized coordinate systems, *J. Comp. Phys*. 94, pp. 102-137, 1991.

Ross, R. F. and Klingenberg, D. J., Dynamic simulation of flexible fibers composed of linked rigid bodies, *J. Chem. Phys*. 106 (7), pp.2949-2960, 1997.

Rouson, D. W. I. and Eaton, J. K., Direct numerical simulation of turbulent channel flow with immersed particles, The 1994 ASME Fluids Engineering Division Summer Meeting, Lake, 1994.

Sagaut, P., Large eddy simulation for incompressible flows, Springer, 2001.

Schumann, U., Subgrid scale models for finite difference simulations of turbulent flows in plane channels and annuli, *J. Comp. Phys*. 18, pp.376-404, 1975.

Shariati, M. R., Bibeau, E., Salcudean M. and Gartshore, I., Numerical and Experimental Models of Flow in the Converging Section of a Headbox, *TAPPI* Papermakers Conference, Vancouver, Canada, 2000.

Shariati, M. R., Bibeau, E., Salcudean, M., Gartshore, I., Zhang, X. and Abdullah, Z. Computational Investigation of the Flow through a Headbox, *TAPPI* Engineering and Finishing Conference, San Antonio, 2001.

Shariati, M. R., Experimental and mathematical modelling of flow in headboxes, Ph.D. thesis, the University of British Columbia, (2002).

Shimizu, T. and Wada,K. Computer simulation of measurement of flow in a headbox. *Proceedings of the Pan Pacific Pulp and Paper technology conference*, pp.157-165, 1992.

Smagorinsky , J. General circulation experiments with the primitive equations. *Mon. Weather Rev.* 91(3), pp.99-164, 1963.

Smook, G. A., Handbook for pulp and paper technologists, Angus Wilde Publications, 1992.

Spalart, P. R., Theoretical and numerical study of a three-dimensional turbulent boundary layer, *J. Fluid Mech.*, 205, pp.319-340, 1989.

Speziale, C. G., On nonlinear k-l and k-ε models of turbulence, *J. Fluid Mech.*, 178, pp.459-475, 1987.

Stockie, J. M. and Green, S. I., Simulating the motion of flexible pulp fibers using the immersed boundary method, *J. Comp. Phys.* 147, pp.147-165, 1998.

Stolz, S., and Adams, N.A., An approximate deconvolution procedure for large-eddy simulation, *Phys. Fluids* 11, pp.1699-1701, 1999.

Stolz, S., Adams, N.A., and Kleiser, L., An approximate deconvolution model for large-eddy simulation with application to incompressible wall-bounded flows, *Phys. Fluids* 13, pp.997-1015, 2001.

Ullmar, M. and Norman, B., Observation of fiber orientation in a headbox nozzle at low consistency, *TAPPI* Proceedings, Engineering and Papermakers Conference, Anaheim, pp.865-869, 1997.

Ullmar, M., On fiber orientation mechanisms in a headbox nozzle, Master's thesis, Royal Institute of Technology, Stockholm, Sweden, 1998.

Van der Vorst, H. A., A fast and smoothly converging variant of BI-CG for the solution of nonsymmetric linear systems, *SIAM J. Sci. Statist. Comput.* 13, pp.631-644, 1992.

Vuik, C., van Nooyen, R.R.P., and Wesseling, P., Parallelelism in ILU-preconditioned GMRES, *Parallel Computing*, 24, pp.1927-1946, 1998

Wei, T. and Willmarth, W. W., Reynolds-number effects on the structure of a turbulent channel flow. *J. Fluid Mech.*, 204, pp.57-95, 1989.

White, F. M., Fluid Mechanics, forth edition, McGraw-Hill, Inc., 1998.

Wilcox, D. C., Turbulence modelling for CFD, Second Edition, DCW Industries, La Canada, CA, 1998.

Yakhot, A., Orszag, S. A., Yakhot, V. and Israeli, M., Renormalization group formulation of large-eddy simulations, *J. Sci. Comput.* 4, p.139, 1989.

Zang, Y, Street, R. L. and Koseff, J. R., A dynamic mixed subgrid-scale model and its application to turbulent recirculating flows, *Phys. Fluids* A 5, pp. 3186-3196, 1993.

Zhang, X., Fiber orientation in Headbox, M. A. Sc thesis, University of British Columbia, 2001.

Zhou, Y, Brasseur, J. and Juneja, A., A resolvable subfilter-scale model specific to large-eddy simulation of under-resolvable turbulence, *Phys. Fluids* 13, pp.2602-2610, 2001.

Appendix A

CG and CGSTAB algorithms

The CG algorithm is presented as follows:

- Initialize by setting: $k=0$, $u_0 = u_{in}$, $r_0 = Q - Au_{in}$, $p_0 = 0$, $s_0 = 10^{30}$, ε
- **while** $\| r_k \| > \varepsilon$ **do**

$$k = k+1$$

$$Mz_k = r_{k-1}$$

$$s_k = r_{k-1} \cdot z_k$$

$$\beta_k = s_k / s_{k-1}$$

$$p_k = z_k + \beta_k p_{k-1}$$

$$\alpha_k = s_k / (p_k \cdot Ap_k)$$

$$u_k = u_{k-1} + \alpha_k p_k$$

$$r_k = r_{k-1} - \alpha_k Ap_k$$

end while

The CGSTAB algorithm is given follows:

Initialize by setting: $k=0$, $u_0 = u_{in}$, $r_0 = Q - Au_{in}$, $p_0 = 0$, $\phi_0 = 0$, ε

$$\alpha_0 = \beta_0 = \gamma_0 = 1$$

- **while** $\| r_k \| > \varepsilon$ **do**

$$k = k+1$$

$$\beta_k = r_0 \cdot r_{k-1}$$

$\omega_k = (\beta_k \gamma_{k-1})/(\alpha_{k-1}\beta_{k-1})$

$p_k = u_{k-1} + \omega_k (p_{k-1} - \alpha_{k-1}\phi_{k-1})$

solve the system: $Mz = p_k$

$\phi_k = Az$

$\gamma_k = \beta_k /(\phi_k \cdot r_0)$

$w = r_{k-1} - \gamma_k \phi_k$

if $\| w \|_2 < \varepsilon$

$r_k = r_{k-1} - \gamma_k z$

return

end if

solve the system: $My = w$

$v = Ay$

$\alpha_k = (v \cdot r_k)/(v \cdot v)$

$u_k = u_{k-1} + \gamma_k z + \alpha_k y$

$r_k = w - \alpha_k v$

end while

Appendix B

Incomplete LU Decomposition

The preconditioner $M = LU$ should be a good approximation to A. In Incomplete LU (ILU), the L and U matrices have non-zero elements only on diagonals on which A has non-zero elements. Every element on the main diagonal of U is set to unity to make the matrices unique. The L and U have the following schematic presentation:

$$L = \begin{bmatrix} & & & & \\ & & & & \\ & & & & \\ & L_W & L_S & L_P & \\ & & & & \end{bmatrix}$$

$$U = \begin{bmatrix} & & & & \\ & & & & \\ & & & & \\ & & \mathrm{I} & U_N & U_E \\ & & & & \end{bmatrix}$$

where $L_W^l = A_W^l$, $\quad L_S^l = A_S^l$

$$L_P^l = A_P^l - L_W^l U_E^{l-N_j} - L_S^l U_N^{l-1}$$

$$U_N^l = A_N^l / L_P^l, \quad U_E^l = A_E^l / L_P^l.$$

The meaning of one-dimensional storage location index l and N_j can be found in Table 3.1 of Ferziger and Peric (1999).

Appendix C

Random Fluctuation Inflow Generation Method

A desired mean flow and Reynolds stress tensor are matched for the random fluctuation method. Let the target mean flow profile be $U_i(y)$ and Reynolds stress tensor by $R_{ij}(y) = < u_i' u_j' >_{z,t}$, where the operation $< >_{z,t}$ is an average on the spanwise direction and time. Three random numbers $\tilde{u}_i(z)$, $i = 1,2,3$ are generated. They satisfy the following condition: each sequence has zero mean and unit variance.

The velocity field is constructed according to

$$u_i(y,z) = U_i(y) + \beta_{ij}\, \tilde{u}_j(z)$$

where

$$\beta_{11} = \sqrt{R_{11}}, \qquad \beta_{21} = \frac{R_{21}}{\beta_{11}}$$

$$\beta_{22} = \sqrt{R_{22} - \beta_{21}^2}, \qquad \beta_{31} = \frac{R_{31}}{\beta_{11}}$$

$$\beta_{32} = \frac{R_{32} - \beta_{21}\beta_{31}}{\beta_{22}}, \qquad \beta_{33} = \sqrt{R_{33} - \beta_{31}^2 - \beta_{32}^2}.$$

β_{ij} not listed above are set zero.